THE MANUFACTURING AND INTEGRATION OF FLUIDIC OSCILLATORS FOR COMPOSITE AIRCRAFT STRUCTURES

A Dissertation
Presented to
The Academic Faculty

By

Ahmed A. Aly

In Partial Fulfillment
of the Requirements for the Degree
Master of Science in the
School of Mechanical Engineering

Georgia Institute of Technology

May 2017

THE MANUFACTURING AND INTEGRATION OF FLUIDIC OSCILLATORS FOR COMPOSITE AIRCRAFT STRUCTURES

Approved by:

Dr. Jonathan Colton, Advisor
School of Mechanical Engineering
Georgia Institute of Technology

Dr. Ari Glezer
School of Mechanical Engineering
Georgia Institute of Technology

Dr. Kyriaki Kalaitzidou
School of Mechanical Engineering
Georgia Institute of Technology

Date Approved: April 19, 2017

"If you know what you're worth,

then go out and get what you're worth."

-Rocky Balboa.

ACKNOWLEDGMENTS

First and foremost, I would like to thank my advisor, Dr. Jonathan Colton, for constantly providing guidance and steering me in the right direction throughout this project. I am appreciative of his availability to answer questions, even when I would spontaneously butt my head into his office during the day. I would also like to thank Pete George, Dr. Abe Gissen, and Randy Wilkerson from Boeing for their supportive input on the project. I am grateful for the GT-Boeing Strategic University Partnership for providing the opportunity and funding to work on an interesting thesis project. I would also like to thank my thesis committee members, Dr. Ari Glezer and Dr. Kyriaki Kalaitzidou.

From my lab, I would like to thank Jason Li for helping me get started with the project and providing guidance. I would also like to thank Viyat Jhaveri and Su Yu for their thoughtful insights. Additionally, I would like to thank the undergraduate assistants who worked on this project including Daniel Hochman, Daniel Budd, Kelly Storrs, and Connor Chadwick.

A special thanks to my friends from all over (Georgia Tech, Hawmies, Shabab ASK) for providing encouragement, a social outlet during the times of stress, and for keeping me grounded. Finally, I would like to thank my parents and my sister for their unfailing support and motivation. Without them, this accomplishment would not have been possible; thank you.

TABLE OF CONTENTS

Acknowledgments v

List of Tables x

List of Figures xii

Chapter 1: Introduction 1

Chapter 2: Background 6

2.1 Composites Review 6

2.1.1 Composite Properties 6

2.1.2 Composite Post Processing 8

2.1.3 Composite Joining Techniques 10

2.2 Current AFC Technologies 13

2.2.1 Aerospace Application 14

2.2.2 Non-Aerospace Applications 18

2.2.3 FO Manufacturing 18

2.2.4 FO Summary 20

2.3 Axiomatic Design 21

2.4 Chapter Summary 25

Chapter 3: Design Generation 26

3.1 Axiomatic Design 26

3.1.1 Customer Attributes 26

3.1.2 Decomposition 27

3.1.3 Design Matrix 30

3.2 Concept Generation 32

3.3 Initial Designs 35

3.3.1 Internal Designs 36

3.3.2 External Designs 40

3.3.3 Internal-External Designs 41

3.3.4 Comparison of Designs 42

3.4 Design Selection 43

3.4.1 Sensitivity Analysis 44

3.4.2 Design of Experiments 45

3.5 Chapter Summary 51

Chapter 4: Detail Designs 53

4.1 Internal 53

4.2 Internal-External 60

4.3 External 67

4.4 Final Design 70

4.4.1 CAD Model 70

4.4.2 Physical Model 75

4.5 Chapter Summary 77

Chapter 5: Validation 78

5.1 Finite Element Analysis 78

5.1.1 FO to Flap Attachment 78

5.1.2 Actuator to Sleeve Attachment 81

5.1.3 Snapfit Connection 85

5.2 Injection Molding Simulation 88

5.2.1 Actuator IM 88

5.2.2 Actuator Cover 90

5.2.3 Sleeve 92

5.3 Chapter Summary 93

Chapter 6: Cost Analysis 94

6.1 Manufacturing Cost 94

6.1.1 IM Cost 94

6.1.2 3D Printing Cost 98

6.2 Material and Assembly Cost 101

6.2.1 Material Cost 101

6.2.2 Assembly Cost 101

6.3 Design Configuration 103

6.4 Chapter Summary 107

Chapter 7: Conclusion 108

7.1 Summary 108

7.2 Future Work 111

Chapter A: Supporting Information 114

References 121

LIST OF TABLES

3.1 List of Customer Attributes and their corresponding Functional Requirements 27

3.2 Decomposition of Fluidic Oscillator Functional Requirements and Design Parameters 28

3.3 AD independence design matrix 31

3.4 FO Constraints 32

3.5 List of DPs and possible solution options 33

3.6 Morphological chart solution selection for one sample design 35

3.7 Internal design estimated costs and weights 43

3.8 External designs (green) and Internal-External designs (pink) estimated costs and weights 43

3.9 Full-factorial treatment levels 46

3.10 Design of Experiments Effects Summary 47

3.11 DOE Parameter Estimates and Variation Inflation Factors (VIF) 50

6.1 Percentage Increases for Appearance Levels [39] 96

6.2 Percentage Increases for Tolerance [39] 97

6.3 Parting Surface Classification [39] 97

6.4 IM mold costs for each component 98

6.5 SLS costs for different configurations 100

6.6 Material cost for each component 101

6.7 Part Handling Times [39] 102

6.8 Part Insertion Times [39] 103

6.9 Assembly Time Cost for each component 103

6.10 Manufacturing Design Configurations 104

A.1 Design attachment listings for preliminary designs. Designs are listed: Internal (1-9), External (10-13), Internal-External (14-15) 115

A.2 Snapfit assumptions 115

A.3 Fastener assumptions 115

A.4 Thermal Staking assumptions 115

A.5 Co-cure assumptions 116

A.6 Adhesive assumptions 116

A.7 Ultrasonic welding assumptions 116

LIST OF FIGURES

1.1 Attached flow versus separated flow on an airfoil at different angles of attack [1] 1

1.2 Different variations of aircraft flaps [2] 3

1.3 Wing flap showing an ideal AFC insertion location 4

2.1 A standard waterjet cutting machine with the labeled components shown [16] 9

2.2 Diagram showing the high usage of adhesive bonding on a Boeing airplane [21] 12

2.3 Two types of AFC actuators 13

2.4 Wing model utilizing pulsed blowing FO devices [4] 15

2.5 Boeing vertical tail with FOs installed [3] 16

2.6 FO attached to non-structural bullnose wing region [28] 17

2.7 AFC attached to z-spar near leading edge [5] 17

2.8 AFC devices attached to the rear end of the truck [29] 18

2.9 FO costs for different manufacturing processes [24] 20

2.10 Four domains of the design cycle [32] 22

2.11 Three types of matrices in AD [32] 22

2.12 An example of the zig-zagging process [32] 23

2.13 Probability Distribution vs Design Parameter [32] 24

3.1 Internal design basic layout 36
3.2 Internal design with the actuator attached to the spar 37
3.3 Internal design with the support connected to the spar 38
3.4 Internal actuator array prior to insertion 38
3.5 Internal actuators connected to a plenum prior to insertion into a guide rail . 39
3.6 Internal actuators fixed into guide rail 39
3.7 External design insertion 40
3.8 Internal-External design insertion 41
3.9 Sensitivity analysis on different parameters affecting total estimated cost . . 44
3.10 Design of Experiments Prediction Plot 48
3.11 DOE Material Cost Leverage Plot 49
3.12 DOE Assembly Time Leverage Plot 49
3.13 Design of Experiments Interaction Plots 51

4.1 Internal design detached 54
4.2 Internal Design, with the doubler attached 54
4.3 Internal Design: Actuator and cover shown as two parts 55
4.4 Internal Design: Actuator 56
4.5 Internal Design: Actuator top surface with sealant groove shown 57
4.6 Design parameters considered in snapfit design 58
4.7 Internal Design: Sleeve isometric view 59
4.8 Internal Design: Sleeve back view 59
4.9 Internal Design flap cutout region 60

4.10 Preliminary design showing external attachment 61

4.11 Preliminary design showing large projected area needed in flap 62

4.12 Comparison of previous vs updated external actuator design 63

4.13 Final design of the Internal-External sleeve 64

4.14 Final design of the Internal-External actuator 65

4.15 Compilation showing the insertion of the Internal-External design 66

4.16 Top view of the nozzle profile outlet within the flap skin 67

4.17 Assembled view of the External design 68

4.18 Sleeve design with one part 69

4.19 Sleeve design with multiple parts 70

4.20 Representative model of a wing flap 71

4.21 Assembled view of flap with the FO 71

4.22 FO actuator 72

4.23 Actuator (left) and Cover (right) 73

4.24 Tongue shown on actuator) 73

4.25 Final sleeve design 74

4.26 Final sleeve design backside 75

4.27 Final design visual mockup 76

4.28 Cutout for FO insertion 76

4.29 FO parts from left to right: sleeve, actuator, actuator cover 77

5.1 FO ANSYS connections 79

5.2 Refined mesh for FO sleeve 80

5.3 FO deformation 80
5.4 FO stress 81
5.5 Actuator connections labeled for the simulation 82
5.6 Actuator mesh, with refinement regions circled 83
5.7 Actuator deformation 83
5.8 Actuator maximum stresses 84
5.9 Actuator fatigue life 85
5.10 Beam fatigue stresses 86
5.11 Beam fatigue deformation 86
5.12 Beam sleeve fatigue life 87
5.13 Beam sleeve fatigue stresses 87
5.14 Actuator IM short shot 88
5.15 Actuator IM cooling time 89
5.16 Refined Actuator IM sink marks 90
5.17 Actuator Cover IM fill time 91
5.18 Actuator Cover IM pressure vs time 91
5.19 Sleeve IM weldline 92
5.20 Sleeve IM weld lines 93

6.1 Geometric bounding box for the sleeve 99
6.2 Part Angle Symmetry 102
6.3 Design Configurations Unit Cost 105
6.4 Design Configurations Unit Cost Zoomed 106

7.1 Final design visual mockup 109

7.2 FO parts from left to right: sleeve, actuator, actuator cover 109

7.3 Design Configurations Unit Cost 111

SUMMARY

Active flow control (AFC) devices have been proven to reduce drag and delay stall on commercial aircraft. This leads to lower fuel usage and thus reduced flight costs. However, there is a large uncertainty as to how to integrate AFCs into aircraft, specifically those with composite structures. Additionally, the cost of manufacturing AFCs for large scale production has not been previously studied.

In this thesis, a design concept for the attachment of a fluidic oscillator (FO) to a composite aircraft structure is investigated. A systematic approach from the conceptual design to the final design is performed using different design tools.

Axiomatic Design is first used to generate the functional requirements and design parameters. Following that, morphological charts are used to generate conceptual designs. These designs are then compared to select the top design from each category through the use of a sensitivity analysis and design of experiments. A final design is created with both CAD and physical models. Design validation of the final model is conducted using finite element analysis and mold simulations. A cost analysis is performed to select the most cost-effective design configuration based on large volume FO production.

Through the design validation and cost estimation, the final design is shown to be feasible for large volume manufacturing.

CHAPTER 1

INTRODUCTION

During flight, it is necessary to reduce drag and delay stall over the aerodynamic surfaces of the aircraft. Stall on wings occurs when the critical angle of attack has been reached; further increasing the angle of attack does not increase lift but rather decreases it. Flow separation is always present on an airfoil in a moving jet stream, but it is negligible compared to the attached flow at low angles of attacks. As the angle of attack increases, the flow separation also increases until the critical limit is reached, and then less lift is generated due to the decreased attached flow. This is illustrated in Figure 1.1 [1].

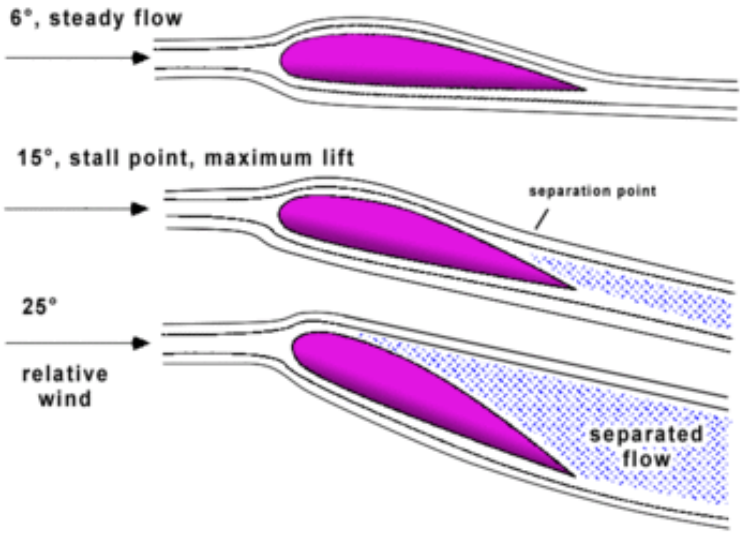

Figure 1.1: Attached flow versus separated flow on an airfoil at different angles of attack [1]

One of the most common methods to delay stall is the use of flaps. Flaps are smaller airfoils that are attached to the trailing edge of the main wing airfoil that work to combat stall. Flaps function by increasing the overall camber of the entire wing so as to prevent flow from separating at higher angles of attack. Some flaps also create more lift through the use of a larger wing chord thus contributing a larger surface area for lift force generation. Flaps

are usually activated during takeoff and landing so as to increase lift and thus increase the angle of ascent/descent. However, flaps inherently create drag, and while this is not usually a favorable condition, it does provide a benefit during landing as it reduces the velocity of the aircraft.

There are many flap variations, as shown in Figure 1.2, that vary based on sliding movement, hinge movement, and slot existence [2]. Simple flaps are the most basic, consisting of a small airfoil attached to the end of the main airfoil that rotates to increase the wing camber thus contributing more lift. Slotted flaps benefit from the ability to pass high pressure air from the bottom wing surface to the top to keep the flow attached, thus reducing stall. Split flaps consist of a smaller airfoil attached to the bottom end of the main airfoil that is also hinged. This type of flap differs from other flaps in that its main purpose is to introduce more drag rather than create lift, which is helpful during landing when more drag is needed to slow down the aircraft. Fowler flaps, which are quite common on commercial aircraft, slide out and then hinge downward so as to increase the wing chord which contributes to an increase in lift.

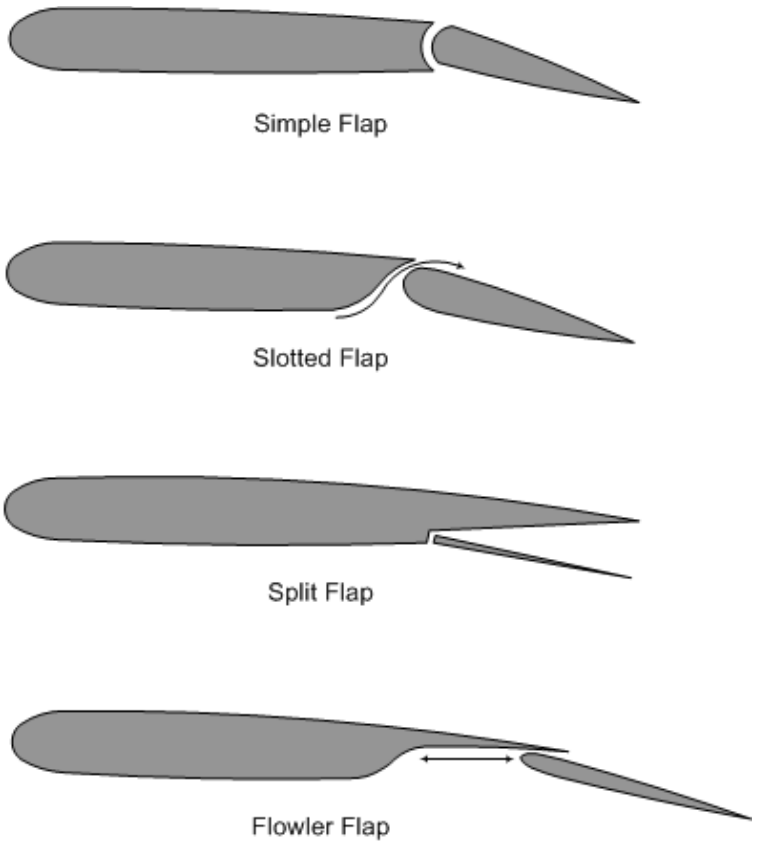

Figure 1.2: Different variations of aircraft flaps [2]

While flaps lower the overall flow separation across the entire wing, there is still local flow separation that occurs at the flap wing surface. This is because the air approaches the leading edge of the flap at a large angle of attack, and so is more prone to separation. This separation can be combated by introducing a vortex generator that invigorates the boundary layer stream by mixing free stream air with it which increases the boundary layer momentum. Active flow control (AFC) can be used to create these vortices by implementing a fluidic oscillator (FO) that creates a sweeping jet that blows energized air into the boundary steam to re-energize it. The introduction of the energized air from the AFC device prevents the flow from separating and thus delays wing stall. An AFC device may be inserted into the front section of a wing flap as shown by the arrow in Figure 1.3.

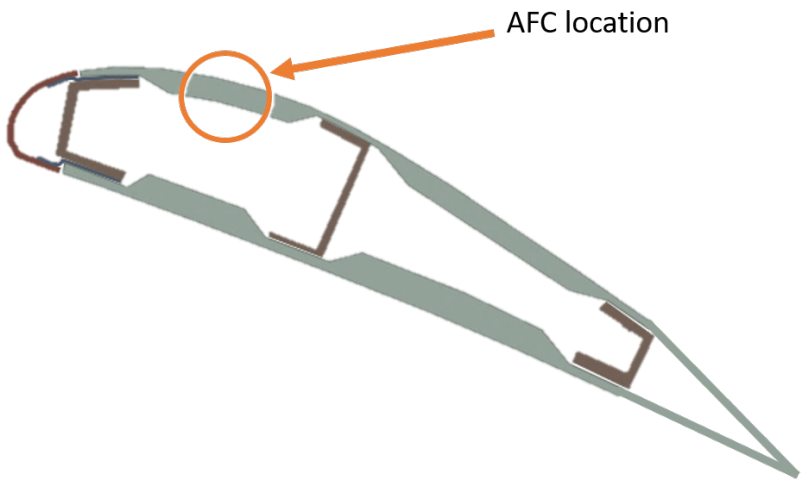

Figure 1.3: Wing flap showing an ideal AFC insertion location

There are numerous methods for creating the active flow control device, including using an actuated air inlet flow to create an oscillating fluid, or using a piezoelectric actuator to drive the motion. This paper focuses on an AFC device that uses fluidic oscillation. This AFC device is composed of three sections that combine to create a sweeping jet. The first is an inlet which receives the air from an air supply tube. This air is then circulated in the second section consisting of the actuator cavity. The air is then ejected out of the AFC device through the exit nozzle, which constitutes the third section. As the air exits out, the air attaches to either side of the exit nozzle walls, which is explained by the Coanda effect. This change in attachment causes the oscillating jet produced by the AFC.

Numerous AFC devices using oscillating jets have been developed since the initial research in sweeping jets at the Harry Diamond Research Labs in the 1960s [3] Since then, numerous aerospace companies such as Airbus and Boeing have researched the implementation of AFC devices into wings and wing flaps to keep flow from separating [4] [5] [6] [3]. These tests have proven successful in increasing lift by delaying stall and have shown the potential of AFC devices to reduce costs by allowing downsizing of certain aircraft components [3]. However, all of these tests were conducted on airfoils constructed of metal, rather than composite materials, which pose new issues to address.

Composite materials have become much more prevalent in the aerospace industry, com-

prising more than 50% of an aircraft compared to the 5% previously used in the 1970s [7]. The increase in the popularity of composite materials is explained by its high strength to weight ratio, being greater than steel or alumninum. Composites also are resistant to corrosion and have better fatigue life compared to metals [8].

However, in dealing with composites, new problems surface with regards to attachment methods. Previously, fasteners were utilized as the primary method of joining metal sheet bodies on aircraft, but continuing to do so on composite materials has greater consequences as they compromise the fiber strength in addition to introducing stress concentrations. Thus, if AFC devices are to be installed into composite wings, there is a need to develop a new approach for fast and reliable attachment. This method may be utilized for the general attachment of AFC devices into aircraft wings, fuselages, and empennages. It may also be used for other composite bodies where flow separation is critical such as racecar wings and undertray components.

This thesis will first provide a summary of background information and literature review relating to composites, AFC devices, and Axiomatic Design. Next, the design methodology regarding Axiomatic design will be explained in detail to discuss the design process used in this work. Designs will be presented and then down-selected until the final design is reached. Finite element analysis and mold flow simulations are conducted to validate the final design, followed by a manufacturing cost analysis. Finally, the results and their implications will be discussed in the conclusion along with suggested future work.

CHAPTER 2
BACKGROUND

In order to better understand the project scope, a review of the research literature is presented. First, composite materials and their processing and joining techniques are reviewed. Following that, previous work on fluidic oscillators is described focusing on their manufacturing processes. Finally, an introduction to Axiomatic Design is presented, which lays the groundwork for the design conceptualization in this project.

2.1 Composites Review

Composite materials consist of a combination of two or more materials that, when combined, create a material with unique properties compared to its constituents. The term 'composites' usually refers to fiber reinforced polymers where fibers such as aramid, carbon, or fiberglass combine with a polymer resin such as epoxy to create the composite material. Composites prove useful in situations where weight savings is critical, such as in the aerospace and automobile industries. This is due to their high strength-to-weight properties, which are useful for replacing traditional metal parts to reduce weight while still maintaining strength. However, composites differ from traditional metals in that their properties are highly dependent on how the material is manufactured. Careful consideration of the fiber orientation and layup process during manufacturing must be made to meet target strength demands. Additionally, different types of reinforcement can be used for different situations.

2.1.1 Composite Properties

Composites are frequently used to replace traditional metal sheeting on aircraft due to their high strength to weight ratio. However in order to meet this strength demand, particular

attention has to be focused on the manufacturing process. During the manufacturing of a composite, fiber orientation is a key concept, as fibers exhibit high strength and stiffness when loaded in their fiber direction. Fibers are often fabricated into layers in which each layer aligns fibers in one primary direction. The stacking of the lamina can be done in alternative fashions with unidirectional laminates (UD) all having the lamina in the same direction (90-90-90-90). Cross ply multidirectional (MD) laminates have each subsequent layer in an alternate orientation angle (0-90-0-90). UD laminates exhibit a linear relationship along the stress strain curve until failure, whereas as MD laminates behave nonlinearly [9]. With regards to MD angle ply laminates, orientation angles closer to 0° (the angle of loading) show an increase in stiffness with an increase in load, while angles closer to 90° show a decrease in stiffness.

Woven fabrics consist of interlacing yarns of fibers with each other in an over-and-under pattern with the warp defining the longitudinal direction and the weft for the width direction. Variations in the distance that the warp goes over the weft and back under creates numerous different weave patterns that vary based on their pliability, strength in a certain direction, and porosity for air and wetting. Woven fabrics excel in that they provide more balanced properties compared to UD laminates, and greatly decrease the fabrication time when compared to MD laminates because the laminates are not orientation specific. However, they have the disadvantage of lower strength and modulus properties when compared to non-woven laminates [9]. Because of this disadvantage, non-woven laminates are more commonly used, especially in aerospace, as material strength is a vital performance characteristic.

UD and MD laminates also differ in how they react to drilling and orthogonal cutting. With regards to trimming, chip formation is very similar between UD and MD laminates, however MD laminates showed less damage for the 90° and -45° plies [10]. In both laminates, 0° orientations showed more fracture along the fiber/matrix interface, whereas angles greater than exhibited failure due to compression shear perpendicular to the fiber axis [11].

When comparing the effect of feed rate for drilling laminates, UD showed about a 30% enlargement of average spalling size [12]. With regards to the research in this thesis, MD laminates are used, but an understanding of the reason for failure and of how it differs compared to UD is important.

2.1.2 Composite Post Processing

In order to attach an active flow control (AFC) device to a composite wing structure, careful consideration to post-processing and machining is important as they strongly affect the structural integrity of the composite material.

Drilling/Rotary Machining

Drilling is used as an assembly tool to create holes for the insertion of mechanical fasteners such as rivets. Drilling is a commonly used technique, specifically in the aerospace industry as more than 12,000 holes are drilled on a single wing set during manufacture [13]. The majority of drilling operations have taken place on metal airplane structures, but composite materials have begun to become more prominent in aircraft because they are lightweight and strong.

In metal machining, drilled holes create local stress concentrations, but do not affect the material properties. Whereas drilled holes compromise the structure of composites as they lead to delamination and breakage of the fibers as the drill bit enters the part. Delamination of the bottom layer also occurs as the drill pierces the exit side and moves freely into the space underneath, and so a holding fixture is used to prevent back-side breakout [14]. Several factors affect drilling including the type of resin, type of fiber, fiber orientation, type of structure, and material thickness, as each variable has to be taken into consideration before machining. Diamond or carbide tipped tools and high cutter speeds are used to limit the damage of rotary machining on composites.

Abrasive Waterjet

Abrasive waterjet cutting (AWJ) involves the use of highly pressurized water (up to 55,000 psi) and the addition of an abrasive garnet to cut through a material; these components are shown in Figure 2.1 [15]. AWJ is versatile in that it can cut a wide variety of materials including ceramics, composites, steel, and titanium. AWJ machines have advanced over time incorporating five axes of rotation for complex parts, and with tolerances of up to 0.003" [16].

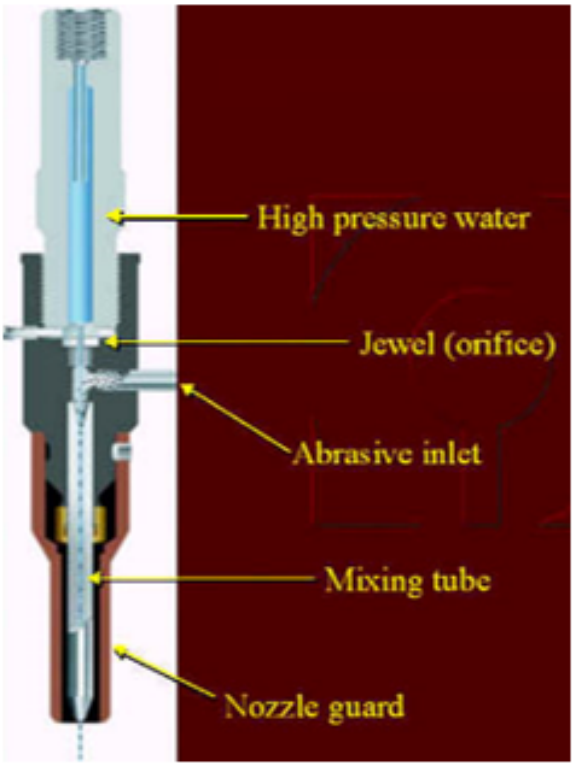

Figure 2.1: A standard waterjet cutting machine with the labeled components shown [16]

The use of AWJ for cutting composite materials has grown in popularity due to its accuracy, speed, and non-toxic nature. Aerospace companies such as Boeing have used AWJ to cut components such as the "center wing box, wing skins, spars, stringers, fixed leading edge, vertical stabilizer, horizontal stabilizer, landing gear components" among other things [17]. AWJ excels in that it can cut without creating a heat affected zone, which creates localized damage in a part. AWJ can also cut composites without creating toxic

gases that are associated with heat-affected regions. A downside to AWJ is the issue of delamination. Similar to rotary tools, AWJ must pierce the material first before cutting, and it is during piercing that delamination is most severe. The shock wave impact of the water in the initial cutting phase penetrates the brittle composite, and it is from this that the crack propagates. Delamination can be minimized by predicting this estimated crack growth based on waterjet settings [18]. Delamination is also limited by having the waterjet stream begin the piercing operation outside of the part or inside a predrilled hole in the part. Most AWJ machines contain a drill head along with the waterjet head to allow piercing with a drill before cutting with the water.

Laser Cutting

Laser cutting involves the use of a focused beam of light that burns and then cuts the laminate. Highly detailed cuts can be made due to the accuracy of the laser and because no cutting force is required; therefore, it is widely used for very thin and fragile pieces. Parts thicker than 0.3" show difficulty in cutting due to the inability to remove deeper layers of waste materials. When compared to AWJ, laser cutters have faster speeds (25-120 ipm) and can cut part features with a tight tolerance of 0.006" [14]. However, heat affected zones are an issue and charred edges may form on the work piece.

2.1.3 Composite Joining Techniques

In order to attach the FO to a wing structure, current composite attachment methods have to be understood. The two main composite attachment mechanisms are mechanical fasteners and surface adhesives. Although adhesives are the primary method for joining composites to composites, fasteners are used in some industries for their ease of use and familiarity.

Mechanical Fasteners

A mechanical fastener is a component that joins two or more items together; rivets are a common type of mechanical fastener. Rivets are frequently used on aircraft components as they offer a quick and inexpensive solution to combine two sheets of material together. While fasteners have been used widely for metal airplane bodies, they have been used on composite plane structures including the wing and fuselage through the use of composite specific rivets [19]. These rivets are different from traditional rivets in that they have a large blind side footprint and use Monel or stainless steel so as to prevent galvanic corrosion of the composite [20].

Mechanical fasteners excel in that they involve minimal surface preparation and have quick assembly and disassembly times. They also allow for easy inspection and quality control. However, mechanical fasteners do contribute weight and create local stress concentrations. Additionally, installed fasteners disrupt external surfaces, interrupting the smooth flow of air, which is important for a wing surface. In dealing with composites, fasteners create fiber discontinuity and could expose fibers to dissimilar material leading to galvanic corrosion with aluminum or cadmium plated fasteners, though this latter issue is usually remedied by using a non-conductive fastener coating or by using fasteners made of titanium, composite, or nickel [14]. While composite-specific rivets are more suited than traditional rivets for composite structures, they still are not the most effective method for joining parts as they require drilled holes, which compromise a composite's structural stability.

Surface Adhesives

Adhesives have been used widely to join dissimilar materials, especially in the field of composites due to their non-destructive nature. Surface adhesives are widely used with composite materials as they create a joint feature without the use of machining that could cause the material to fail through delamination or the introduction of additional stress concen-

trations. This has caused adhesives to become the primary joining method for composites to other materials including metals and other composites [14]. Adhesives have been very widely used in the aircraft industry since their introduction to de Havilland aircraft during WWII. Adhesive joining has continued to increase in aerospace with the introduction of more composite parts that require joining to other materials as shown by the schematic in Figure 2.2 [21].

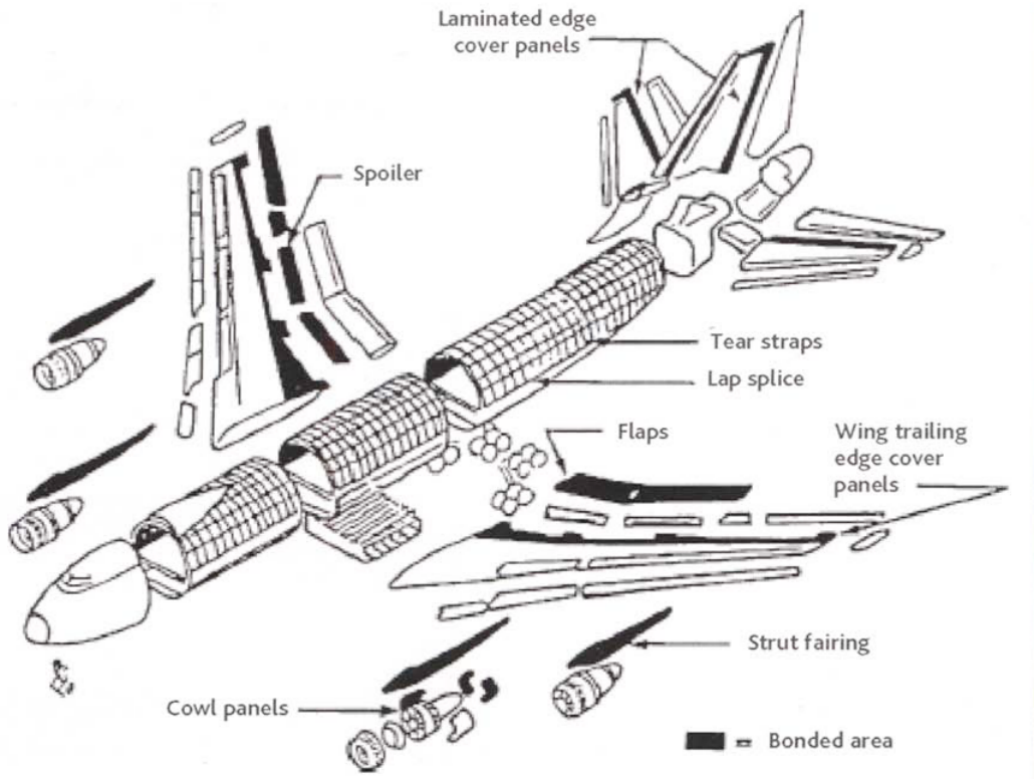

Figure 2.2: Diagram showing the high usage of adhesive bonding on a Boeing airplane [21]

Typical adhesives use polymer matrices such as Epoxy adhesives, rubber based adhesives, acrylic adhesives, and sometimes hot melt thermoplastic adhesives. Epoxies are the most common adhesive and have high bond strength and environmental resistance [14]. Surface adhesives are good because they distribute the load over a large surface area compared to a localized stress point. Surface adhesives also provide the advantage of joining irregular surfaces together while maintaining a smooth surface finish, unlike fasteners which disrupt the smooth surface. In terms of weight and cost, adhesives tends to excel when

compared to traditional mechanical joining methods. Adhesives also provide resistance to vibrational stresses and flexure, and have a longer fatigue life.

Although surface adhesives excel in many aspects, they require long surface preparation times that include surface cleaning and surface abrasion. After the adhesive is applied, high heat and pressure is often required to bond the materials. In addition, surface adhesives create permanent bonds compared to mechanical fasteners, and so inspection is more difficult. Due to the permanent bonds, disassembly is uncommon as disassembling the surfaces could damage the parts [14].

2.2 Current AFC Technologies

Active flow control (AFC) devices have been studied since the 1960s [3] to improve flow along a surface through the introduction of pulsed air to stimulate fluid flow. With AFCs, flow is maintained along the surface of the inserted object through the introduction of a vortex from the device that invigorates the boundary layer stream along the inserted object's surface. This vortex mixes in with the free stream to speed up the boundary layer momentum and keep the flow attached to the surface. Pulsating AFCs have been developed using fluidic or piezoelectric actuators to produce the oscillating jet as shown in Figure 2.3.

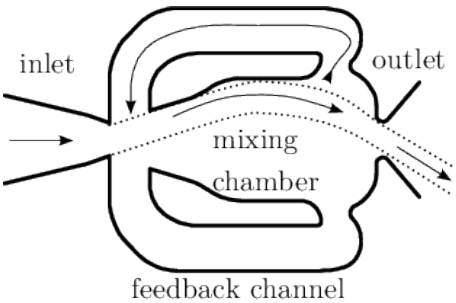

(a) Fluidic actuator [3]

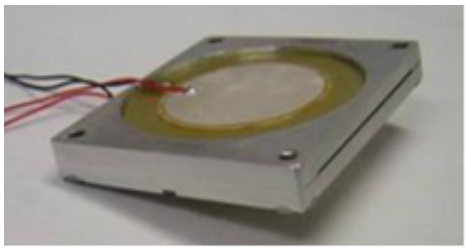

(b) Piezoelectric actuator [22]

Figure 2.3: Two types of AFC actuators

Piezoelectric AFCs use piezoelectric materials to produce fluttering air at the device's surface. A piezoelectric actuator device is shown on the right of Figure 2.3b [22]. Piezo ac-

tuators do not require a compressed air source and so, no piping is required for it. However, piezo actuators are limited to low-medium speeds that coincide with the device's resonant frequency [23].

Fluidic oscillators (FO) use pressurized air as the intake source and expel air out of the nozzle as a pulsating jet. Fluidic devices use the Coanda effect to produce oscillating air that attaches to one side of the nozzle exit wall, before switching over and attaching to the other side. A FO device shown on the left of Figure 2.3a is shown with labels identifying key points in the creation of the oscillating jet stream [3]; here, the jet is shown to attach to the bottom of the exit nozzle. FOs have been tested on models to improve air flow characteristics, specifically of a form to keep external flow from separating along the surface [24]. This has caused AFC devices to be studied for their application in both aircraft and non-aircraft vehicles.

2.2.1 Aerospace Application

Active flow control devices have been studied by several companies and institutions over the years. NASA sought to reduce the disruption in laminar flow in 1991 when it fitted an F-16XL with a suction device in the wing [25]. This research proved successful in introducing laminar flow through numerous laser-cut holes that sucked in the turbulent layer over the wing skin. A "glove" consisting of a thin titanium sheet with the microscopic holes covered about 25% of the wing to provide the suction interface. While this research was successful in creating laminar flow on supersonic aircraft, the "glove" that was used was solely for experimental purposes as the goal of the NASA program was to provide data for a proposed supersonic civilian transport jet.

Several aerospace companies have worked on developing FO technologies in order to increase lift for landing approaches and to reduce aircraft component weight. Past research at the Technical University of Berlin has shown the feasibility of using active flow control in low Reynolds number flows [26]. However these tests were conducted on limited model

sizes and with Reynolds numbers that were too low to compare to realistic full-scale flight conditions. Other research, conducted by Airbus Operations and the German Aerospace Center, worked on utilizing pulsed blowing FOs in a wind tunnel to provide more computational results that more closely match realistic flight conditions using a high lift model [4]. A more accurate wing scale model was used that had the FO inserted inside, as shown in Figure 2.4. Despite using a more accurate scale model, there were still limitations encountered in the tunnel testing that disturbed the signal frequencies leading to smaller successive lift increments during testing. With regards to the implementation of the FO devices in both of these experiments, exit slots were cut out of the metal wind tunnel model and the devices were placed inside of it, requiring no novel approach to integrating the FO device.

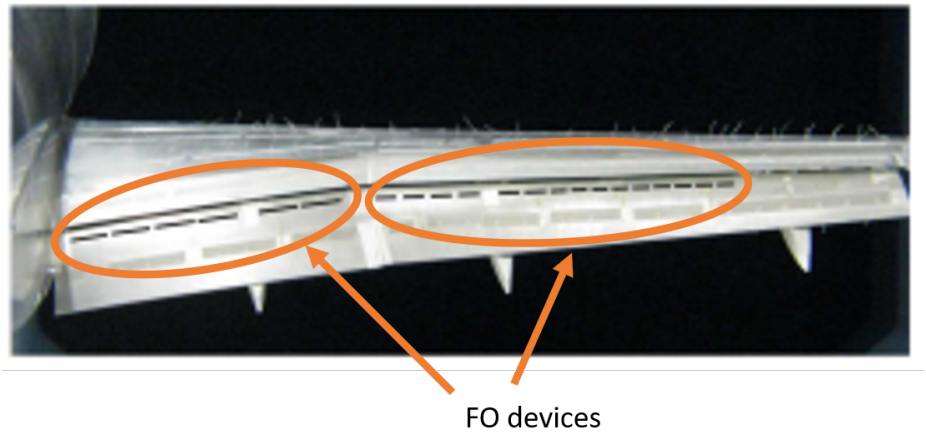

Figure 2.4: Wing model utilizing pulsed blowing FO devices [4]

Boeing also worked on the implementation of FO devices into wings to keep flow attached. In a joint project alongside NASA, Boeing successfully implemented rows of FOs into a full scale 757 vertical tail that was tested in a full scale wind tunnel [3]. The results showed that there was a 20-30% side force enhancement due to the performance of the FOs. In this test, the actuators were installed into 3/8" thick panels that were attached on top of the vertical tail wing surface. This resulted in a noticeable "bump", shown in Figure 2.5, but as this was for testing purposes, future designs seek to eliminate this bump by installing the actuators within the wing.

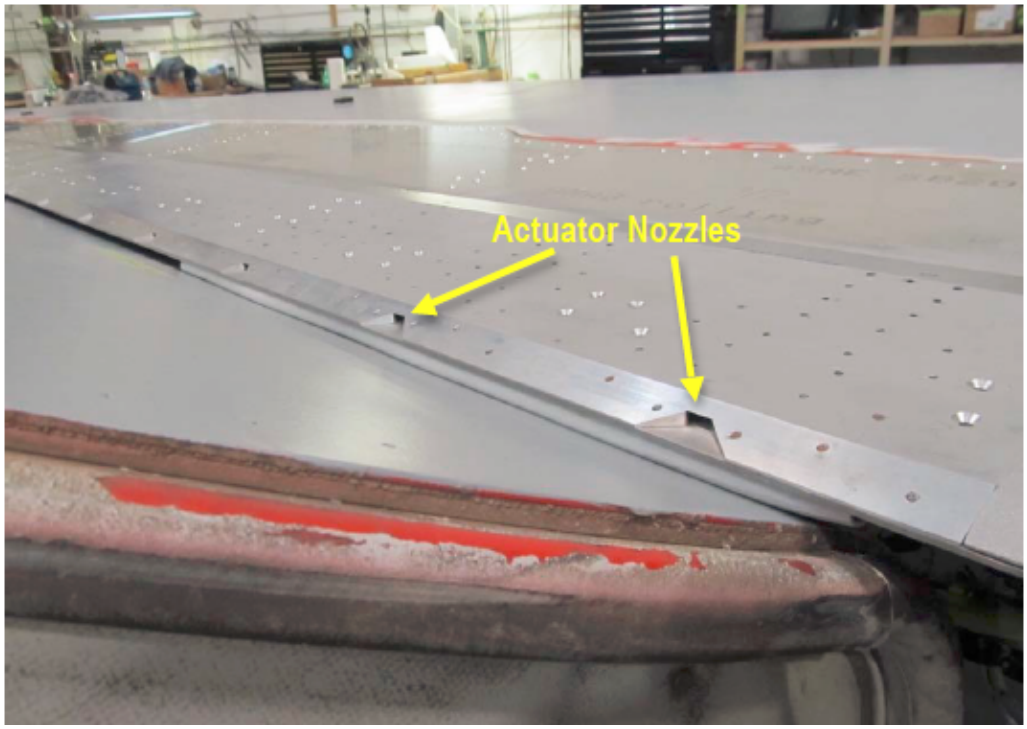

Figure 2.5: Boeing vertical tail with FOs installed [3]

Research into the integration of FO devices in composites has also been conducted. Through a joint project with Boeing, research at the Georgia Institute of Technology showed the implementation of rows of FO devices into a composite wing flap [27]. This research focused on the integration of the FOs by embedding the devices into the composite skin. Several alternative configurations were studied including the insertion of the devices from the top or the side and embedding them into the composite skin, or by installing them from on top into a wing groove and applying an adhesive for attachment. While these configurations provided feasible solutions for integrating the devices into the skin, they did not allow for serviceability as the attachment methods were permanent.

Research was conducted on the attachment of a FO into a composite wing-flap front section by Li at the Georgia Institute of Technology [28]. Li created a design, shown in Figure 2.6, that attached a fluidic oscillator into the bullnose section using a peripheral bracket to attach the FO to the front spar. However, this design focused on attaching the FO to a non-structural, fiberglass part of a wing flap, where it will be more accessible for

servicing.

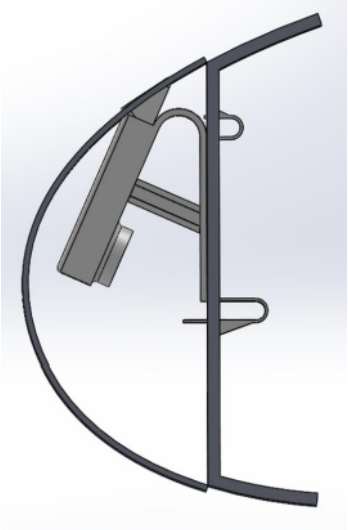

Figure 2.6: FO attached to non-structural bullnose wing region [28]

Research at TU Dresden in Germany integrated an AFC system into a carbon fiber reinforced wing flap. An additional spar was placed inside of the flap and screwed into place. The AFC was attached to the underside of this spar as seen in Figure 2.7. Although plastic material was considered, the spar was made out of aluminum as the plastic was deemed too flexible and would lead to issues with torsion and bending [5]. Additionally, the AFC parts were constructed from aluminum.

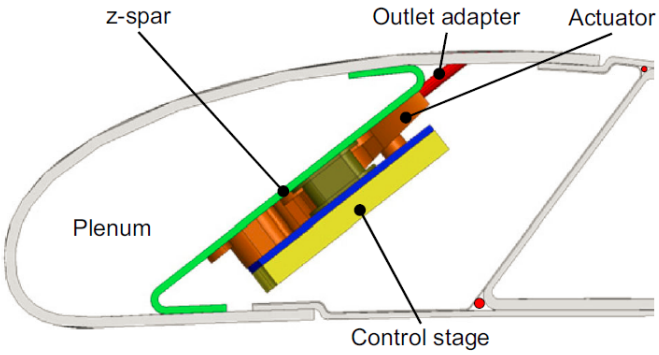

Figure 2.7: AFC attached to z-spar near leading edge [5]

2.2.2 Non-Aerospace Applications

Active flow control devices have also been used in non-aerospace applications to reduce drag. AFC devices in the form of "Suction and Oscillatory blowing" actuators have been demonstrated to aid in the reduction of fuel consumption on heavy ground vehicles. Actuators were placed on the top edge and sides of the rear end of the truck trailer to both blow and suck air to reduce turbulent air in the wake of the vehicle. During road tests in the US, fuel consumption was reduced by 1.0-3.5% depending on the truck speed [29]. During these tests, the AFC devices were placed into a metal strip array which was subsequently bolted onto the end of the trailer, as seen in Figure 2.8. The devices are shown on the truck in the figure on the left, while the right image shows a closeup view of the AFC array. Since the focus of the experiment was on the feasibility of this new technology, the emphasis was placed on how well the devices worked in real time rather than on the integration of the device into the truck.

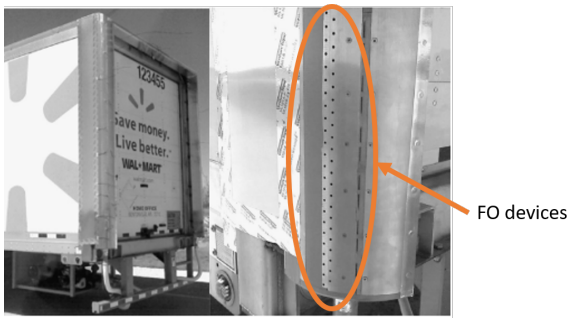

Figure 2.8: AFC devices attached to the rear end of the truck [29]

2.2.3 FO Manufacturing

For all prior fluidic oscillator research, actuators were created for the individual prototype testing but significant research has not been conducted on the manufacture of FOs for large scale production. Due to the complex geometry inside of a fluidic oscillator and its hollow chambers, FOs are generally manufactured in multiple parts. 3D printing has facilitated enhanced manufacturing by successfully creating complex geometries in a single part. Prior

research has used 3D printing techniques to create the FO's small and complex geometries, and to reduce overall part count [27] [28].

Manufacturing methods for micro-fluidic oscillators, which are similar to FOs have also been studied. Research by Becker provided an overview of several methods including 3D printing, injection molding, precision machining, and thermoforming [30]. Thermoforming, which heats up a polymer and presses it into a mold, was found to be effective for small to medium scale production, whereas injection molding was effective for large scale production.

If the FO device must be made in more than one part, then bonding techniques would need to be used. Past research in the bonding of thermoplastic micro-fluidic devices has shown that adhesives, thermal fusion, and solvent bonding are effective [31]. Indirect bonding through the use of adhesives benefit from their high bond strength, low cost, and low temperature processing requirements. However, adhesives provide the limitation of potentially clogging the FO's micro-channels. Thermal fusion and solvent bonding are commonly used due to their low process complexity and low-medium cost. Due to the bulk polymer flow, care has to be taken so as to not deform the FO channel surfaces during the high temperature and pressures used. Ultrasonic welding is also a good technique for localized bonding, but its high equipment cost prevents its widespread application.

FO manufacturing costs have been studied for different manufacturing methods at several batch quantities as shown in Figure 2.9 [24]. Thermoforming was once again found to be effective for small quantities, while injection molding and compression molding were effective for high part volumes in excess of 10,000 parts. Li also conducted a cost analysis for three FO designs for a non-structural wing region [28]. 3D printing was found to be useful for small part counts, while injection molding was more cost effective for part counts larger than 1000 parts.

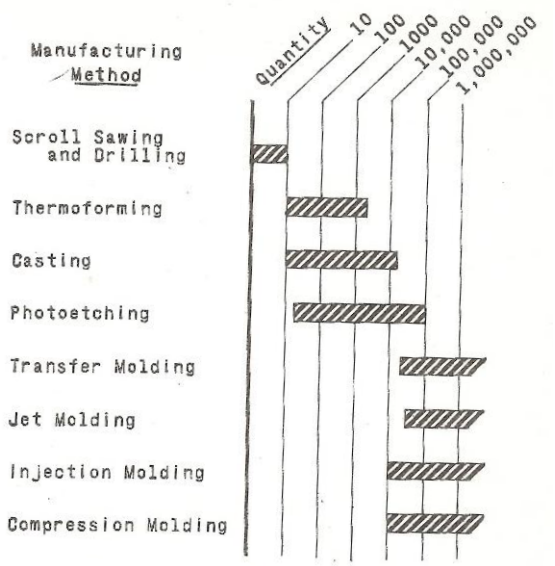

Figure 2.9: FO costs for different manufacturing processes [24]

2.2.4 FO Summary

In this section, a summary of active flow control (AFC) devices and how they function was provided. AFC devices in the form of fluidic oscillators and piezoelectric actuators were presented. Following that, examples of current designs exhibiting implementation of FO devices were also explored. Examples were presented in the application of aircraft and non-aircraft flow control. In both of these applications, FO devices were shown to reduce surface-induced drag on the vehicle, thus resulting in cost savings due to lower fuel requirements. However, in all of these examples, the devices were tested on a prototype model where FO devices were simply attached through mechanical fasteners to the current vehicle to test feasibility of the devices. None of these implemented the FO devices directly into a composite body, which poses new difficulties compared to attachment to traditional metal frames. This thesis will present a viable method for integrating FO devices into thin composite skins.

2.3 Axiomatic Design

Axiomatic Design (AD) is a design methodology introduced by Dr. Nam P. Suh in 1990, which drives design selection and consists of two axioms: the independence axiom and the information axiom [32]. The first axiom consists of maintaining independence between each functional requirement. The second axiom focuses more on the probability of satisfying functional requirements through the reduction of information. Together, the two axioms are used to generate feasible designs.

By implementing AD, a systematic approach to generating design concepts can be created while eliminating unsatisfactory designs and reducing complexity. This systematic approach eliminates the need to arbitrarily assign specific weights to certain parameters to help rank certain designs, and the approach can be implemented in a variety of industries including manufacturing, materials processing, and software. In this thesis, AD was utilized in the initial design stage to create design requirements and constraints. Design concepts were then developed through the use of 'zig-zagging' and design hierarchies.

To understand AD, one must first understand the various domains through which a design cycles. Figure 2.10 shows the four domains through which a designer progresses; however, it should be noted that while the cycle generally moves from left to right, it is an iterative process so the direction changes as needed. The customer domain is first and includes all of the customer needs (termed the customer attributes (CA)) in order to create customer satisfaction. These CA are then translated into functional requirements (FR), which describe what the product must contain. The third design domain is the physical domain where the design parameters (DP) are formulated to correspond to each FR. Lastly, the process domain includes process variables (PV), which identify the method that will create the DPs.

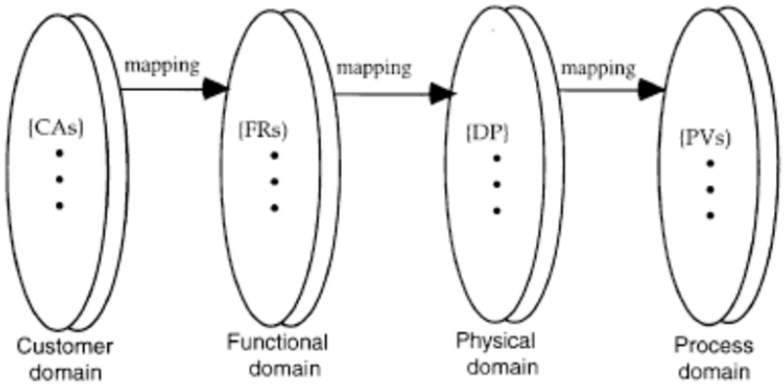

Figure 2.10: Four domains of the design cycle [32]

The first axiom states that each functional requirement must be held independent of other functional requirements. In order to do this, first, a list of CAs is generated and is then synthesized into a set of FRs that the final product must provide. Following that, a set of DPs is created specific to the product at hand. The next step in AD is to insure a decoupled or uncoupled solution, which means that each FR is independent of other FRs. This is visually represented through the use of a matrix of functional needs versus design parameters, as shown in Figure 2.11. Three sets of matrices show the functional requirements on the left of the equation and the design parameters on the right. The first matrix is an example of an uncoupled, the second shows a decoupled matrix, while the last one shows a coupled matrix [32].

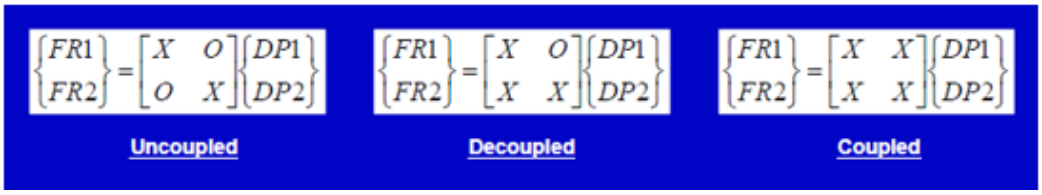

Figure 2.11: Three types of matrices in AD [32]

Ideally, there would be only one design parameter for each FR so that adjusting one parameter does not have any repercussions on other DPs. An uncoupled matrix is one in which there is an equal number of DPs and FRs; this is shown with a diagonal of values (X), with empty values above and below it (0), as shown in the first matrix in Figure 2.11.

A decoupled matrix is also a viable outcome as it means that parameters can be changed independently, as long as they are changed in an order that does not affect the independence of other variables. This is shown by a diagonal matrix with non-zero values beneath the diagonal, as in the second matrix of Figure 2.11. A coupled matrix is the least favorable outcome, as it shows that the FRs are not independent because the parameters are coupled to each other; this is seen in the third matrix in Figure 2.11, which has DPs associated with several different FRs producing a non-diagonal matrix. If a design produces a coupled matrix, then this design is considered to be an unsatisfactory option.

When creating DPs, it becomes necessary to delve deeper into a DP to show the design intent, which is accomplished by breaking down the highest level DP into multiple sub-levels [32]. These subsequent DPs can be further decomposed resulting in a system of hierarchies. In order to decompose these DPs, 'zig-zagging' between the functional domain and the physical domain is used. Starting off with a FR in the functional domain, a corresponding DP is created in the physical domain (1). Following that, a return to the functional domain is necessary to decompose the FR into FR1 and FR2 (2), which then requires a jump back to the physical domain to create DP1 and DP2 (3). This process continues (4) and (5) until no further decomposition is required or possible. This zig-zagging process is illustrated in Figure 2.12. The zig-zagging process includes moving from the functional domain (left) to the physical domain (right) and back in order to decompose FRs and DPs.

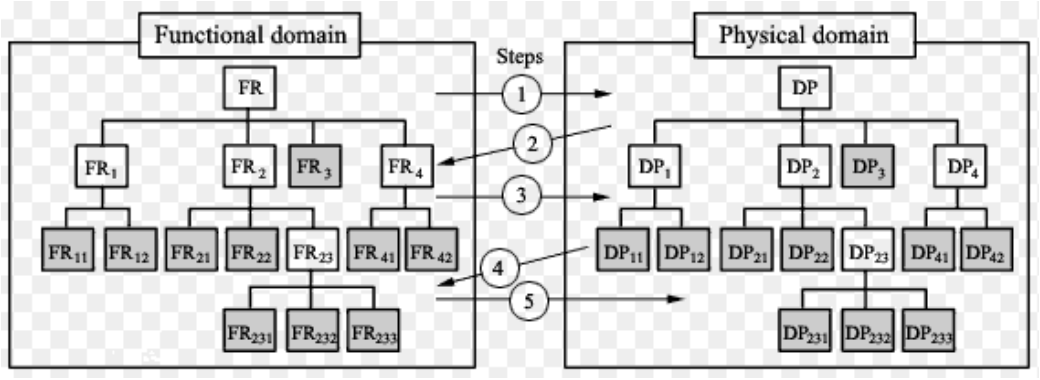

Figure 2.12: An example of the zig-zagging process [32]

After filtering designs with the Independence Axiom, the only viable designs are those that are uncoupled or decoupled and meet all the FRs independently. These are then evaluated to select the best design that most efficiently meets the FRs while reducing redundancy and complexity. The second axiom relies on the core idea of minimizing the amount of information for each solution. Designs that have the smallest information content constitute better designs; as in the realm of information theory, these designs have a lower entropy value. Entropy, measured in Shannons, is expressed as a probability and is characterized by the average amount of information contained in a message [32]. Minimizing this entropy correlates to a design that is less complex and has a higher probability of success. In order to measure the success, a design must contain a solution that meets the required FRs as completely as possible without redundancy. A probability distribution chart, shown in Figure 2.13 is used to visually support this concept of measuring a successful design.

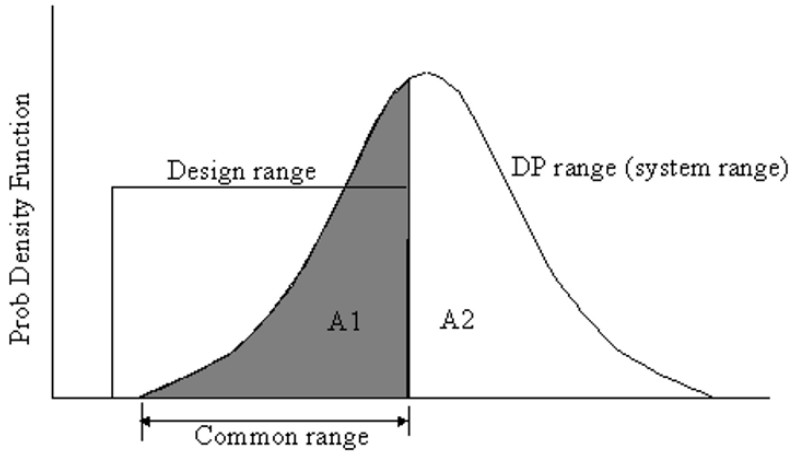

Figure 2.13: Probability Distribution vs Design Parameter [32]

In this chart, there are three major areas that constitute the design parameter: design range, system range, and common range. The design range shows the minimum and maximum tolerance values that the key functional requirement includes. The system range highlights the minimum and maximum tolerance values of the current design parameter, and the common range shows the overlapping region between the design and system ranges. Assuming a uniform distribution, a non-dimensional variable 'I' can be used to quantitatively

represent how well the current design meets the customer satisfaction. This is shown in Equation 2.1 as the logarithm of the ratio of the system range to the common range.

$$I = log_2(\frac{L_{sr}}{L_{cr}}) \tag{2.1}$$

Ideally, the value of *I* would approach zero, indicating a minimum amount of information content by showing that the common range matches the system range. Designs with an *I* value of infinity signifies that the design contains an infinite amount of information and that there is no overlap between the design and system ranges. There is no need for the use of a weighting factor as the functional requirement design range already specifies the importance of each parameter. Applying the second axiom to the designs that meet the conditions of the first axiom yields a corresponding value *I* for each design. These designs would then be compared to each other by prioritizing the design with the minimum information. In doing so, a systematic and quantitative approach is used to select between different designs without arbitrarily assigning weighting factors to each variable and then selecting them in that manner.

2.4 Chapter Summary

In this chapter, an overview of composites was presented including composite properties, post processing, and joining techniques. Next, current FO technologies were presented including applications for both aerospace and non-aerospace. Different methods for manufacturing the FOs were then discussed after. Finally, the Axiomatic Design process was explained. In the next chapter, Axiomatic Design is used to generate the functional requirements and design parameters for preliminary FO designs.

CHAPTER 3
DESIGN GENERATION

The first step in generating designs for the FO attachment was to identify the customer attributes and functional requirements. Axiomatic Design was used in the first phase of the design process to eliminate unsatisfactorily coupled designs. Morpholgical charts were used to generate feasible design solutions. Sketches were made of these designs, followed by 3D models. Costs were estimated for each of the designs, which were ranked based on their cost. Sensitivity analysis and design of experiments were conducted to evaluate the design rankings based on cost parameters.

3.1 Axiomatic Design

Axiomatic Design (AD) was used as a systematic approach to generate design concepts while reducing complexity and eliminating coupled designs [32]. Coupled designs have non-independent functional requirements (FR), where altering one FR necessitates changing another FR.

3.1.1 Customer Attributes

The first step in the AD process was to generate the customer attributes (CA) in the customer domain. The main customer needs were to create a working FO and to integrate that FO into a composite wing flap. These customer needs were synthesized into the three main CAs listed in Table 3.1. Using these CAs, top-level FRs were generated to create the product functions.

Table 3.1: List of Customer Attributes and their corresponding Functional Requirements

Customer Attributes	Functional Requirements
CA1. Manufacture a working FO	FR1. Produce FO with an oscillating jet stream
CA2. Integrate FO into a wing flap's internal structure	FR2. Mount FO to wing structure
CA3. Provide a connection across the wing skin to the free stream	FR3. Mount FO to wing skin

3.1.2 Decomposition

After generating the CAs and the high-level FRs, the next step involved mapping the conceptual work. This required a crossover to the physical domain to create the design parameters (DP) for each FR. First, high-level DPs were created for each corresponding FR. After that, a zig-zag approach was utilized to shift back to the functional domain and breakdown the top-level FR into sublevels. For each FR sublevel, a corresponding DP sublevel was generated. This process was carried out until all of the FRs were satisfied and would no longer need decomposition. The decomposed hierarchies for the FRs and DPs are shown in Table 3.2.

Table 3.2: Decomposition of Fluidic Oscillator Functional Requirements and Design Parameters

Functional Requirements (FR)	Design Parameters (DP)
FR1. Produce FO with an oscillating jet stream FR1.1 Carry loads on FO FR1.2 Handle internal pressure in FO FR1.3 Supply air to create jet stream FR1.4 Oscillate air FR1.5 Create required jet stream frequency FR2. Mount FO to wing structure FR2.1 Support FO in wing FR2.1.1 Carry loads on support FR2.1.2 Attach support to wing structural element FR2.1.3 Connect support to structure FR2.2 Connect FO to support mount FR2.3 Disconnect support from wing structure FR2.4 Disconnect FO from support FR3. Mount FO to wing skin FR3.1 Expel air from FO to free stream FR3.1.1 Connect Nozzle Profile Extension to skin FR3.1.2 Connect FO to Nozzle Profile Extension FR3.2 Seal FO-skin connection point FR3.3 Disconnect nozzle profile extension from wing skin FR3.4 Disconnect FO from nozzle profile extension	DP1. FO Design DP1.1 FO Material DP1.2 Wall Thickness DP1.3 Air supply system DP1.4 Manufacturing tolerance DP1.5 Surface roughness DP2. FO-Structure Connection DP2.1 Support Mount mechanism DP2.1.1 Support material DP2.1.2 Support attachment location DP2.1.3 Support-Structure attachment method DP2.2 FO-Support attachment method DP2.3 Support-Structure detachment method DP2.4 FO-Support detachment method DP3. FO-Skin Connection DP3.1 Nozzle Profile Extension DP3.1.2 Nozzle-Skin attachment method DP3.1.3 Nozzle-FO attachment method DP3.2 Sealant system DP3.3 Nozzle-Skin detachment method DP3.4 Nozzle-FO detachment method

As can be noted in the decomposed FRs and DPs shown above, the design process was divided into three main categories:

1. Manufacturing the actuator to produce an oscillating flow control device,
2. Attaching the actuator to the flap structure, and
3. Connecting the actuator to the flap skin.

FR1

The first FR involved accurately manufacturing an actuator that would be able to successfully oscillate the air and eject it from the nozzle. The manufacturing process had to be studied so that it would not degrade the actuator's performance. Machining tolerances and

the surface roughness were monitored, as small changes in the actuator geometry resulted in changes to the actuator performance [28].

The FO material had to be selected to withstand the temperature and forces that act on it. The part geometry, including the wall thickness, had to support the loads while also considering manufacturing. For example, parts with large wall thicknesses required long cooling times for injection molding.

The air supply system had to be connected to the actuator in a way that facilitated air flow into the chamber, while not interfering with attachment points to the flap. The air supply system used had to be pressurized in order to facilitate proper flow and to expel any particles or foreign object debris (FOD). Pressurized air from the engine exhaust would be suitable for this application and could melt ice that forms along the exit holes [33].

FR2

The second FR was to connect the FO to the existing flap structure. This was broken down into two main connection points and corresponding detachment methods: the attachment of the support mechanism to the flap, and the attachment of the FO to the support mechanism.

The support mechanism was defined as the support material that would be used to hold the actuator inside of the flap. This support mechanism would be attached to the flap. Therefore, information on the type of material from which it would be made, the location of the support connection point, and the method used to connect the support to the flap needed to be generated. The location of the connection points were the flap skin, flap spar, or flap rib. Attachment methods included both permanent, such as co-curing and co-bonding, and non-permanent, such as fasteners and snapfits.

After selecting the attachment method for the support mechanism, the attachment of the actuator to the support was selected next. The attachment options are the same as those for attaching to the flap structure. Detachment methods were then considered to determine how the FO would be removed for service. These included non-destructive options where the

actuator may be reused, and destructive methods where the FO would need to be replaced.

FR3

Finally, the third FR involved the connection of the FO device to the flap skin. In order to complete the connection of the FO to the free stream atmosphere, a nozzle profile extension would have to be created to connect the end of the actuator exit to the top surface of the flap skin. This involved two connection points for the FO: Nozzle to Skin, and Nozzle to Actuator. These two connection points necessitated both attachment and detachment methods as shown by DP3.1.2, DP3.1.3, and DP3.3, DP3.4, respectively. Additionally, a sealant system would be needed to ensure that these connection points were secure and did not leak air.

It is important to note that, although it would be possible for some of the designs to have the actuator and nozzle extension built together as one part, the DPs were still listed separately. This was done as AD follows a solution-neutral design approach.

3.1.3 Design Matrix

After generating the FRs and their corresponding DPs, a design matrix was created to show the relationships between the FRs and DPs, highlighted in Table 3.3. Squares with an X show that a certain DP affects a certain FR. Empty squares signify no relationship between a FR and a DP.

Table 3.3: AD independence design matrix

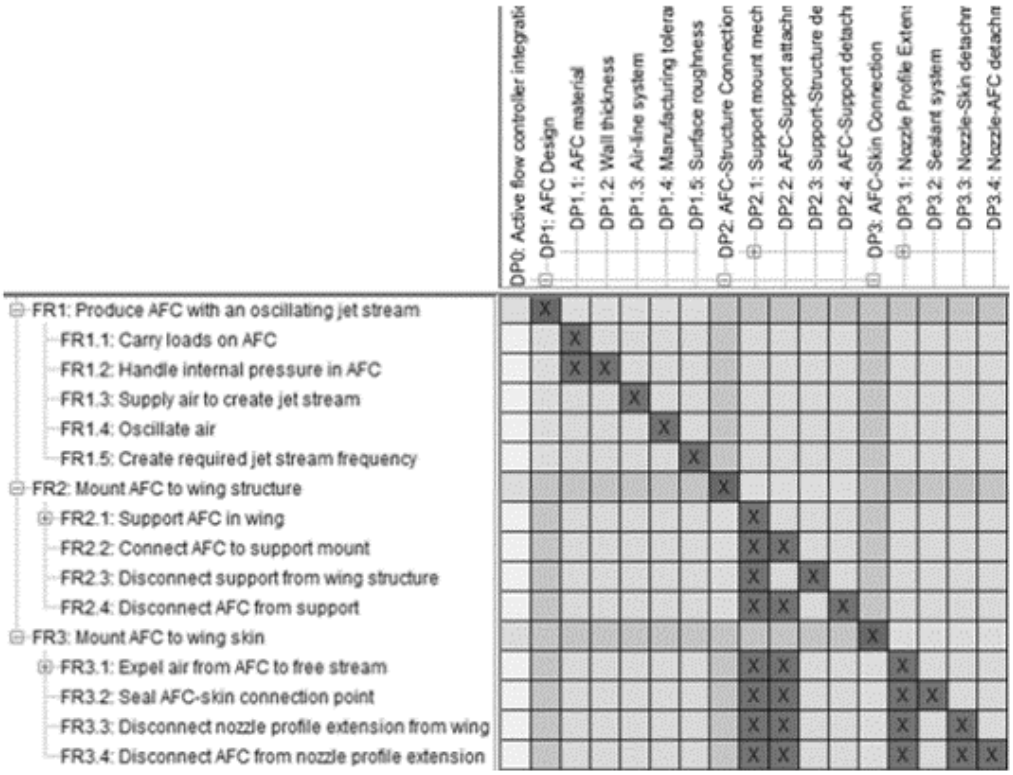

This matrix shows the relationship between the FRs and DPs. The ideal uncoupled design would have only a diagonal relationship with elements equal to zero both above and below the diagonal. With this diagonal configuration, each FR is satisfied by only one DP. Table 3.3 shows a lower triangular matrix where all the elements above the diagonal are equal to zero. This is significant as it shows that FRs are in fact independent of each other if the DPs are determined in the correct sequence. For example, FR1.2-Handle internal pressure in FO is related to both DP1.1-FO Material and DP1.2-Wall thickness. Wall thickness is dependent on the properties of the material, so if the wall thickness was set but the material was changed, the wall thickness would be subject to change. However, by selecting the FO material first, and then properly choosing the wall thickness, FR1.1 and FR1.2 are found to be independent of each other, as long as the sequence is maintained. This focus on the sequence of DPs can be seen again starting at FR2.1 which shows a relationship between the support mechanism connected to the flap, and all the subsequent attachment

DPs.

Constraints are needed throughout the AD process to ensure that DPs do not violate any specified limitations. Constraints were placed on the actuator device and on the actuator integration. Constraints on the device included temperature and pressure loadings, actuator sizing, and air supply ducting. Constraints for the integration involved the angle of the device with respect to the flap skin surface, actuator spacing along the flap span, and flap loadings. These constraints are summarized in Table 3.4.

Table 3.4: FO Constraints

Constraints
1. FO wing surface protrusion < 0.120"
2. FO can withstand temperatures: -54°C to 82°C
3. FO can withstand internal & external loads
a. Internal pressure: 30 psi ± 5psi
b. External pressure: 3.46 to 14.7 psi
c. Wing Loading > 136 lb/ft2
d. Vibration: 0-3 Hz
4. FO hole to be placed every 6-8" in skin along wing span
5. Air supply shall be at a temperature of 50°F ± 30°F
6. Air supply shall have a 3/4 in^2 cross section for each actuator
7. Wing skin is composed of composite CF material

3.2 Concept Generation

Axiomatic design laid the framework for determining solutions through the Independence Axiom. Doing so allowed for the creation of design solutions for each DP that were not coupled to each other. For each DP, viable solutions were listed to accomplish the desired function. Solutions were also required to fit the system constraints, such as allowing for servicing, manufacturing, and low cost. Table 3.5 lists the viable solutions for each DP.

For the materials, high grade thermoplastics were chosen for their high tensile strength and resistance to strain. Thermoplastics were used due to their high temperature resistance, short fabrication time, and the ability to be combined with fiber reinforcement. Polyether-ketoneketone (PEKK) and Polyetheretherketone (PEEK) were selected as options because

Table 3.5: List of DPs and possible solution options

	Parameter											
	FO Material	Air Supply System	Support Material	Support Attachment Location	Support-Structure Attachment	Support-Structure Detachment	FO-Support Attachment	FO-Support Detachment	Nozzle-Skin Attachment	Nozzle-FO Attachment	Sealant System	Nozzle-FO Detachment
Solution	PEEK	Plenum	Same as FO	Skin	Snapfit	None	Snapfit	None	Snapfit	Snapfit	Gasket	None
	PEKK	Individual FO	Different than FO	Wing Spar	Fastener	Destructive	Fastener	Destructive	Fastener	Fastener	O ring	Destructive
	Other			Wing Rib	Thermal Staking	Inverse of Attachment	Thermal Staking	Inverse of Attachment	Thermal Staking	Thermal Staking	Lip Seal	Inverse of Attachment
					Built-in Bolt		Built-in Bolt		Built-in Bolt	Built-in Bolt		
					Co-Cure		Co-Cure		Co-Cure	Co-Cure		
					Co-Bond		Co-Bond		Co-Bond	Co-Bond		
					Adhesive		Adhesive		Adhesive	Adhesive		
					Threaded		Threaded		Threaded	Threaded		
					Magnetic		Magnetic		Magnetic	Magnetic		
					Plastic Welding		Plastic Welding		Plastic Welding	Plastic Welding		
									None	One part		

they are widely used in aerospace applications due to their high strength, chemical resistance, and high temperature resistance. Supplying air into the FO was accomplished through either individually connecting air supply lines to each FO or connecting an air supply line to one plenum to which multiple FOs were attached.

For the insertion of the FO, the selection of the support attachment location was the first step of the design process as it was a deciding factor for many subsequent decisions such as attachment type and disassembly method. After selecting the FO insertion location, the attachment of the FO to the flap structure was decomposed according to AD. Designs for the FO attachment were broken down in the following order to prevent coupled designs:

1. Attaching the support material to the flap structure
2. Detaching the support material from the flap structure
3. Attaching the FO device to the support material
4. Detaching the FO device from the support material
5. Attaching the nozzle profile to the skin
6. Detaching the nozzle profile from the skin

7. Attaching the FO device to the nozzle profile

8. Sealing the actuator

9. Detaching the FO from the nozzle profile.

All of the DPs for attachment shared the same solutions; this was also the case for the detachment methods. Attachment options included the use of joining methods that could be applied to polymer and composite materials. Plastic welding indicated either ultrasonic or resistance welding. The use of electromagnets was initially listed as an attachment option but was later eliminated as it did not fall within the constraint of keeping the device at a low cost. Attachment methods dictated the detachment method because a material that was co-cured or co-bonded would generally be considered permanent, and thus non-removable (shown as 'None' in Table 3.5). "Destructive detachment" indicated that the attachment method would have to be destroyed to be replaced, such as in the case of mechanical fasteners that would need to be drilled out. "Inverse of attachment" denoted attachment methods that could be replaced by applying the same action in reverse such as unscrewing a threaded insert or releasing the snapfit pin to remove the snapfit insert.

For the sealants category, chemical sealants that are commonly used in aerospace applications, especially in the inside of a wing at fuel orifices, were initially considered. However, these options were eliminated as they would have violated the constraint of allowing the FO to be detached for service.

Once the solutions for each DP were selected, morphological charts were used to create design solutions. Using Table 3.5, one or more solutions was chosen for each parameter, and the combination of the different solutions for the parameters constituted a design solution. This can be seen in Table 3.6 with the highlighted cells representing the solutions that were chosen. This was systematically carried through to generate multiple uncoupled designs.

Table 3.6: Morphological chart solution selection for one sample design

	Parameter											
	FO Material	Air Supply System	Support Material	Support Attachment Location	Support-Structure Attachment	Support-Structure Detachment	FO-Support Attachment	FO-Support Detachment	Nozzle-Skin Attachment	Nozzle-FO Attachment	Sealant System	Nozzle-FO Detachment
Solution	PEEK	Plenum	Same as FO	Skin	Snapfit	None	Snapfit	None	Snapfit	Snapfit	Gasket	None
	PEKK	Individual FO	Different than FO	Wing Spar	Fastener	Destructive	Fastener	Destructive	Fastener	Fastener	O ring	Destructive
	Other			Wing Rib	Thermal Staking	Inverse of Attachment	Thermal Staking	Inverse of Attachment	Thermal Staking	Thermal Staking	Lip Seal	Inverse of Attachment
					Built-in Bolt		Built-in Bolt		Built-in Bolt	Built-in Bolt		
					Co-Cure		Co-Cure		Co-Cure	Co-Cure		
					Co-Bond		Co-Bond		Co-Bond	Co-Bond		
					Adhesive		Adhesive		Adhesive	Adhesive		
					Threaded		Threaded		Threaded	Threaded		
					Magnetic		Magnetic		Magnetic	Magnetic		
					Plastic Welding		Plastic Welding		Plastic Welding	Plastic Welding		
									None	One part		

3.3 Initial Designs

Once the designs were generated through the morphological charts, initial sketches were created. From these sketches, it became apparent that designs should be grouped into three general categories based on how the FO would initially be attached to the flap. Attaching the FO would be dependent on the accessibility to the flap and so the three categories were:

1. Internal Designs
2. External Designs
3. Internal-External Designs.

Internal designs involved attaching the FO to the inside of the flap structure and so necessitated 'internal' access to the flap. External designs would be ideal for retrofits, as the FO could be inserted and attached from the outside without requiring access to the internal structure. Internal-External designs would require internal access to attach the FO support structure, but the actuator itself could be inserted from the outside.

The differences between these categories are more apparent when discussing the assembly and maintenance of the FOs into the flap, as External and Internal-External designs

allow for actuators to be easily replaced without any disassembly of the flap, while Internal designs would require disassembling the wing flap to access the actuator. It was noted that different locations on the flap could require different methods of insertion based on accessibility, and so the categories were deemed useful to allow for more accurate comparison between designs of similar function. This split of designs into categories prevented designs from being eliminated due to their inherent categorical difference, and allowed for the best design from each category to be selected.

3.3.1 Internal Designs

Internal designs required internal flap access and had the support structure and the actuator attached to the inside of the flap. The overall layout for an Internal Design is shown in Figure 3.1. The design shows a structural sleeve that is permanently fixed to the skin through cobonding. The actuator then connects with a sealant, in this case a gasket, to the support sleeve through the use of a snapfit. A snapfit connection is shown in the figure, but a range of attachments such as fasteners or thermal staking may be used.

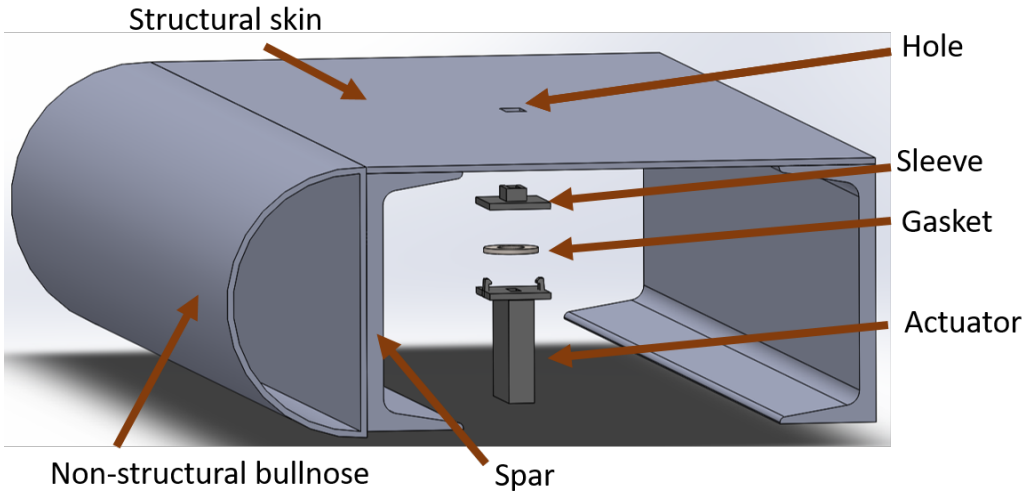

Figure 3.1: Internal design basic layout

The location of the sleeve in the flap box is also subject to change depending on flap access. An alternative design involves shifting the sleeve and actuator position towards the

front of the flap box so that the sleeve can fit into the spar rather than the structural flap skin region; this is shown in Figure 3.2. In this design, there is an alternative to drilling through the structural flap skin, and drilling occurs through the spar and the portion of the flap skin above the spar. However, this solution has a limited capacity of actuators that could be attached along the chord of the flap due to the small dimensions of the spar. Additionally, the angle of the actuator is limited by the spar's C-channel structure. Structural damage would have to be carefully assessed for the spar, as the holes can weaken its rigidity.

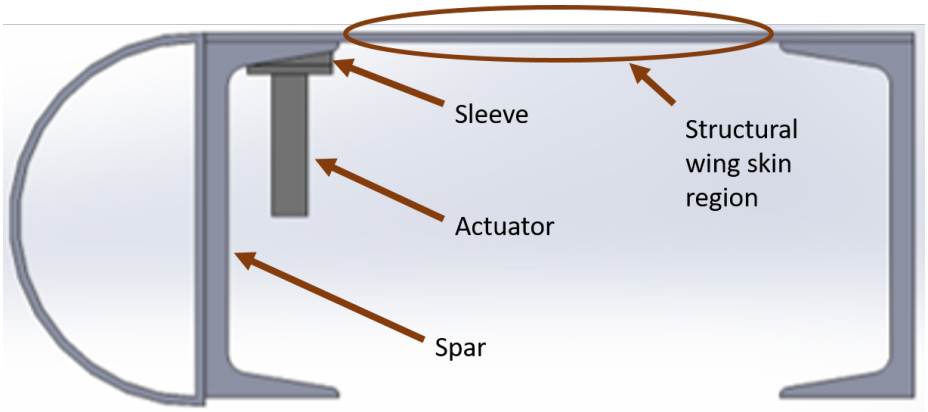

Figure 3.2: Internal design with the actuator attached to the spar

Another alternative design attachs the support to the flap spar through the use of a support beam, as seen in Figure 3.3. The support beam can be made as one part with the actuator, or as two separate parts. The benefit of this design is that the air supply lines can be maintained by removing the non-structural region of the bullnose rather than requiring access inside of the flap box. However, there is a downside to the design in that the spar will have to be drilled in addition to the flap skin, which could pose a structural issue.

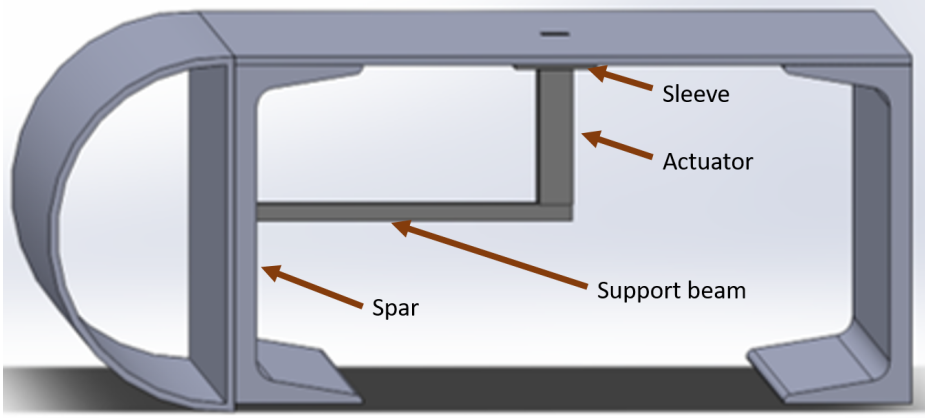

Figure 3.3: Internal design with the support connected to the spar

The benefit of the internal designs is that multiple actuators can be attached together through the use of a plenum. The plenum can be created as separate pieces that connect with the actuators or can be manufactured as one part together with the actuators. The plenum with the individual actuators is shown in Figure 3.4.

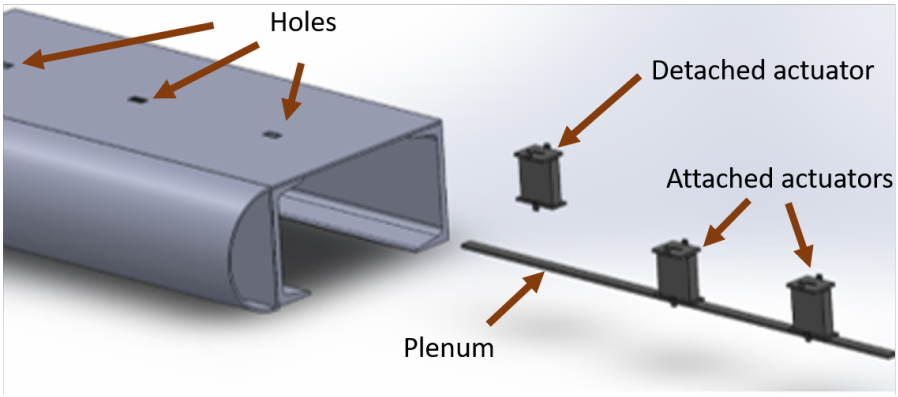

Figure 3.4: Internal actuator array prior to insertion

Actuators are shown with individual attachment first to the plenum, then to the flap skin. Due to the actuators fitting in place through an array, tighter tolerances have to be kept between the alignment of the holes to make sure that the actuators line up in position with the holes. The same principle of inserting an array of actuators can also be applied in another fashion by attaching a guide rail to the bottom of the flap skin as shown in Figure 3.5. A rail attachment rack is fixed to the top of the actuators to be inserted into the

guide rail.

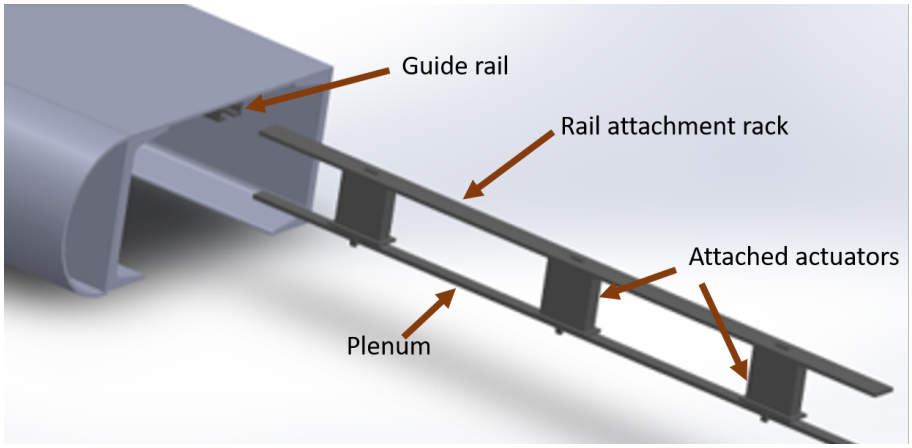

Figure 3.5: Internal actuators connected to a plenum prior to insertion into a guide rail

The plenum with the array of actuators can then be slid into the guide rail and attached as one part into the flap. The end of the insert shown in Figure 3.6 is mechanically fixed to keep the actuators in compression to insure proper sealing. While rivets are shown in this configuration to hold the array in place, any other attachment method could be used. However, a problem with the insertion of this array is that it is dependent on the placement of the flap ribs. More frequently spaced ribs would obstruct the insertion of a plenum through the side of the flap, necessitating a smaller plenum size.

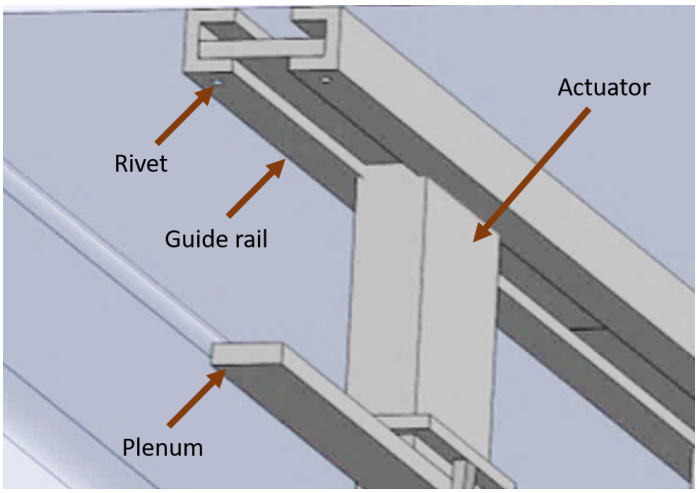

Figure 3.6: Internal actuators fixed into guide rail

3.3.2 External Designs

External designs were simple and did not have much variation. The general layout included a hole into the flap skin followed by a structural sleeve that would be inserted from the outside and permanently attached to the skin. After attaching the sleeve to the skin, the actuator can then be inserted from the outside. Once the actuator is inserted, it is flush with the skin of the flap, without protruding parts. The External design layout is shown in Figure 3.7.

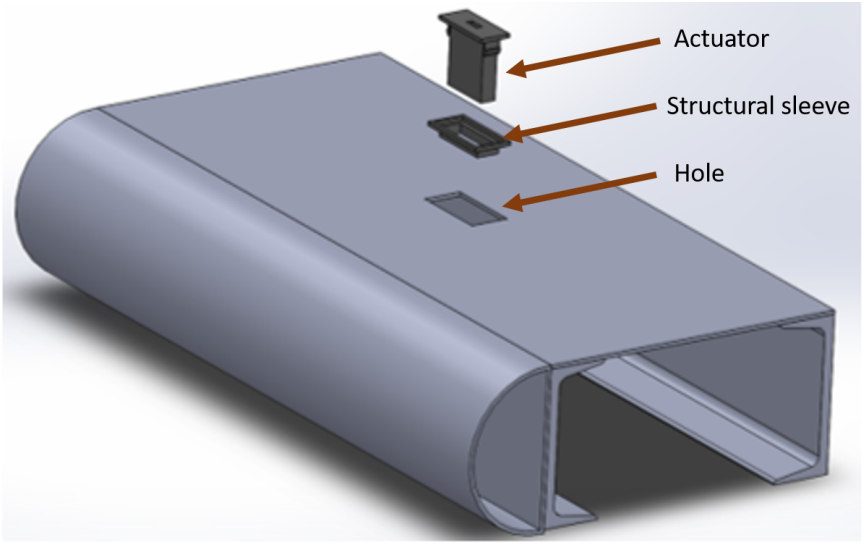

Figure 3.7: External design insertion

The support sleeve can be reinforced through the use of "doublers" underneath the skin. "Doublers" are laminated structural members that are used in the aerospace industry to provide localized structural support to a small region [34]. This reinforcement would prove useful due to the larger hole cut-out required in the structural skin. The actuator would then be inserted and attached to the support sleeve through the use of either snapfits, fasteners, or thermal staking.

Although External Designs are much easier to attach and do not require internal flap access, a major drawback to their design is the large hole size required. Since the actuator would have to be inserted from the outside, the hole in the flap skin would have to be

large enough to accommodate the actuator insertion. This could be problematic as a large discontinuity in the composite flap skin has a tremendous effect on the flap's structural stability. Thus, if an External Design is selected, careful analysis on the hole's effects on the composite skin will have to be conducted. Doublers and other reinforcement methods will also have to be considered.

3.3.3 Internal-External Designs

Internal-External designs combine aspects from both Internal and External designs. Internal-External designs have a hole cut for the actuator to be inserted from the outside, similar to the External designs. A plenum to which the actuators can attach is inserted inside of the flap, similar to the internal designs. The general attachment of the Internal-External designs can be seen in Figure 3.8.

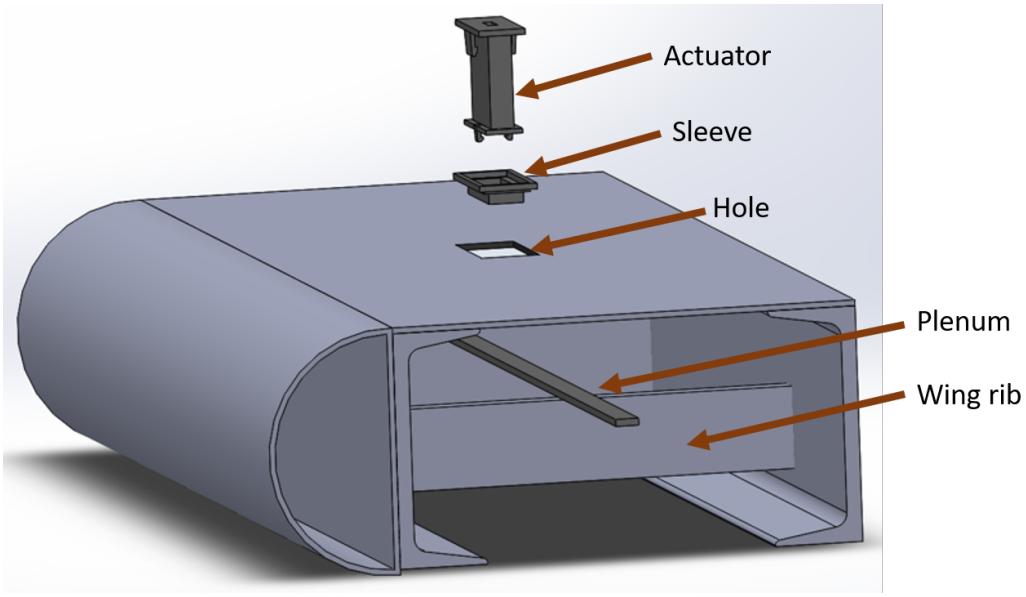

Figure 3.8: Internal-External design insertion

Internal-External designs benefited from having the plenum attachment fixed to the ribs inside of the flap. The actuators would be inserted from the outside, and so, if the actuators needed to be replaced for serviceability, the flap would not have to be taken apart. Additionally, by having the plenum inside of the flap, it is fastened securely, and the

plenum could supply air to the actuators without requiring individual hose connections as in the External design.

3.3.4 Comparison of Designs

Numerous design configurations were created through the morphological charts. Table A.1 in the Appendix lists the designs created based on their attachment methods. Following with the principles of AD, the second axiom is used to select the best design which minimizes the amount of information for each solution. Designs that have the smallest information content constitute better designs; as in the realm of information theory, these designs have lower complexity [32]. In order to measure the information for each solution, a design must contain a solution that meets the required FRs as completely as possible without redundancy. Doing so requires comparing the design range with the system range. In this thesis, the system range was known for each design however there was limited information for the design ranges for each FR for the wing flap. Due to the limited information on the aircraft design ranges, designs were evaluated by comparing their estimated product costs.

The product cost consisted of the material and assembly costs. The material cost was the product of the material cost per weight and the weight of the design. The assembly cost consisted of the product of the labor rate of $18 per hour and assembly time [35]. The product weight was also tabulated for each design to provide another measure of comparison between cost-efficient designs. Calculations and assumptions for the estimated costs are included in Tables A.2-A.7 in the Appendix. The designs with their calculated costs and weights are shown in Table 3.7 and Table 3.8. Rankings are also listed for each design based on the lowest estimated total cost. The total cost and the final rankings are shown in bold.

Table 3.7: Internal design estimated costs and weights

	Internal							
	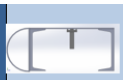							
Design Number	1	2	3	4	5	6	7	8
Product cost	*$2.39*	*$2.44*	*$3.69*	*$4.01*	*$2.45*	*$3.64*	*$3.49*	*$2.33*
Ranking	2	3	7	8	4	6	5	1
Assembly cost	*$5.83*	*$5.83*	*$5.90*	*$5.90*	*$5.83*	*$5.87*	*$5.85*	*$5.83*
Ranking	4	1	8	7	1	6	5	3
Total cost ($)	***$8.22***	***$8.27***	***$9.59***	***$9.91***	***$8.27***	***$9.52***	***$9.34***	***$8.15***
Ranking	**2**	**3**	7	**8**	**4**	**6**	**5**	**1**
Weight (lbm)	*0.046*	*0.048*	*0.042*	*0.056*	*0.040*	*0.044*	*0.047*	*0.058*
Ranking	4	6	2	7	1	3	5	8

Table 3.8: External designs (green) and Internal-External designs (pink) estimated costs and weights

	External				Internal-External	
	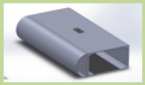	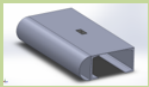	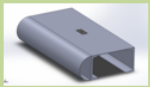	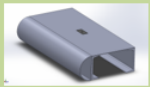		
Design Number	9	10	11	12	14	15
Product cost	*$3.40*	*$3.74*	*$3.62*	*$3.40*	*$3.90*	*$4.05*
Ranking	2	4	3	1	1	2
Assembly cost	*$3.65*	*$3.65*	*$3.65*	*$3.65*	*$5.84*	*$5.94*
Ranking	3	1	2	3	1	2
Total cost ($)	***$7.06***	***$7.39***	***$7.26***	***$7.05***	***$9.74***	***$9.99***
Ranking	**2**	**4**	**3**	**1**	**1**	**2**
Weight (lbm)	*0.089*	*0.975*	*0.994*	*1.000*	*0.080*	*0.080*
Ranking	1	2	3	4	1	1

3.4 Design Selection

In order to compare the designs, cost was considered as the primary goal to rank the different designs. However, a vital question was whether the design rankings would change if certain parameters affecting the product cost were changed. The most notable parameters that affected the product cost were material cost, assembly time, material density, and flap skin thickness. Skin thickness affected the cost as greater thicknesses required more material to fill the hole and support the FO. Although varying the material density does not make physical sense as it is a material property, it was varied to understand how the model would change with respect to this key parameter. A sensitivity analysis was carried out first, followed by a design of experiments to understand interaction effects.

3.4.1 Sensitivity Analysis

A sensitivity analysis was conducted first to determine how the relative rankings of the designs changed relative to a change in a key parameter in the cost equations. Each of these parameters was varied by a high factor (2) and low factor ($\frac{1}{2}$) to view the spread of the data. The results from the sensitivity analysis are shown in Figure 3.9. The cost is shown for each design based on its design numbers shown in Table 3.7 and Table 3.8. The center dots represent the original design's predicted cost, before varying the parameter. Error bars are attached to each design to show the variation in cost when the parameter was varied by the high and low factors. The designs are color coded with Internal designs in blue, External in orange, and Internal-External in gray.

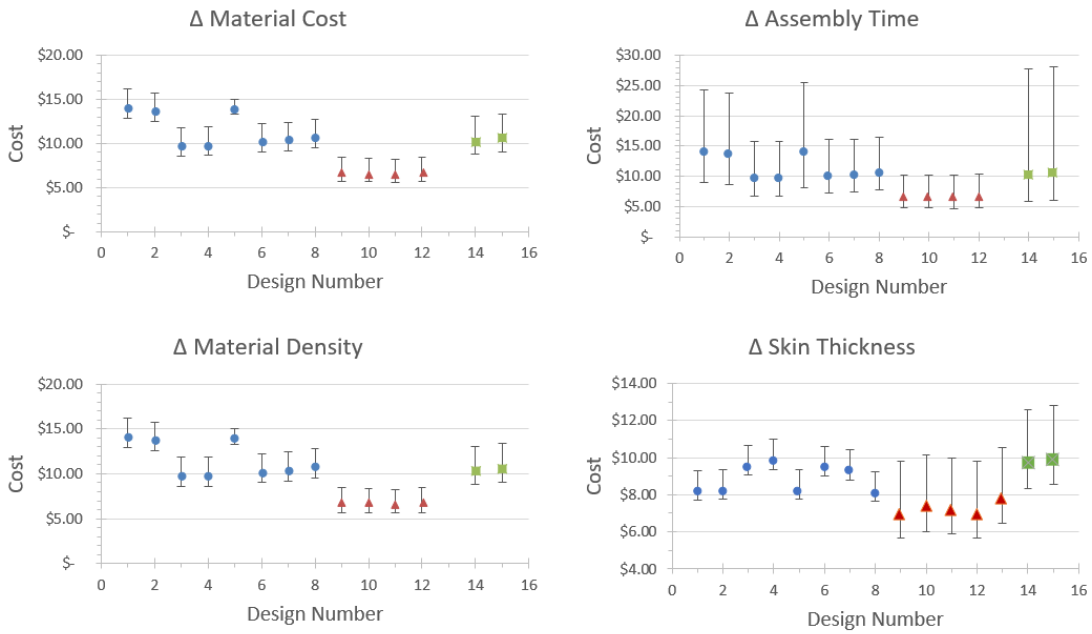

Figure 3.9: Sensitivity analysis on different parameters affecting total estimated cost

When each factor was varied, assembly time showed the largest change in cost, followed by material cost and material density. Increases in the flap skin thickness showed a large effect on the external designs compared to the internal ones, as the FO support would have to be attached to the flap skin and not the internal ribs and flap structures. Mate-

rial Cost and Material Density showed identical variations. This is understandable as the cost equation consisted of the material cost per unit weight multiplied by the density and volume of the material. Therefore, an increase in either parameter by the same multiple yielded equivalent results.

In all of the parameter variations, however, the rankings did not significantly change between individual designs; the low-cost designs remained the low-cost designs while the higher cost designs were still more costly. This showed that design rankings were not affected by changes in the cost parameters.

3.4.2 Design of Experiments

In order to better understand the effects of the parameters on estimated cost, a design of experiments (DOE) was performed to attain a more quantifiable measure of the sensitivity of the parameters and their interaction effects. With four parameters and two factors for each parameter (High-factor=2, Low-factor= $\frac{1}{2}$), a full-factorial design was conducted with 16 different runs. Data were collected for all of the different designs at each factor level for a total of 16*15=240 sets of data. The same four parameters were considered: Material Cost (A), Material Density (B), Assembly Time (C), and flap Skin Thickness (D). Table 3.9 shows the full-factorial breakdown by treatment for each run; -1 represents the low treatment, while +1 represents the high treatment.

Table 3.9: Full-factorial treatment levels

Run #	Treatment	A	B	C	D
1	Null	-1	-1	-1	-1
2	a	+1	-1	-1	-1
3	b	-1	+1	-1	-1
4	ab	+1	+1	-1	-1
5	c	-1	-1	+1	-1
6	ac	+1	-1	+1	-1
7	bc	-1	+1	+1	-1
8	abc	+1	+1	+1	-1
9	d	-1	-1	-1	+1
10	ad	+1	-1	-1	+1
11	bd	-1	+1	-1	+1
12	abd	+1	+1	-1	+1
13	cd	-1	-1	+1	+1
14	acd	+1	-1	+1	+1
15	bcd	-1	+1	+1	+1
16	abcd	+1	+1	+1	+1

The data were analyzed through SAS Institute's JMP software as a full-factorial DOE. From the results of the experiment, all four parameters were found to be significant, along with the interaction between three parameters: Material Cost-Material Density, Material Cost-Skin Thickness, and Material Density-Skin Thickness. This is demonstrated by the low P-values for each parameter as shown in Table 3.10. The vertical blue line indicates parameter significance at the 0.05 level; parameter bars extending to the right beyond the blue line are significant.

Table 3.10: Design of Experiments Effects Summary

Source	LogWorth	PValue
Assembly Time	9.041	0.00000
Material Cost	5.324	0.00000
Material Density	5.324	0.00000
Skin Thickness	4.633	0.00002
Material Cost*Material Density	3.720	0.00019
Material Cost*Skin Thickness	2.825	0.00150
Material Density*Skin Thickness	2.825	0.00150

The DOE effect summary also yielded a cost prediction model shown by Equation 3.1 and plotted in Figure 3.10. This was generated to estimate the cost based on input parameter values. The correlation between the data with respect to cost was high with an R^2 value of 0.9942. The high correlation meant that the cost prediction model fits the data very well as the difference between the model data and the predicted data was minute. Since the R^2 value increases with the addition of parameters to the model, the adjusted R^2 is used to get a better understanding of correlation as it adjusts for the number of parameters in the model. Even with the adjusted R^2, the correlation was still high with a value of 0.9896.

$$\begin{aligned} Cost = &+ 10.82 - 1.46(Cost) - 1.46(Density) - 4.37(AssemblyTime) \\ &- 1.18(SkinThick) + 0.87(Cost * Density) + 0.64(Cost * SkinThick) \\ &+ 0.64(Density * SkinThick) \end{aligned} \tag{3.1}$$

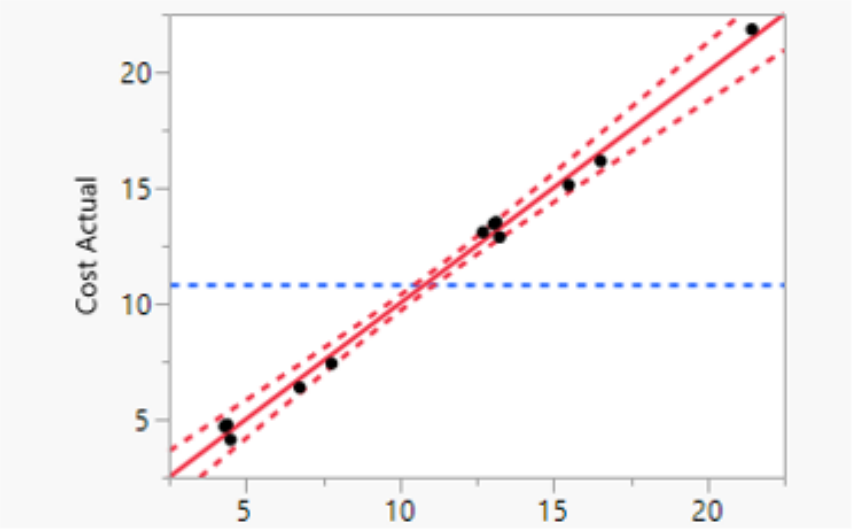

Figure 3.10: Design of Experiments Prediction Plot

Leverage plots were studied to understand how strongly a certain parameter affected the predicted cost. This is shown by the slope of the line in the plot. A zero slope line indicates no interaction between the parameter to the result, whereas large slopes indicate greater interaction effects. Material Cost, Material Weight, Skin Thickness, and their subsequent three interactions all affected the cost, but only slightly. This is shown by Figure 3.11, which shows the leverage plot for Material Cost versus the predicted cost. Assembly time, however, showed a much larger slope which indicates a large effect on the predicted cost, as seen in Figure 3.12. This corroborated the results of the previous sensitivity analysis, which showed that assembly time had a large effect.

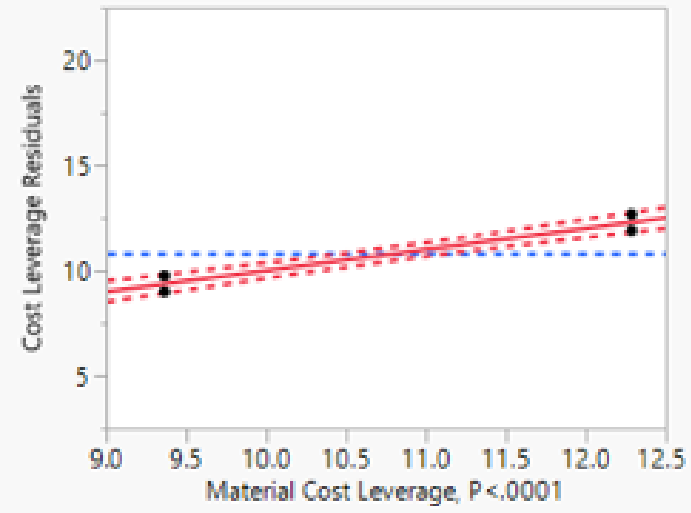

Figure 3.11: DOE Material Cost Leverage Plot

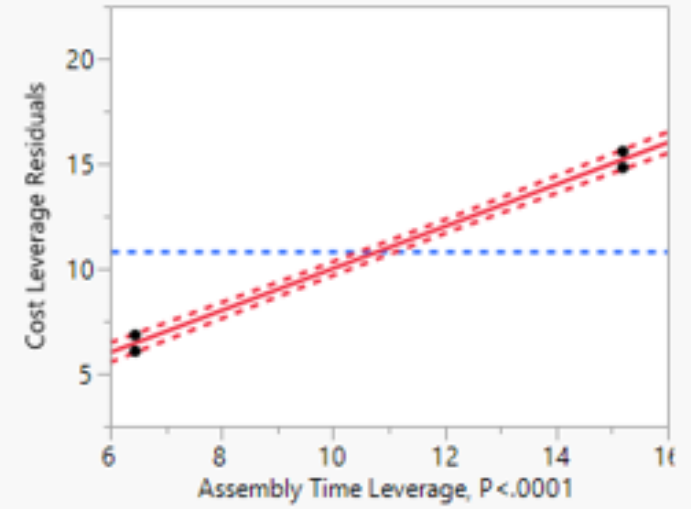

Figure 3.12: DOE Assembly Time Leverage Plot

Multicollinearity poses an issue when multiple parameters are correlated and provide redundant information for the response results [36]. Multicollinearity can lead to inaccurate regression coefficients and misleading results, and so needs to be identified. The variation inflation factors (VIF) for each predictor can be calculated by Equation 3.2 to identify if there is multicollinearity.

$$VIF = \frac{1}{(1 - R^2)} \tag{3.2}$$

If the VIF for a parameter is found to be greater than 10, then there is an issue with multicollinearity. The VIF was calculated for each factor and is shown in the last column of Table 3.11. No multicollinearity was found as the VIF was less than 10 for each of the tested parameters. For all the parameters, the VIF was equivalent to 1, as the R^2 value for each parameter was fairly small.

Table 3.11: DOE Parameter Estimates and Variation Inflation Factors (VIF)

Term	Estimate	Std Error	t Ratio	Prob>|t|	VIF
Intercept	10.825	0.135236	80.05	<.0001*	.
Material Cost[-1]	-1.46125	0.135236	-10.81	<.0001*	1
Material Density[-1]	-1.46125	0.135236	-10.81	<.0001*	1
Assembly Time[-1]	-4.37375	0.135236	-32.34	<.0001*	1
Skin Thickness[-1]	-1.18	0.135236	-8.73	<.0001*	1
Material Cost[-1]*Material Density[-1]	0.8775	0.135236	6.49	0.0002*	1
Material Cost[-1]*Skin Thickness[-1]	0.63875	0.135236	4.72	0.0015*	1
Material Density[-1]*Skin Thickness[-1]	0.63875	0.135236	4.72	0.0015*	1

In analyzing the data, interaction plots were studied to better understand how the parameters interacted. Interaction plots allow for visual understanding of how a change in one parameter affects another parameter. Figure 3.13 shows the interaction plots for the four parameters. Each box in the interaction plot compares two parameters against each other at both the high (1) and low (-1) factors. For example, the box in row 2 column 1 shows how the predicted cost changes with respect to the Material Cost. The blue line shows how the predicted cost versus Material Cost changes when the material density is high (1), while the red line shows the relationship when the Material Density is low (-1). From this box, it can be seen that Material Cost more strongly affects the predicted cost when the Material Density is high compared to a low level. This indicates an interaction effect between the two parameters of Material Cost and Material Density.

Parallel lines in the interaction profile box indicates no interaction between two parameters, as the slopes remain unchanged regardless of whether a certain parameter is at a high or low level. Assembly Time did not show significant interaction with the other parameters,

and this is clearly shown by the parallel lines with each of the different parameters. These parallel lines are seen in the boxes in row 3, and the boxes in column 3 which show the interaction of the Assembly Time with other parameters.

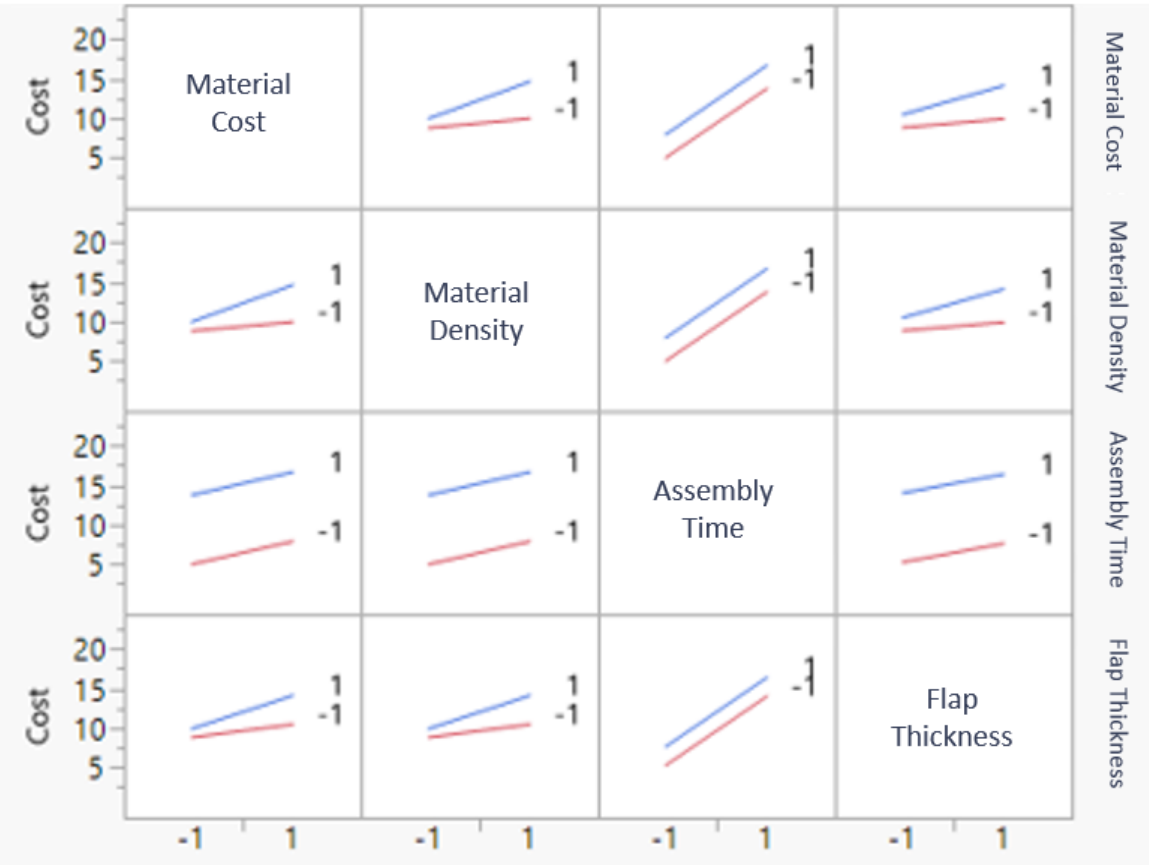

Figure 3.13: Design of Experiments Interaction Plots

3.5 Chapter Summary

In this chapter, customer attributes were collected to generate the design FRs and DPs. These were used to create uncoupled design solutions. Designs costs were estimated, and the designs were ranked based on their overall cost. A sensitivity analysis and design of experiments were used to evaluate how the design rankings would change based on changes in the cost parameters. It was found that, although costs changed when parameters were varied, the overall ranking of the designs remained unchanged. Thus, the higher ranked

designs were still the higher ranked designs, despite changes in their costs. The next chapter focuses on the detailed designs for top designs from each category (Internal, External, Internal-External). Following that, the final design is selected and discussed further.

CHAPTER 4
DETAIL DESIGNS

The results from the sensitivity plots and the DOE showed that, despite changes to the main cost parameters, the overall rankings between designs did not vary. This signified that the top ranked designs remained at the top level despite changes in performance parameters; likewise, bottom ranked designs remained at the bottom of the list. Knowing this information, the top design, that with the lowest cost, from each category was selected. These designs were refined by taking into account factors such as accurate actuator dimensions, nozzle-to-skin integration, FO angle of attack, aircraft approved sealant, and snapfit designs factoring in the required attachment force. Lastly, a final design was created with both a CAD model and a physical mockup.

4.1 Internal

The Internal design consisted of FO arrangements that require access to the inside area of the flap box for both attachment and detachment of the device. These designs benefited from small holes required in the flap skin surface but necessitated access to the flap's internal region. Access to the flap's internal region is manageable during initial flap fabrication; however, access is limited once the flap has been fully assembled and an FO needs to replaced.

The Internal design of the FO can be seen in Figure 4.1. The design consists of two main parts: the actuator and the sleeve. A hole is cut out from the top surface of the skin, and the top surface of the sleeve fits into this hole. The sleeve is affixed to the bottom surface of the skin with an adhesive. The actuator is then attached to the sleeve through the use of a pair of snapfits that attach to grooves in the sleeve.

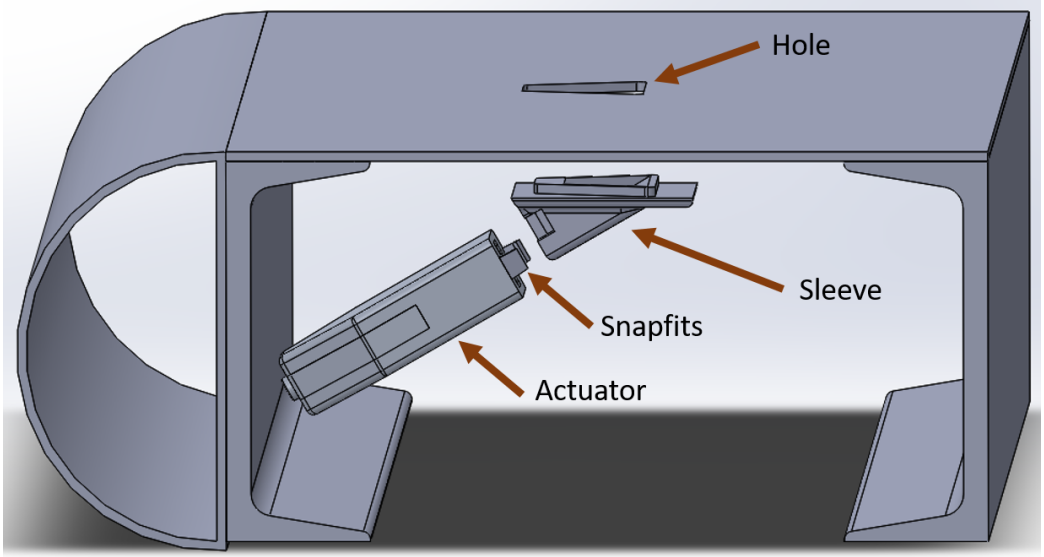

Figure 4.1: Internal design detached

Additionally, a doubler, or structural reinforcement, can be attached around the sleeve if further reinforcement is needed due to the hole [34]. The attached FO arrangement is shown in Figure 4.2 with the doubler fixed between the sleeve and the bottom skin surface. In the Internal design, the angle of the FO exit nozzle is 30° to reduce pressure losses in the actuator while effectively blowing air parallel to the flap surface [6].

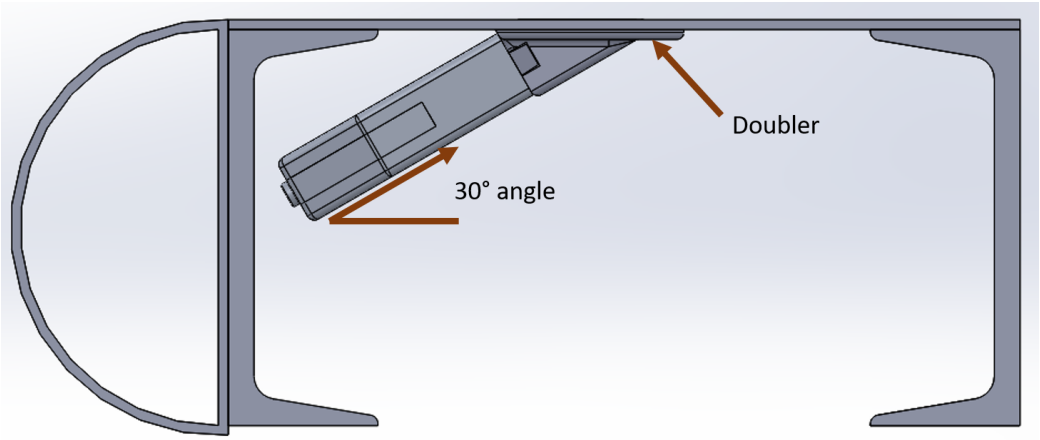

Figure 4.2: Internal Design, with the doubler attached

The actuator design, shown in Figure 4.3, consists of many changes compared to the simplified model used in the concept generation phase. The part now includes accurate

dimensions of the actuator for a full-scale wing flap [6]. The actuator is closed off by adding a cover to the top of the FO design, which is shown as a separate part in the figure. Depending on the manufacturing process used to fabricate the actuator cover, it can be produced as a separate part (injection molding) that is later attached or manufactured with the actuator as one part (3D printing). If the cover is manufactured as a separate part, a high temperature polymer adhesive can be used to attach and seal the two parts. Ultrasonic welding may also be used, but due to the high CF content within the PEKK material, a heat treated steel or carbide-faced titanium horn would have to be used [37]. A uniform wall thickness is used in the FO to allow for similar cooling times throughout the part. With regards to load handling, the wall thicknesses were sized to handle the internal stresses on the FO. The figure shown includes a grayed out region to hide proprietary material.

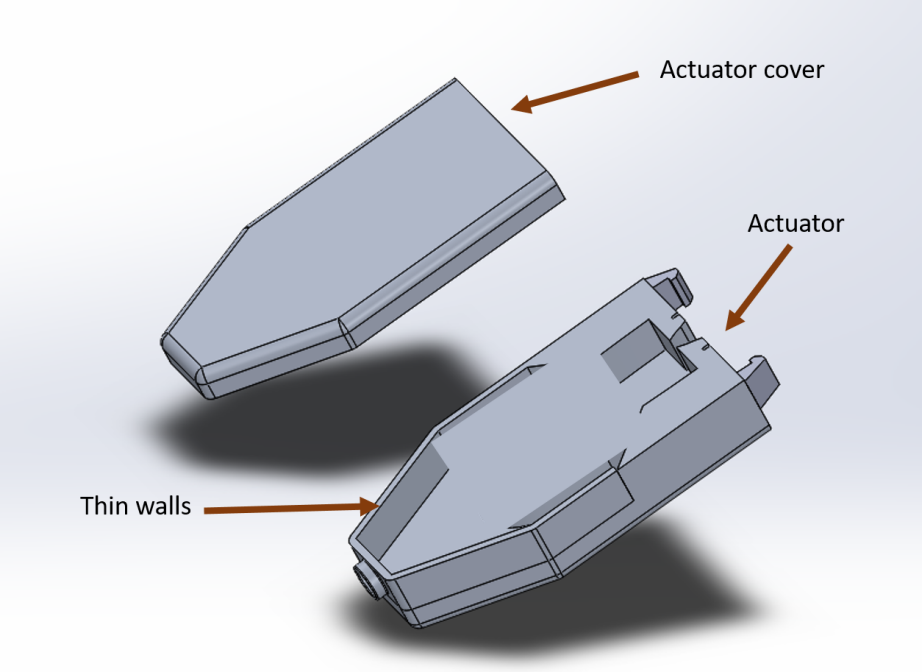

Figure 4.3: Internal Design: Actuator and cover shown as two parts

As shown in Figure 4.4, the actuator has an extended entrance region to allow for incoming flow from the air inlet to flow smoothly before mixing in the internal chamber. A tapered profile is used to guide the air flow into the chamber. Rounded edges along the

outside surface of the part aid in reducing stress concentration regions due to sharp corners. Two snapfits are located at the top of the actuator to attach to the supporting sleeve.

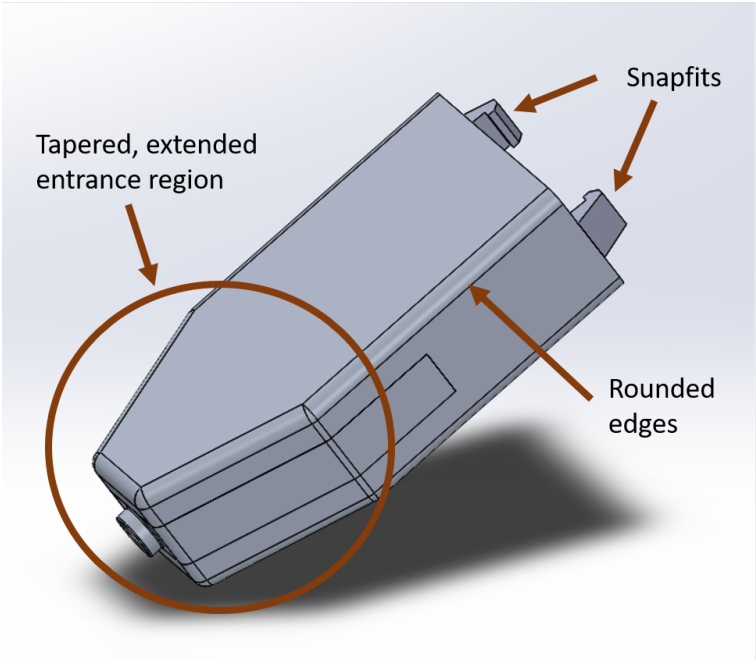

Figure 4.4: Internal Design: Actuator

The top side of the actuator contains the exit nozzle that meets with the sleeve surface, as shown in Figure 4.5. A recessed groove is placed around the nozzle wall to allow for an O-ring to be inserted to provide sealing. Although the groove around the nozzle wall is rectangular, a regular sized O-ring can be used due to the rounding of the edges and corners of the groove. The design selected requires an O-ring that is $\frac{1}{16}$" thick with an $\frac{11}{16}$" outer diameter, that can withstand temperatures between -54°C to 82°C [14].

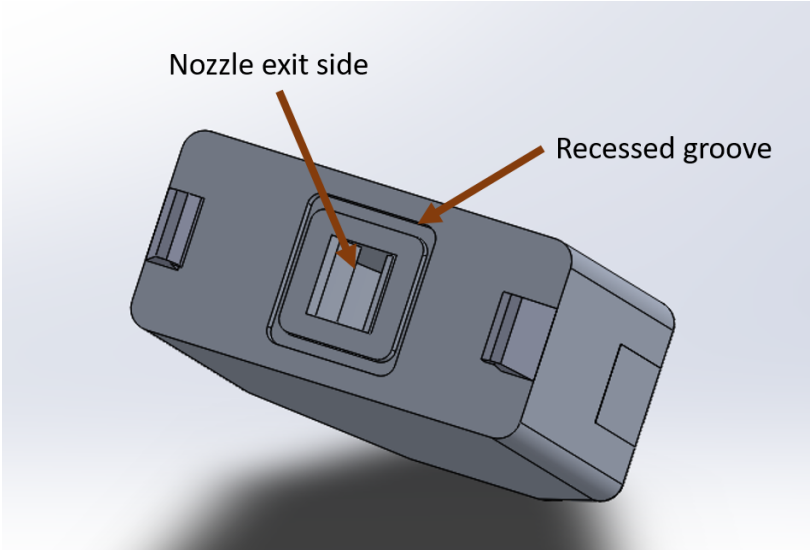

Figure 4.5: Internal Design: Actuator top surface with sealant groove shown

Two snapfits are placed at opposite ends of the actuator top surface. These snapfits are sized to require about 12 lbf to insert and 17 lbf to remove, based on calculations from DSM Snapfit Theory [38]. These force values were used based on a target insertion force of 10 lbf, which is common for insertion of objects by manual labor without requiring the use of a tool [39]. In order to calculate the snapfit assembly force, several parameters were manipulated as shown by Figure 4.6. When calculating the required forces, a coefficient of friction of 0.35 was used for the CF PEKK material [40]. The snapfits are also designed with a 3° draft angle to ease the removal of the snapfit from the sleeve crevice. Additionally, a 60° release angle was used on the exit side of the snapfit hook to allow the actuator to be removed from the sleeve. Conversely, if a 90° angle was selected, it would make the snapfit non-removable (require >43 lbf to remove), which could be used if the FO is desired to be non-removable. However, in doing so, destructive removal of the FO would be necessary in order to replace it.

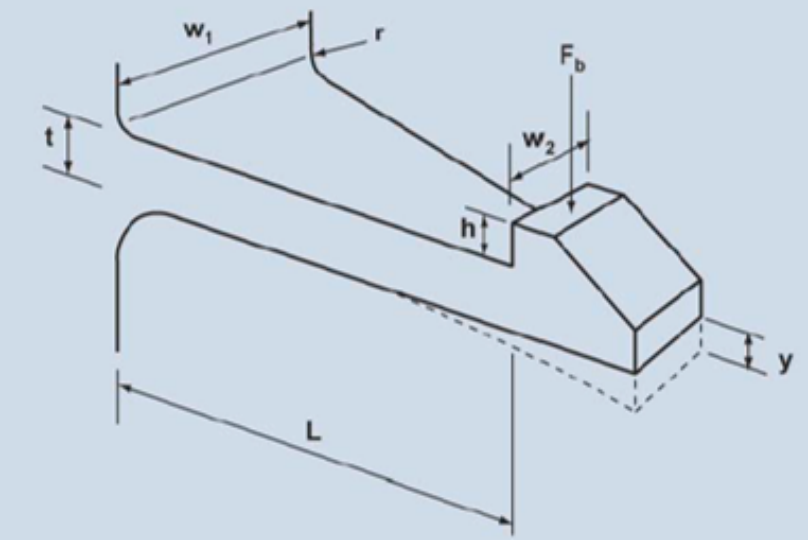

Figure 4.6: Design parameters considered in snapfit design

The other main component of the Internal design is the sleeve attachment, shown in Figure 4.7. This part is a medial connection point between the actuator device and the flap skin surface. After creating the hole in the flap skin, the sleeve is connected to the bottom surface of the skin and allowed to close up the cut inner skin cross section. The sleeve is designed to have the nozzle profile extension with the same angle as that in the actuator to eject air from the FO and into the free-stream air. The nozzle profile is integrated into the sleeve design to limit the part count, which subsequently leads to a lower part cost [39]. The sleeve contains a large lip area that extends 0.5" from the exit nozzle to allow for more contact surface area between the sleeve and the bottom skin surface. This large surface area is necessary to provide an adequate bonding area to keep the sleeve in place and prevent it from peeling from the flap skin. The top surface of the sleeve has a raised wall area that encloses the side walls of the flap skin to prevent actuator exhaust air from blowing into the exposed flap skin. This is important for flap skins with honeycomb structure, as there would be more gaps for the exhaust air to spill into.

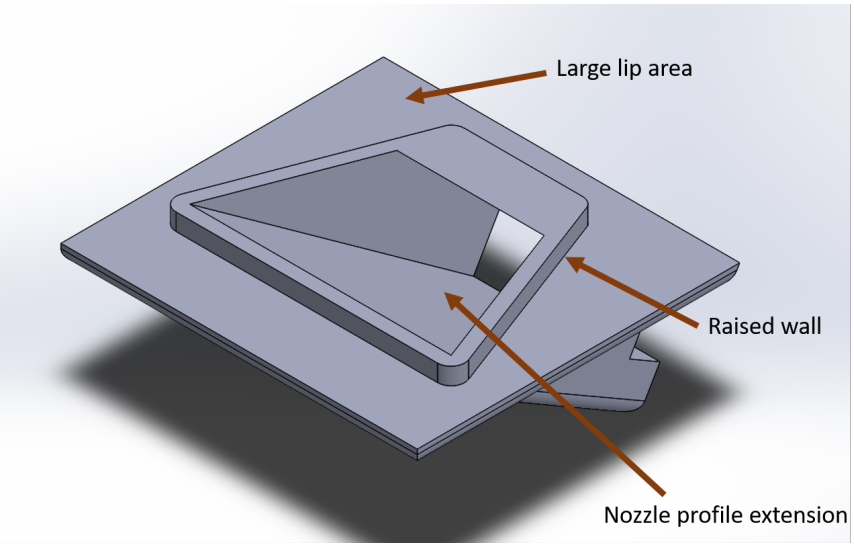

Figure 4.7: Internal Design: Sleeve isometric view

The actuator attaches to the bottom surface of the sleeve with snapfits that fit into side pockets in the sleeve, as shown in Figure 4.8. The snapfits hold the device in place and ensure proper compression so as to prevent air leakage from the FO. Rounded edges along the outside surface of the part aid in reducing stress concentration regions due to sharp corners.

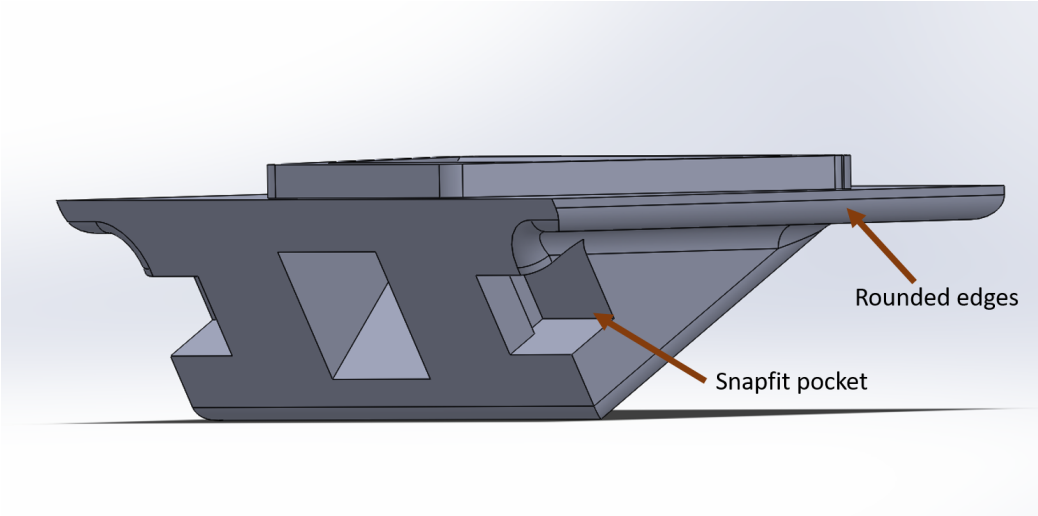

Figure 4.8: Internal Design: Sleeve back view

The flap-skin hole for the sleeve requires the use of a precise mill or waterjet cutter to create the hole shape. Since the nozzle protrudes in a trapezoidal shape, the hole shape

would also be a trapezoid. Previous simulations on hole size effects on the flap skin showed that a trapezoidal shape would reduce the amount of cut material while limiting induced stress [28]. Figure 4.9 highlights the overall shape of the flap cutout area with arrows indicating the area of the nozzle versus the area of the skin hole cutout. Rounded corners are also used to reduce the stress concentrations in both the nozzle and the flap skin hole. The wall thickness of the nozzle is modeled to be similar to the part wall thickness. The approximate dimensions of the hole cutout are 1.8” x 1.0” while the area required by the nozzle end is approximately 1.6” x 0.7”.

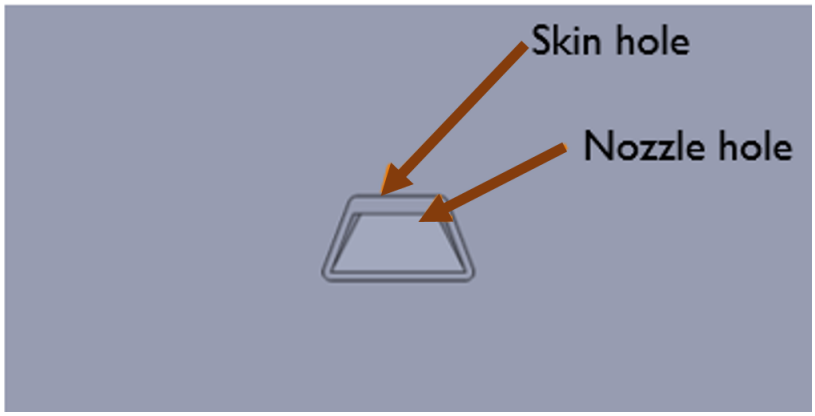

Figure 4.9: Internal Design flap cutout region

4.2 Internal-External

Previous designs of the Internal-External category included attachment to the flap support structure such as the ribs or stringers. However, further analysis of the current internal geometry of a composite flap revealed that the flap box did not contain local ribs or stringers. This lead to a reconsideration of how the FO could be attached internally while allowing external access later on. Internal access would be feasible while the flap is still being assembled and access to the internal region and flap bottom surface is available. External access would be anytime after the flap has been assembled and access to the internal flap box is not readily available.

In order to refine the Internal-External designs, the preliminary External design shown

in Figure 4.10 was used as a base point. This design was modified to permanently mount the sleeve to the flap's bottom surface when access to the internal region is available. The actuator would then be inserted through a hole in the flap surface and attach to the internal sleeve. Subsequent removal of the actuator for maintenance or replacement would be achievable through the removal of the actuator in the same manner to that it was inserted.

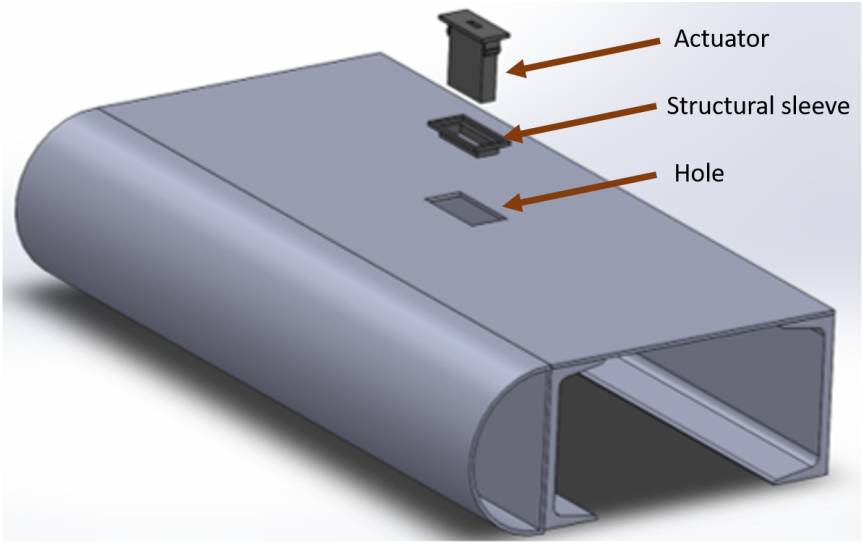

Figure 4.10: Preliminary design showing external attachment

The preliminary design was adjusted for the nozzle extension and the angle of attack of the actuator with respect to the flap skin. In doing so, however, a sizeable hole was required to be cut in the flap skin due to the large projected area of the FO when inserted vertically. This can be seen by the boxed region encapsulating the region that would need to be cut in Figure 4.11.

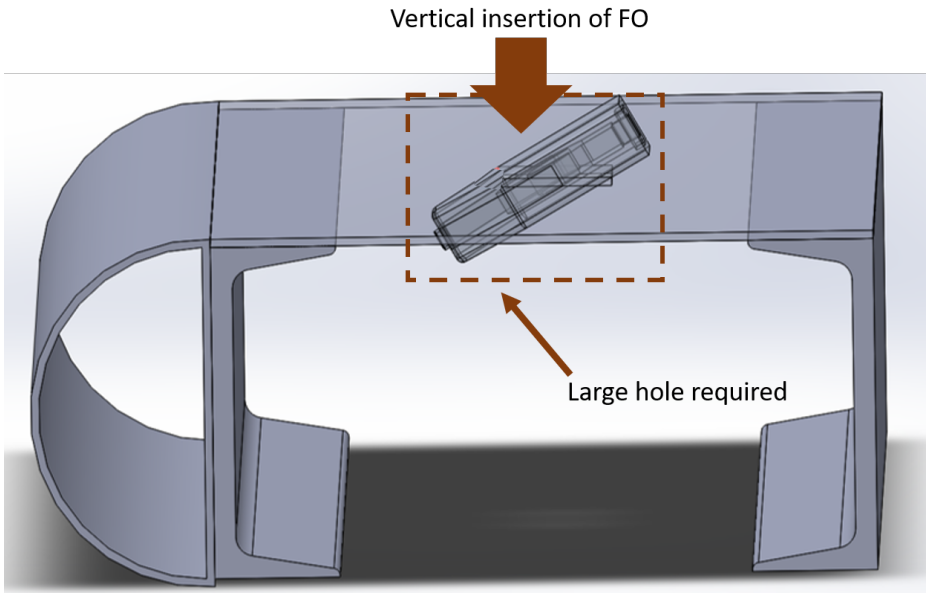

Figure 4.11: Preliminary design showing large projected area needed in flap

The FO design was updated to accommodate the large hole required. This involved adjusting the actuator design to allow for a reduced projected part area. The preliminary design is shown in Figure 4.12a while Figure 4.12b shows the updated design. The nozzle extension profile was created to allow the air to exit from the actuator and into the freestream velocity at the flap surface. The nozzle is offset at an angle with respect to the actuator to allow for insertion from a vertical position. This contrasted with the flat lip that was used in the preliminary actuator design.

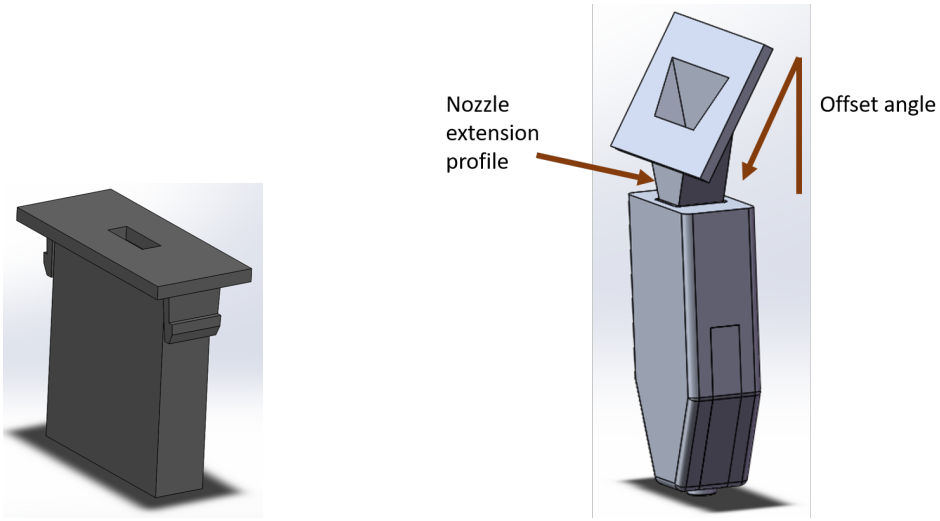

(a) Preliminary design (b) Updated design

Figure 4.12: Comparison of previous vs updated external actuator design

Similar to the Internal design, a support sleeve is to be connected to the bottom surface of the flap skin to allow the actuator to attach to it. The sleeve design is shown in Figure 4.13. This design is modeled in a rectangular shape similar in dimension to the hole size required in the skin. The sleeve also contains an extended lip to create a large contact area to bond with to the bottom skin surface. An extension area for the actuator is also created for the actuator lip to rest on. This area is smaller in perimeter than the lip, and thus the lip can be placed on top of the sleeve without allowing the actuator to fall through it.

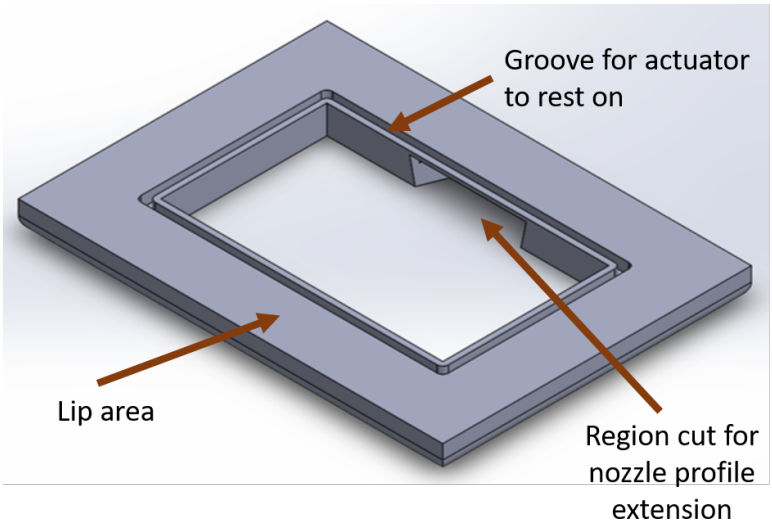

Figure 4.13: Final design of the Internal-External sleeve

The final design of the actuator with the connected nozzle profile extension is shown in Figure 4.14. This design shows the nozzle profile extension and the lip area connected to the actuator as one individual part. A $\frac{3}{8}$" air inlet allows for air to pass into the device, while a tapered bottom edge and rounded edges help facilitate the air flow within the device. Two snapfits are located on either side of the nozzle exit area to allow attachment to the support sleeve. At the top surface of the actuator lip are slight indentations to allow for locating the snapfit center points once the device is in place. This could aid in the removal process of the actuator as drilling of the snapfits would be required to unlatch the FO from its attached sleeve. The snapfit center points could also be visually represented through the use of shallow laser engraving or localized surface roughness instead of indentations.

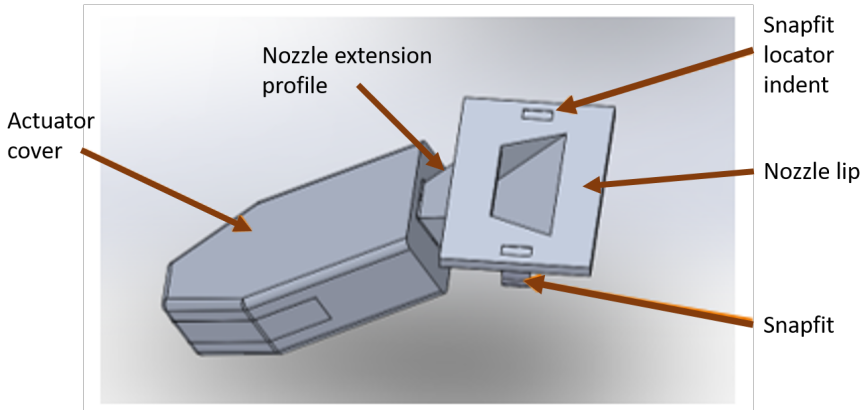

Figure 4.14: Final design of the Internal-External actuator

The vertical insertion of the actuator and its subsequent steps to its final position are shown by the storyboard in Figure 4.15. The first position shows the sleeve and the actuator prior to attachment. The second step involves attaching the sleeve to the skin. After that, the actuator is inserted vertically into the hole in the sleeve. Due to the smaller hole area of the sleeve, the actuator can slip through the hole but the lip keeps it from falling in and creating foreign object debris (FOD). The actuator is then rotated until the lip lines up flat with the sleeve, maintaining the FO into its proper position at the correct angle of attack. Two snapfits mounted on the bottom of the actuator lip lock into place, connecting with the bottom side of the sleeve. Although this design incorporates snapfits, rivets or thermal staking pins may be used to attach the actuator to the sleeve. In all cases, the actuator is attached to the sleeve and not to the skin so as to not create a local stress concentration.

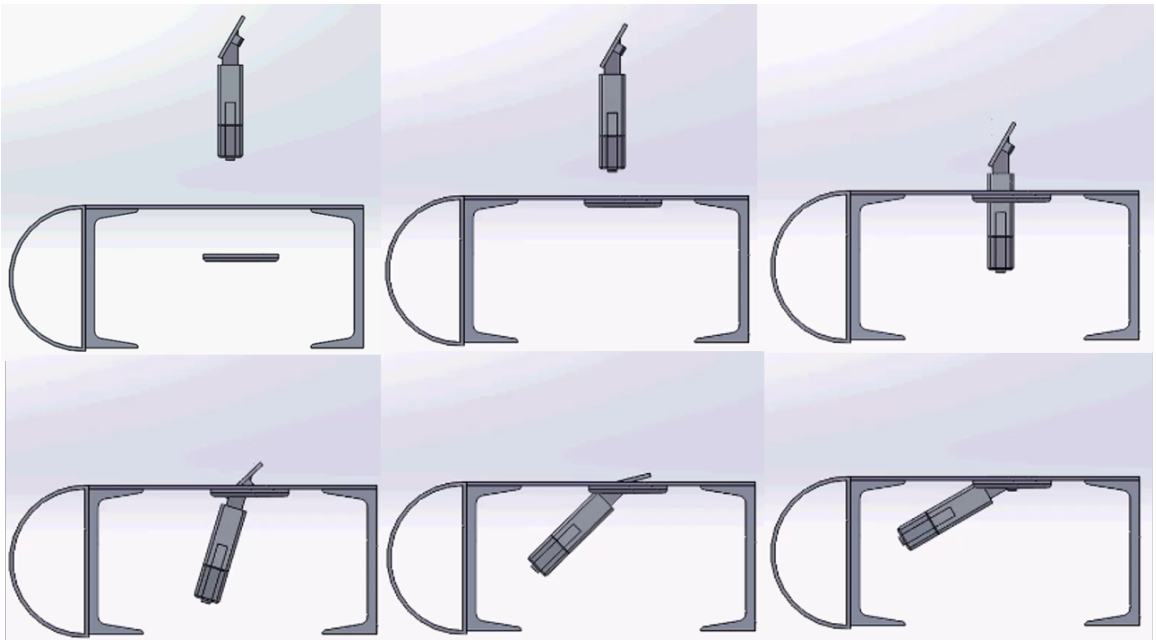

Figure 4.15: Compilation showing the insertion of the Internal-External design

The hole cutout in the skin would need to be a rectangular shape, which can be done through the use of an orbital mill. The hole size would be approximately 2.7” x 1.7” as shown in Figure 4.16 to accommodate the size of the actuator’s lip. The lip itself contains the extension of the nozzle profile which has an outlet hole of approximately 1.7” x 0.7”. Although the nozzle outlet is not much larger than the hole required for the Internal design, the surrounding hole in the skin would need to be larger to hold the actuator securely. Compared to the Internal design, the hole size required for the Internal-External design is approximately 155% larger in area.

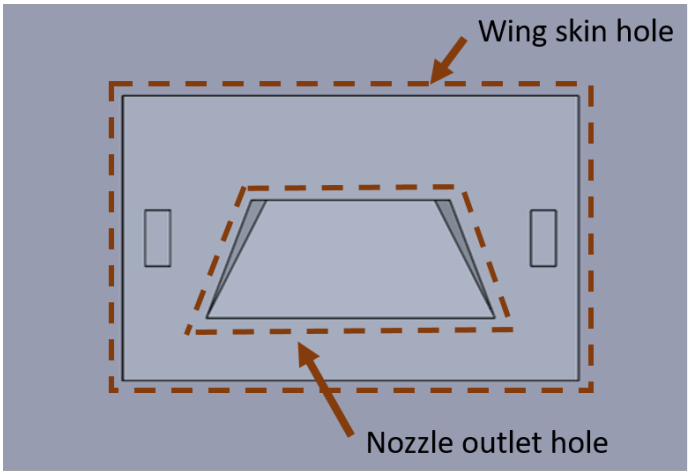

Figure 4.16: Top view of the nozzle profile outlet within the flap skin

4.3 External

The External design consists of an attachment method that would allow insertion of the FO into areas that could not be accessed internally. This would be useful for the retrofit attachment of FOs into older planes. Cuts would be made into the flap skin and then the support sleeve and the actuator could be installed solely from the external flap side. Replacement of the actuator would also be from the outside, as the actuator can be removed in the reverse direction of insertion.

The refined designs of the External FO mounting share many similarities to the refined Internal-External designs. The same actuator with built-in nozzle profile extension is used and a similar sleeve is designed. The assembled setup of the External design is shown by Figure 4.17.

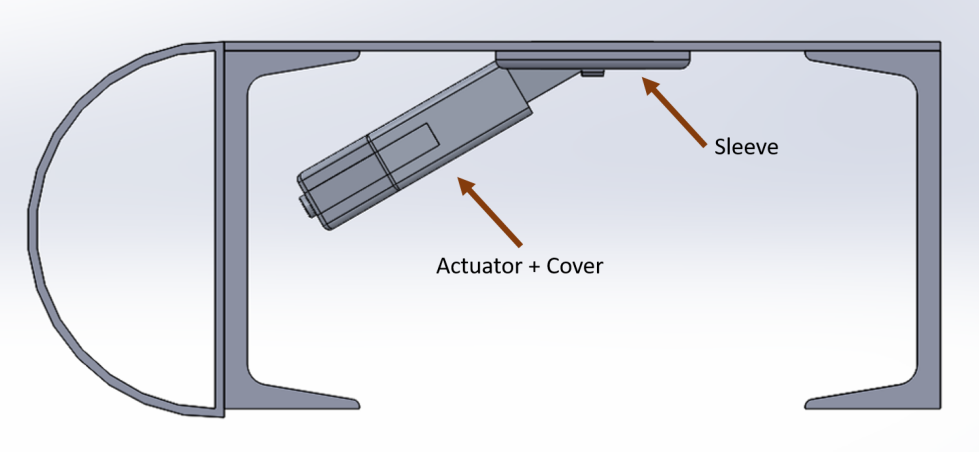

Figure 4.17: Assembled view of the External design

The main difference between the External design and the Internal-External design is the design of the sleeve that holds the actuator in place. In order to fit the FO without access to the internal flap box, the sleeve would have to be placed from outside of the flap. This involved creating the sleeve so that it could fit into the hole in the skin from the outside, and then be fixed into place by bonding it to the bottom skin surface. Two designs were created to satisfy these criteria.

The first design, shown by Figure 4.18, incorporates one central sprue that can be used to hold the sleeve and position it into the correct location inside the flap box. The method of insertion would be to insert the sleeve through the shorter side at an angle, and then rotating the sleeve while sliding it further into the flap box until the top surface is parallel with the bottom flap skin surface. In order to attach the sleeve to the flap skin, an adhesive would need to be applied prior to insertion, or rivets can be used to attach the sleeve to the flap skin to allow for removal later. In both methods of attachment, the operator would pull on the central sprue to maintain compression and ensure a tight fit between the sleeve and the bottom skin surface. After the sleeve is in place, the sprue may then be removed by cutting off the edges connecting it to the part. In terms of manufacturing the sprue, injection molding can be used and the central sprue that is used to fill the mold may be kept in place until after the part is assembled.

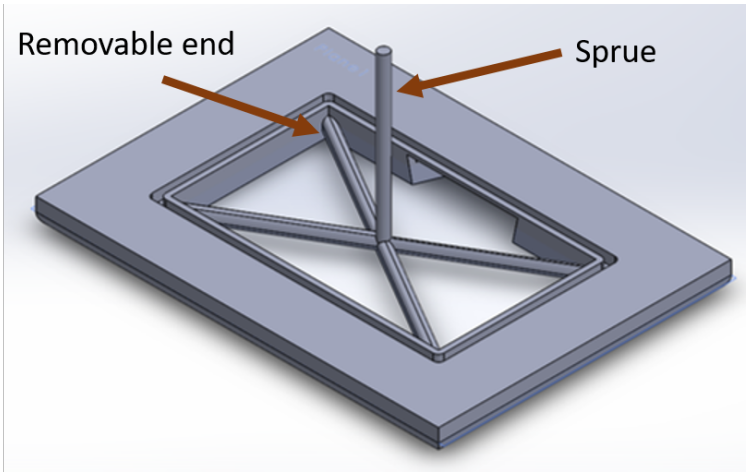

Figure 4.18: Sleeve design with one part

The second design, shown by Figure 4.19, sections the sleeve into four parts with individual sprues. Since the sleeve is separated into many parts, insertion of the parts would be easier than a design with one sprue, as no rotation or sliding of the parts into place would be necessary. Each part would be lowered vertically into the flap box through the cutout in the surface, and then positioned into the correct location and attached. Attachment could once again be done through either an adhesive or fasteners. Similar to the first design, the sprues would be created during the injection molding of the part and then be used to hold the part and maintain compression during the attachment to the flap. Compared to the previous design, the design with multiple parts allows for easier insertion of the parts as there is no rotational or sliding movement, and facilitates more compression during attachment as each sprue has a lower moment arm compared to the design with the central sprue. The downside to this design is that, because it consists of multiple parts, this increases the overall number of parts required which leads to a higher manufacturing complexity [39]. Additionally, a greater quantity of smaller parts can lead to more parts being lost, or possibly dropped inside of the flap and thus creating FOD.

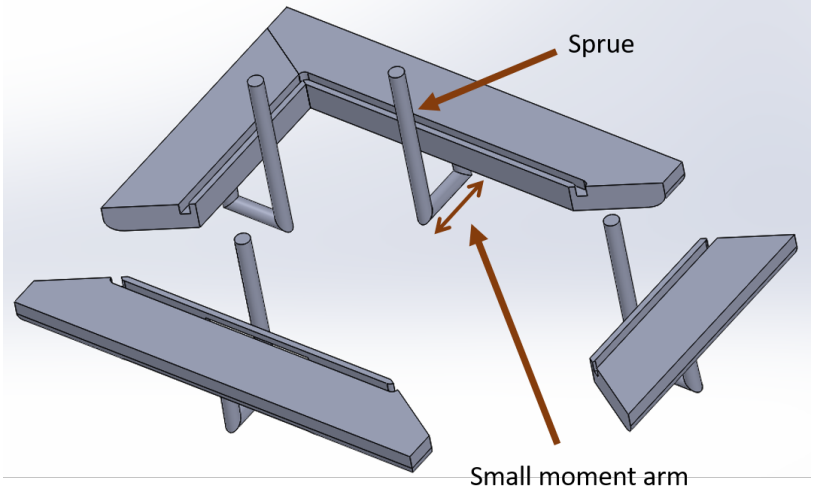

Figure 4.19: Sleeve design with multiple parts

4.4 Final Design

The Internal design was selected as the basis for the final design. A physical model was also created to provide a visual mock-up inside a generic wing flap, with inside spars and wing geometry to properly represent the full-scale flap size. A 787-type aircraft's flap dimensions were used as the flap basis due to the usage of composite skins and reinforcing materials on existing aircraft.

4.4.1 CAD Model

The model of the flap box differed than that used in previous design work as a flap model with more representative dimensions was used. This updated flap shown in Figure 4.20 was scaled to the representative size of a full size wing flap. Spars were spaced out to their relative positions along the chord of the flap, and a span of 6" was used to produce a section model of the entire wing flap. The spar and skin thicknesses were also adjusted to more closely follow that of a real wing flap. The FO design can be seen attached to the flap in Figure 4.21. The design consists of three parts: the actuator, actuator cover, and the sleeve.

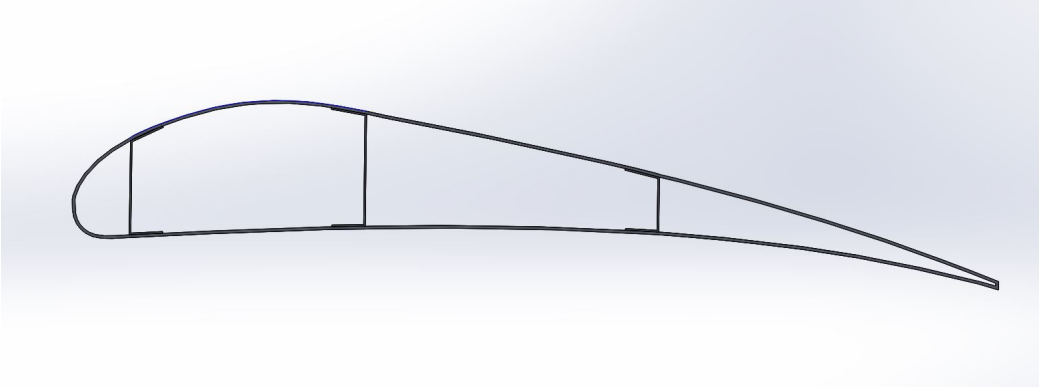

Figure 4.20: Representative model of a wing flap

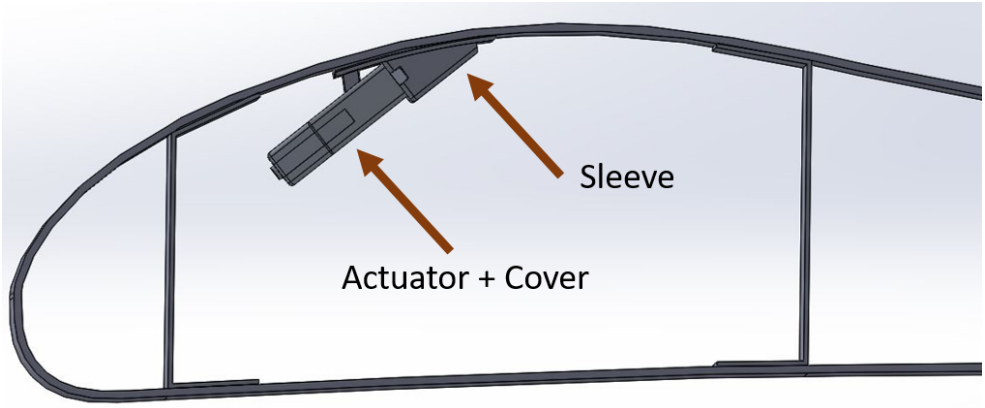

Figure 4.21: Assembled view of flap with the FO

The final design for the actuator is shown in Figure 4.22. Rounded edges are used instead of sharp corners along the outside part surface to reduce stress concentrations and aid in manufacturing. A uniform wall thickness is used in the actuator to allow for uniform cooling throughout the part, which is important for IM. The exit side of the actuator has a recessed groove that allows for an O-ring to be inserted to provide sealing. Two snapfits are mounted to the topside of the part to allow for attachment to the sleeve. A vertical beam protrudes from the top surface of the actuator that slides into a slot in the sleeve. Along with the snapfits, this beam is used to hold the actuator to the sleeve securely.

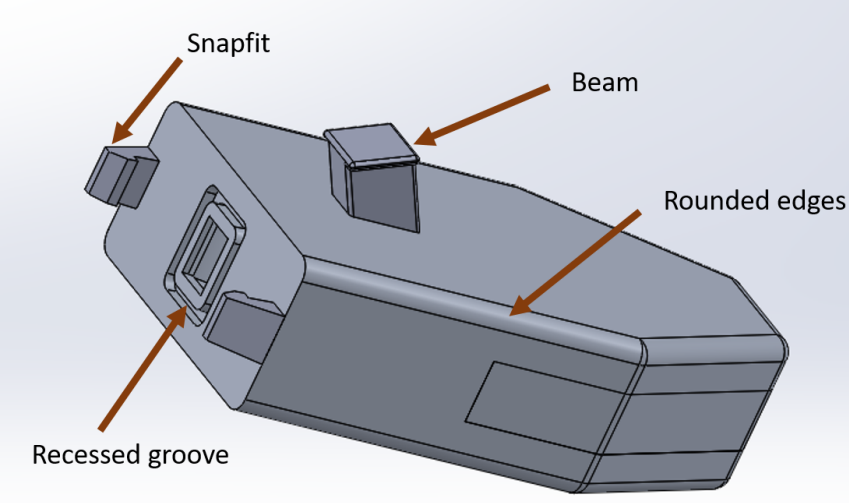

Figure 4.22: FO actuator

The actuator is closed off by adding a cover to the top of the FO design. Depending on the manufacturing process, the actuator cover can be produced as a separate part (IM) that is later attached or manufactured with the actuator as one part (3D printing). The cover and the actuator, shown as two separately manufactured parts, can be seen in Figure 4.23. If the cover is manufactured as a separate part, a high-temperature polymer adhesive can be used to attach and seal the two parts. Ultrasonic welding may also be used, but due to the high CF filler content within the PEKK material, a heat-treated steel or carbide-faced titanium horn would have to be used [37]. To help join the actuator to the cover, a tongue-and-groove joint is used to increase the bonding surface area to more securely hold the two parts. The raised edge for the 'tongue' on the actuator side is shown in Figure 4.24. The figures shown include grayed out regions for proprietary material.

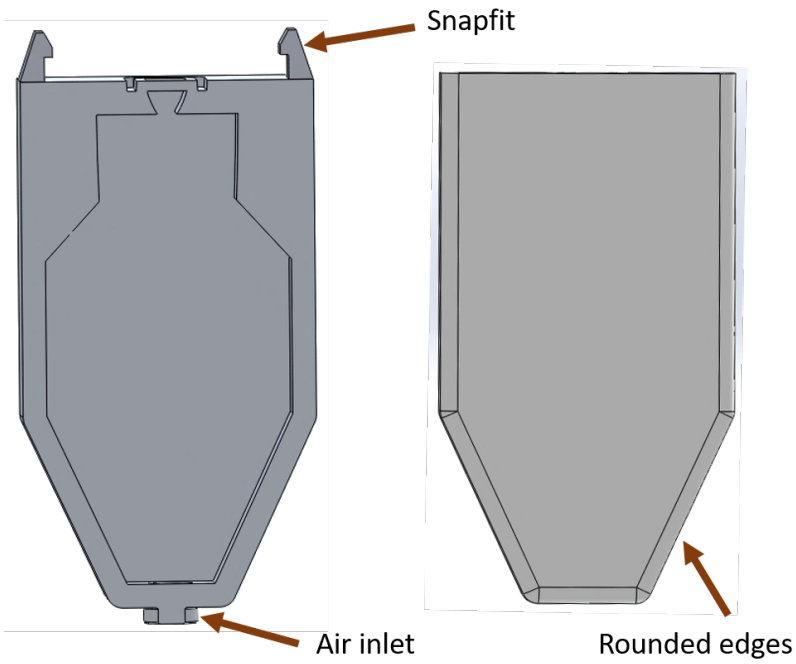

Figure 4.23: Actuator (left) and Cover (right)

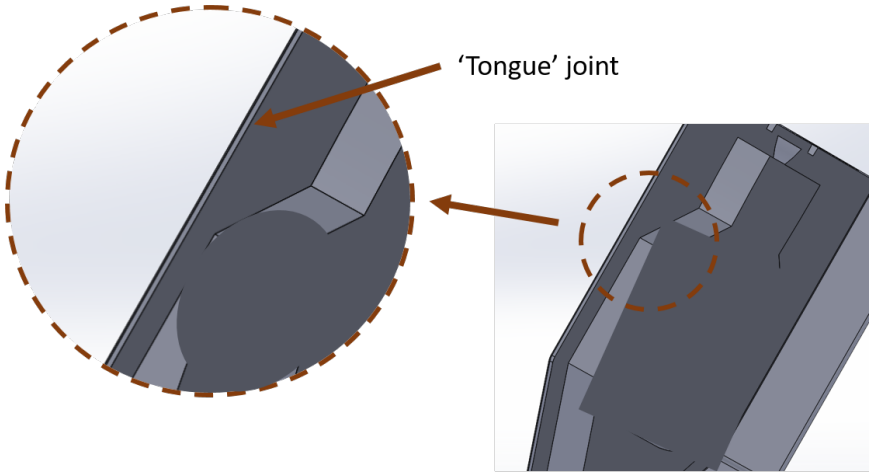

Figure 4.24: Tongue shown on actuator)

The last FO component is the sleeve attachment, shown in Figure 4.25. This part is an intermediate connection point between the actuator and the flap skin surface. The nozzle, which expels the air, is integrated into the sleeve design to limit the part count and lower the cost. After cutting the hole in the skin, the sleeve is attached to the bottom surface of the skin with the protruding nozzle extending into the hole. The sleeve contains a large outer

lip area that allows for more contact surface area between the sleeve and the bottom skin surface. This surface area provides the large bonding area needed to keep the sleeve in place and to prevent peeling off from the flap surface. The actuator attaches to the bottom surface of the sleeve with snapfits that hold the device in place and ensure proper compression on the sealant surface to prevent air leakage. The local curvature at the insertion point in the flap skin showed a more curved surface than was expected for the flap box region. The Internal sleeve model was adjusted to accommodate this curvature, as shown in Figure 4.25. The updated model has a local curvature to the sleeve lip that mimics that of the skin to allow for proper alignment between the two surfaces. The slotted hole that was created for the beam was adjusted to follow a curved path along the non-linear portion of the sleeve lip. The nozzle extension profile was updated to reflect the change in flap thickness in addition to the change in local curvature. This resulted in a deeper nozzle extension profile as the actuator was now at a position farther from the exit surface.

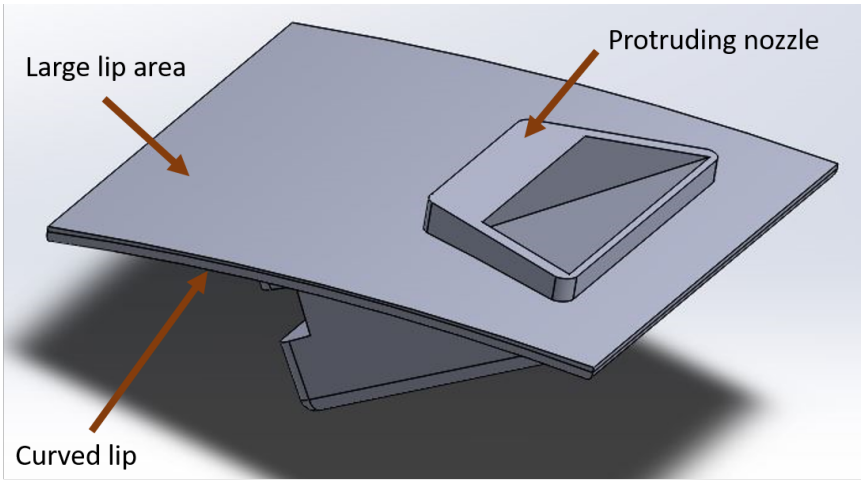

Figure 4.25: Final sleeve design

The backside of the sleeve is shown in Figure 4.26. The backside contains two crevices for the insertion of the snapfits. The top edges of the crevices are chamfered to facilitate the insertion of the snapfits without interference. A slot in the lip allows for the insertion of the actuator beam into the sleeve. This slot aids in orientation of the actuator during assembly,

as well as holding it securely.

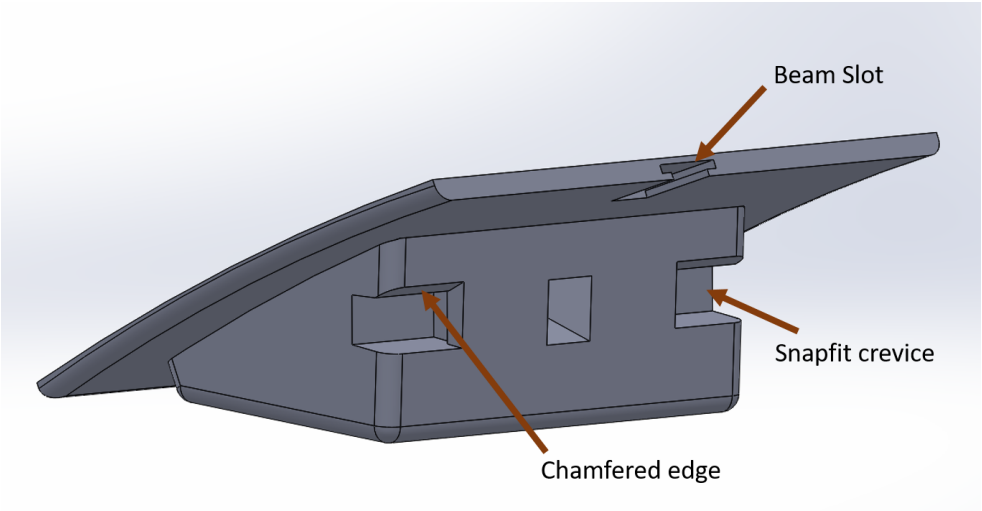

Figure 4.26: Final sleeve design backside

4.4.2 Physical Model

After generating the CAD model, a physical model was fabricated to create a visual mockup of the design. This model was made to the full scale dimensions of a generic flap wing with a 6” span, identical to the CAD model. The final design, represented as a physical mockup, is shown in Figure 4.27.

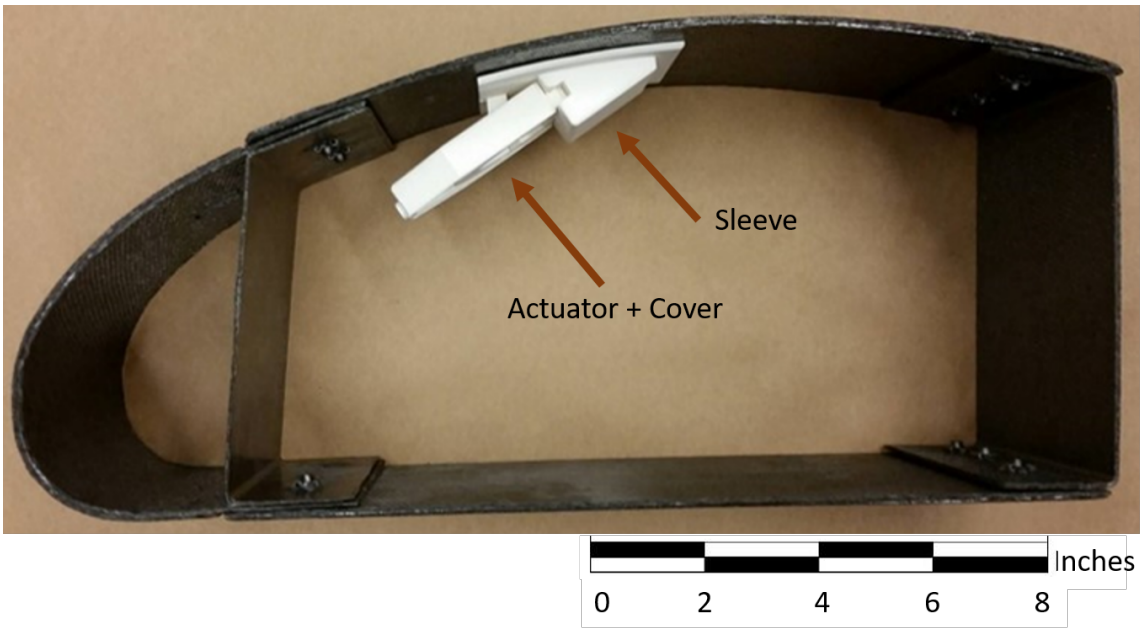

Figure 4.27: Final design visual mockup

The wing flap was created from CF laminate composed of eight layers of woven multi-directional lamina. Aluminum and high-temperature foam molds were used to create the spars and contoured surfaces. A waterjet cutter was used to create the hole cutout to insert the FO as shown in Figure 4.28.

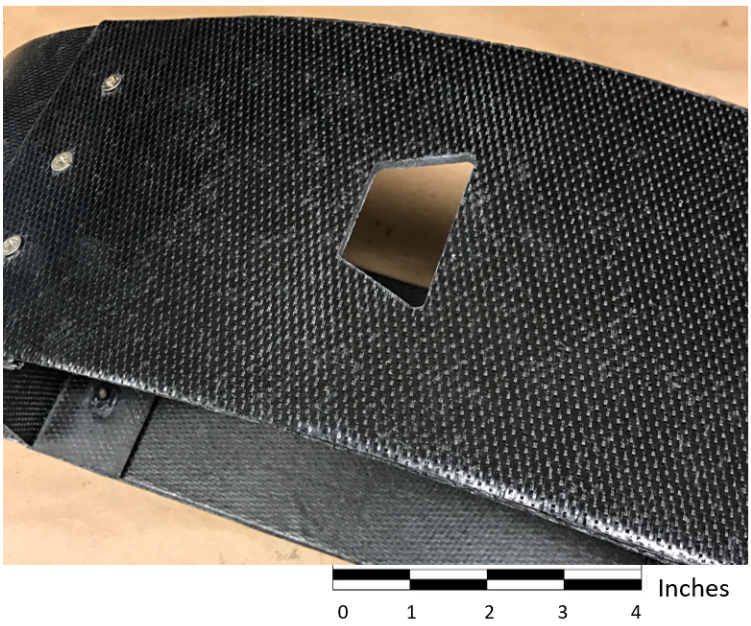

Figure 4.28: Cutout for FO insertion

The FO was created using a FDM 3D printing process. The FO was manufactured in three parts: sleeve, actuator, and actuator cover. The actuator utilized snapfits and a vertical beam to attach to the sleeve. The three individual FO parts are shown in Figure 4.29. The actuator in the figure contains a white box to hide proprietary material.

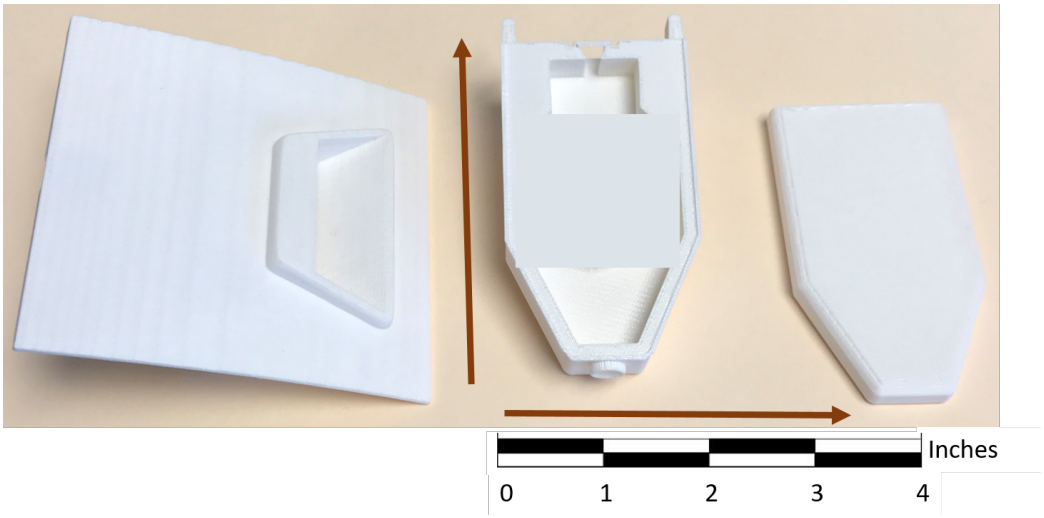

Figure 4.29: FO parts from left to right: sleeve, actuator, actuator cover

4.5 Chapter Summary

In this chapter, the top design was selected from each category of Internal, External, and Internal-External designs. These designs were discussed in more depth and with accurate dimensions in reference to the actuator sizing, angle of placement, and snapfit sizing. A final design based on the Internal design was then presented with both CAD and physical models. The final design was built on the dimensions of a full scale composite wing flap. The next chapter discusses the validation and simulations for the final design.

CHAPTER 5
VALIDATION

Validation of the designs consisted of two approaches: analyzing their structural stability, and analyzing their ability to be manufactured. In order to analyze structural stability, finite element analysis was used to model different loading conditions. A simulation was used to analyze the flow of the polymer material as it filled the injection mold. This helped identify manufacturability and possible flaws in the model that would appear during large scale production.

5.1 Finite Element Analysis

Finite element analysis (FEA) was used to validate the FO designs and model the loads that it would experience. The FEA was performed using ANSYS Workbench software. Validation testing was performed on three areas: attachment of the FO to the flap, attachment of the actuator to the sleeve, and insertion of the actuator into the sleeve.

5.1.1 FO to Flap Attachment

The first simulation tested how well the FO would stay attached to the flap under realistic applied loads. Commercial aircraft parts are generally tested to withstand weight loadings with up to nine times the acceleration of gravity (9G). Due to the insertion of the FO into a non-structurally loaded wing flap, no other external loads were studied. The reaction force generated from the air exiting the nozzle was also considered, but previous work has shown this force to be negligible [28]. The initial conditions for the simulation included a fixed flap surface and a bonded contact surface between the FO sleeve lip and the inside flap skin surface. The actuator is connected to the sleeve through the use of bonded contacts rather than frictional contacts, as the load of the actuator on the sleeve was of more concern than

the connection of the actuator to the sleeve, which is addressed in the next section. These two bonded contacts are shown in Figure 5.1. Ambient temperature conditions were used in the simulation.

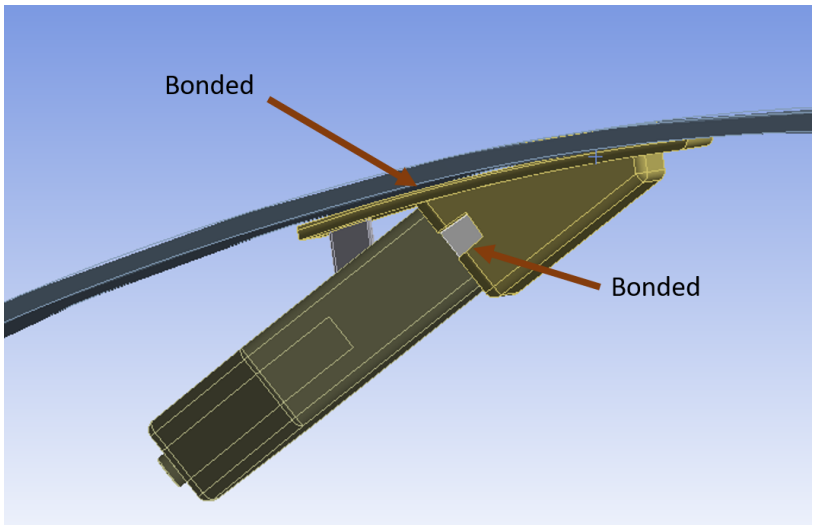

Figure 5.1: FO ANSYS connections

A mesh was automatically generated with enhanced mesh refinement applied to areas of interest, specifically around the hole where the FO would be inserted. Thus, mesh refinement was applied on both the flap surface region around the hole and the nozzle profile region of the FO. A small mesh size is important for areas of expected stress concentration as it increases the element count in that region to better estimate the true stress concentrations. Figure 5.2 shows a closeup of the FO sleeve, with the mesh refinement applied around the nozzle area.

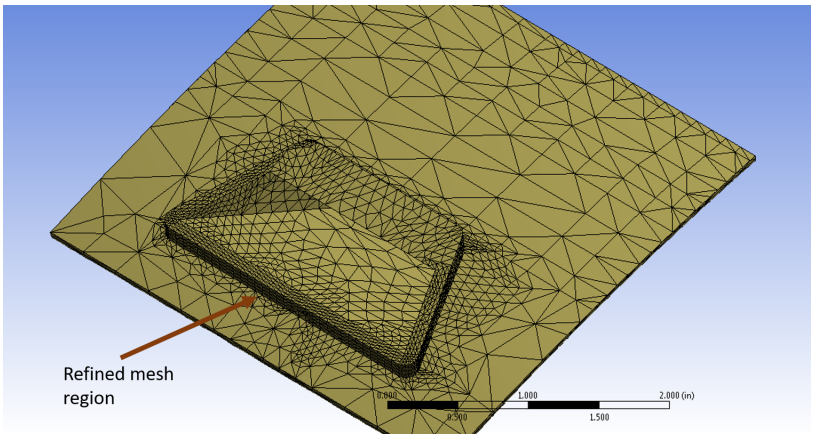

Figure 5.2: Refined mesh for FO sleeve

With the applied loads set, the simulation was performed to approximate the deformation and stresses along the FO. The FO experienced minimal deformation despite the 9G loading, with a maximum deformation of 0.00022" as seen in Figure 5.3. As expected, the maximum deformation came at the edge of the actuator connected to the sleeve. The actuator's long body creates a bending moment that causes its end to experience an additional loading leading to deformation. The sleeve's back lip section experiences some additional deformation due to the weight of the actuator pulling it down, and peeling it away from the flap surface. This is in contrast to the sleeve section that directly surrounds the hole in the skin as it experiences the least amount of deformation.

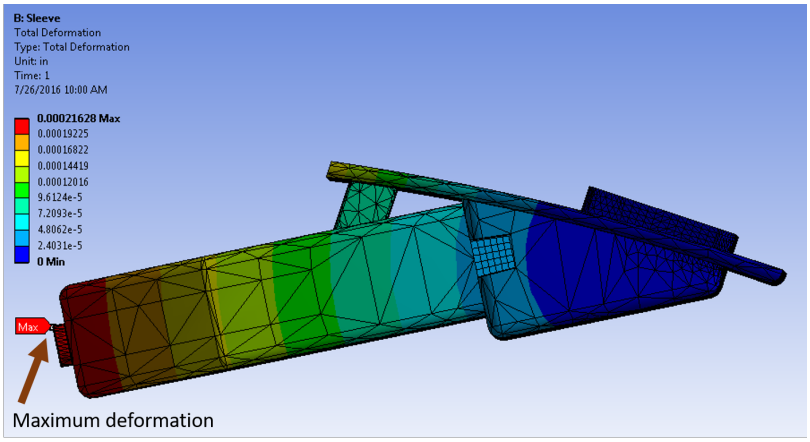

Figure 5.3: FO deformation

The maximum principal stresses were calculated to determine the stress concentrations

on the FO. The maximum principal stress was chosen over the von Mises stress evaluation due to the low ductility of PEKK. The CF reinforced PEKK has a maximum strain of about 1%, which is lower than the recommended strain of 5% for von Mises equivalent stress evaluation [41]. The stresses on the FO device can be seen in Figure 5.4. This simulation showed that the maximum expected stress was about 270 psi, which is much lower than the yield stress of CF PEKK which is about 8000 psi. This maximum stress concentration occurred around the edges of the nozzle profile that fit into the hole in the flap skin.

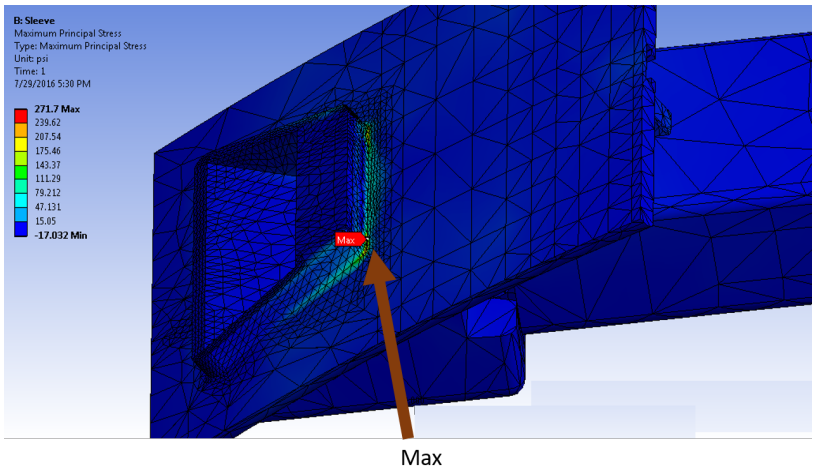

Figure 5.4: FO stress

5.1.2 Actuator to Sleeve Attachment

In addition to securing the FO sleeve in place to the flap, the connection point between the actuator and the sleeve was also tested. The snapfits are the main connection points between the sleeve and the actuator that secure the two parts and ensure a tight seal around the actuator nozzle. The beam protruding out of the top of the actuator was designed to insert into a groove in the sleeve to align it and to sustain loads due to the actuator weight in the vertical direction .

The sleeve had fixed constraints applied to its top surface, simulating the bonded connection between it and the flap surface. Section 5.1.1 validated that the sleeve would remain attached to the flap surface, and so, the fixed constraint was a valid assumption. A ”rough

surface constraint" was used between the actuator face and the sleeve face to allow the surfaces may separate if enough loading was applied. For the connection to between the snapfit hook faces (on the actuator) and the snapfit groove faces (in the sleeve), friction contacts were applied with a friction coefficient of 0.35 [40]. An overview of the connections on the FO are shown in Figure 5.5.

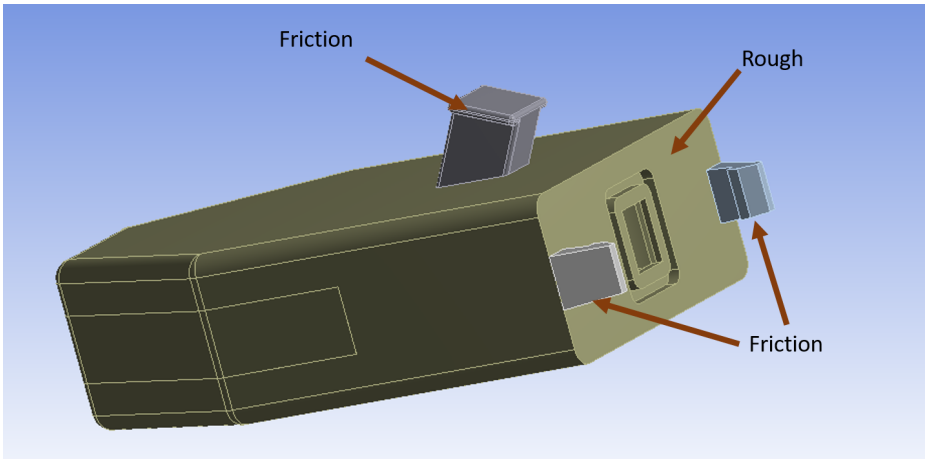

Figure 5.5: Actuator connections labeled for the simulation

Contact settings were adjusted to aid in the solution convergence. An Augmented-Lagrange formulation was used to solve the non-linear frictional problem. The Augmented-Lagrange was chosen over the Normal-Lagrange method due to the available symmetric contact points between the target regions, which prevents the snapfit hooks from penetrating the groove surface and vice-versa. An aggressive stiffness factor was applied that updated on each iteration, along with a specified pinball region of 0.003". These two controls specified the non-contact regions and gaps to facilitate solution convergence. Similar settings were used for the interface of the beam to the beam slot in the sleeve. A triangular mesh was applied, with mesh refinement around the snapfit and beam faces, as can be seen in Figure 5.6.

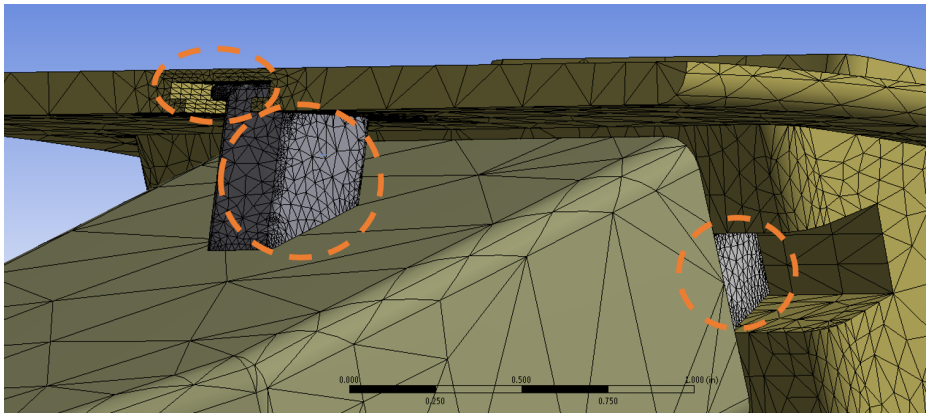

Figure 5.6: Actuator mesh, with refinement regions circled

Similar to the previous test, minimal deformation was found on the actuator, with the maximum also occurring at the end point. This can be seen in Figure 5.7. The maximum stress on the actuator was found to be well within the acceptable range. 30% CF PEKK has a yield strength of about 8000 psi, and the maximum stresses experienced on the device were far below that, at about 470 psi. This can be seen in Figure 5.8.

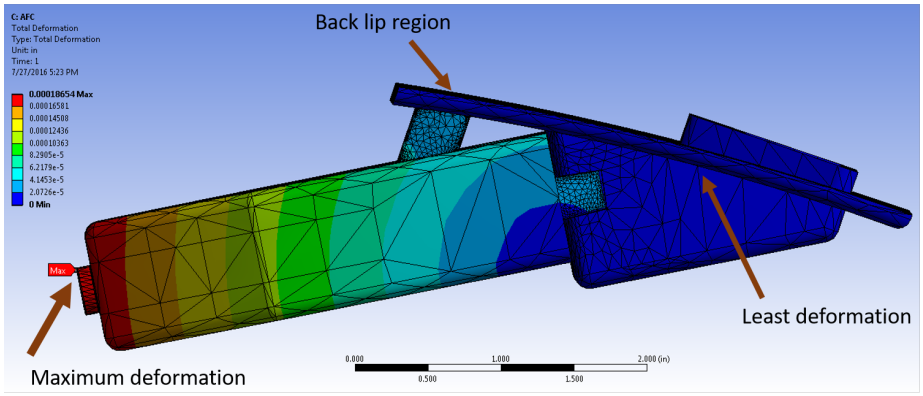

Figure 5.7: Actuator deformation

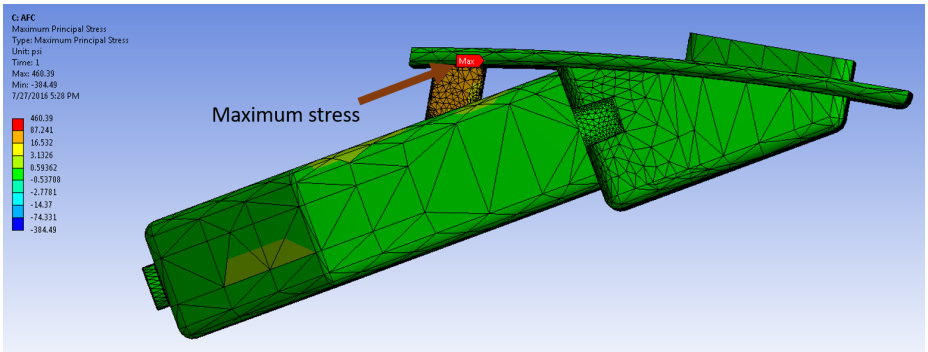

Figure 5.8: Actuator maximum stresses

An area of concern during design was whether the thin member of the beam top surface would get damaged after repeated use. After running this test to determine if it would handle the loads under an acceleration of 9G, another test was run to determine the fatigue of the part after sustaining this load for multiple cycles. Using the same model and loads, a fatigue test was run in ANSYS to determine how well the part resisted repeated loads.

A fatigue model with fully reversed loading was used. This applied the force from the 9G weight onto the FO in both the positive and then negative directions, and also oscillated between the two directions. A stress life model was used to analyze the cycles for the FO based on stress leading to failure. Similar to the Static tests, the Maximum Principal Stress was used instead of the von-Mises Stress to account for the material's low ductility. Data for the fatigue SN curves were estimated using data from Victrex on 30% CF PEEK, which closely resembles the structural properties of PEKK [42]. Ambient temperature conditions were also used for the fatigue simulation. The results of the fatigue test are shown in Figure 5.9.

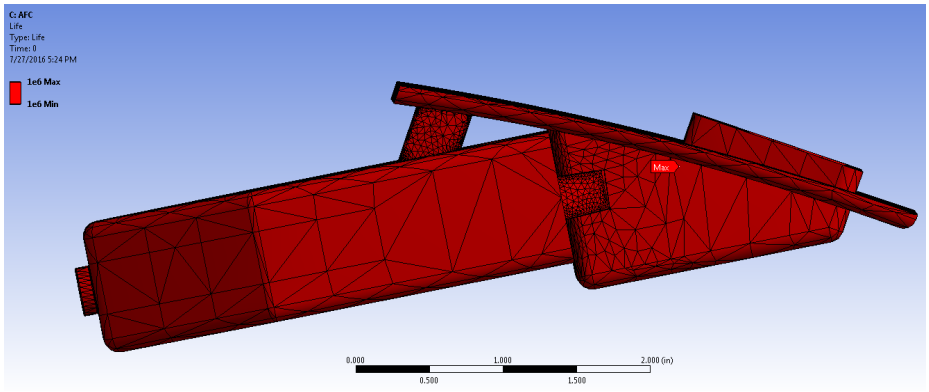

Figure 5.9: Actuator fatigue life

This figure indicates that infinite life is reached throughout the whole FO as shown by the red color encapsulating the part, signifying that at least 1E6 cycles were reached for all regions of the part without failure. Once a part is verified to reach infinite life (1E6 cycles), the software does not calculate how many cycles are actually attained.

5.1.3 Snapfit Connection

After testing whether the thin members of the beam and the snapfit would support the sustained loads at 9G, another fatigue test was run to determine if the snapfit and beam connecting parts would sustain repeated loads caused by the insertion and detachment of the actuator from the sleeve. The snapfits were designed to require a total attachment force of about 12 lbf, as discussed in Chapter 4. The force due to friction during insertion was the product of the coefficient of friction and the normal force due to the actuator weight, resulting in a force of 0.07 lbf. The friction force combined with the snapfit assembly force resulted in a total force of 6.07 lbf for each beam. This was applied to each snapfit on the actuator. The results from the fatigue test confirmed infinite life for all the members; however, the equivalent stresses were the regions of highest stress concentrations. The results from the fatigue test with regards to the equivalent stresses are shown in Figure 5.10.

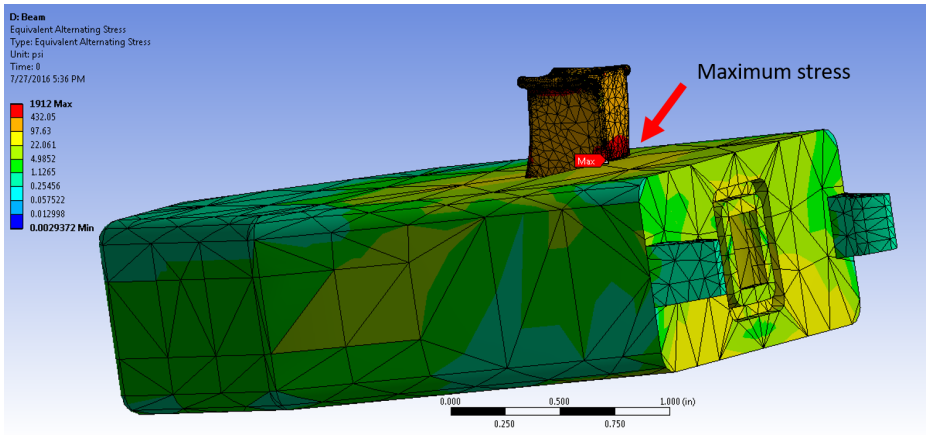

Figure 5.10: Beam fatigue stresses

As can be seen, the highest stress concentration regions occurred at the edge of the base that is part of the actuator. The front edge experienced the highest principal stress of 1912 psi. This high stress was expected as the beam acts like a fixed-free column subjected to a normal force that creates a bending moment. The stresses on the beam can be viewed more clearly by observing the total deformation experienced by the actuator, as seen in Figure 5.11. The highest deformation occurred at the beam's top edges, which were the thinnest members and also the primary edges subject to the frictional forces upon insertion into the sleeve slotted groove.

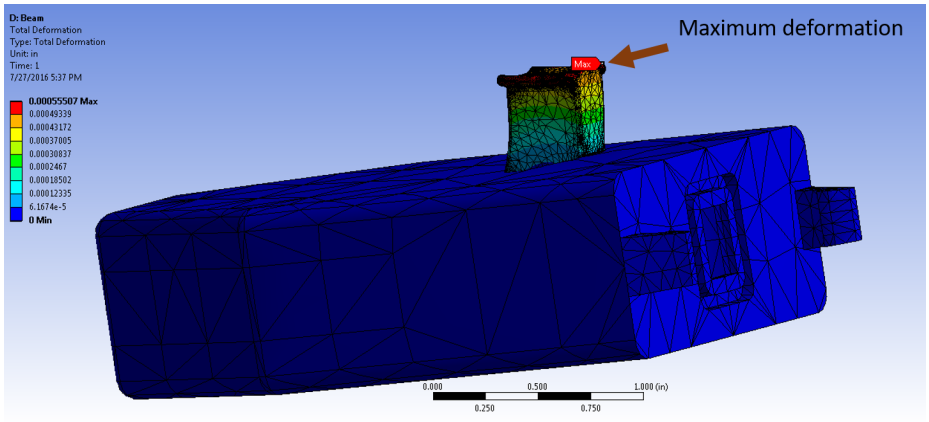

Figure 5.11: Beam fatigue deformation

After testing the actuator side of the beam for the fatigue analysis, an equivalent test was run on the corresponding region of the sleeve. The sleeve was fixed by its top face,

simulating bonded attachment to the flap skin. The insertion force due to the snapfits and friction were applied on the inner edges of the slotted groove, and the fatigue test was run. The uniform red color in Figure 5.12 demonstrates that infinite life was attained once again for the entire part.

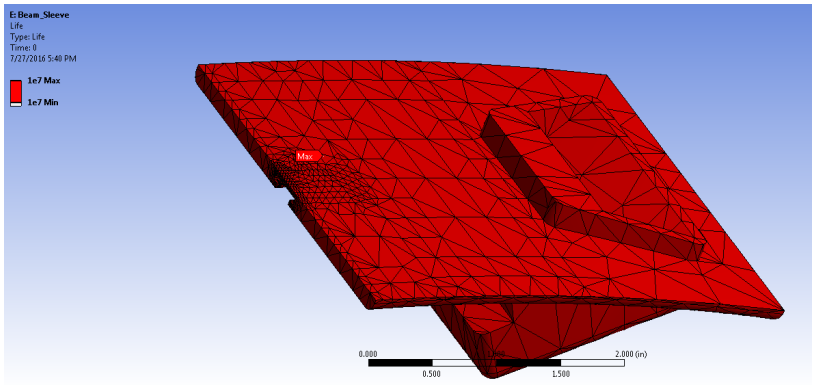

Figure 5.12: Beam sleeve fatigue life

The equivalent principal stresses were also observed for the the sleeve. As expected, the sleeve slotted groove experienced the highest stresses due to its structurally thin members. The maximum deformation of 386 psi occurred at the inner top edge of the slotted groove, as seen in Figure 5.13. The figure also shows the mesh on the sleeve, with a refined mesh applied around the groove area to more accurately predict the stress concentrations in that region.

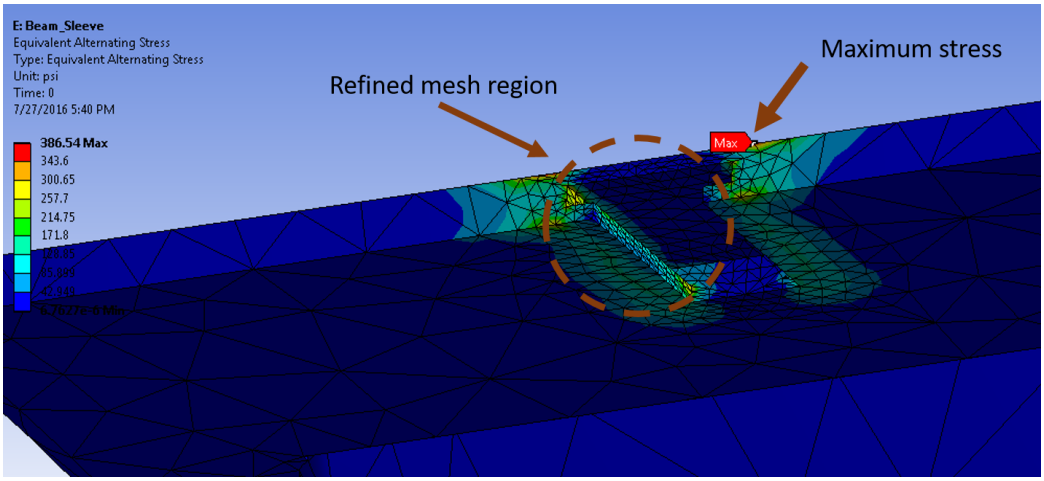

Figure 5.13: Beam sleeve fatigue stresses

5.2 Injection Molding Simulation

Injection molding (IM) was modeled using the Plastics package from SolidWorks software to simulate molding flow and identify potential problematic issues. Analysis tools included fill time, injection pressure, cooling time, and fluid flow. These tools were run for the three component parts of the FO: actuator, actuator cover, and sleeve.

5.2.1 Actuator IM

A volumetric mesh was applied to the model with sizing adjusted for detailed sections such as the air inlet and outlet regions. A volumetric mesh was used instead of the surface mesh to obtain a more balanced gate contribution, and thus, a more accurate fluid flow. A 30% CF PEEK material was chosen from the library due to its similar viscous properties to CF PEKK. An automatically-generated gate was used for the initial run with a diameter of 0.35” and was placed on the back side of the actuator above the horseshoe. This resulted in a “short shot” as the material did not completely fill the mold as shown in Figure 5.14 by the unfilled grey region at the top.

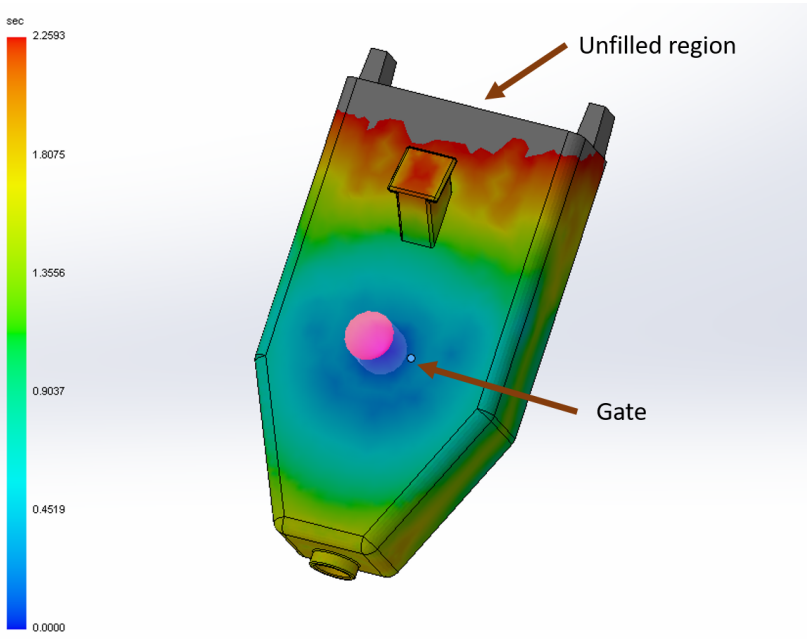

Figure 5.14: Actuator IM short shot

The central temperature at the end of the fill reached 743°F and did so with a fill-time of 1.82 sec. The cooling time was fairly large with a value of 67.95 sec. This was mainly due to the thick parts at the top shoulders of the actuator. These thicker sections also led to sink marks. The high potential regions for sink marks are shown by the red sections that require a large cooling time in Figure 5.15. The figure shown includes a grayed out region to hide proprietary material.

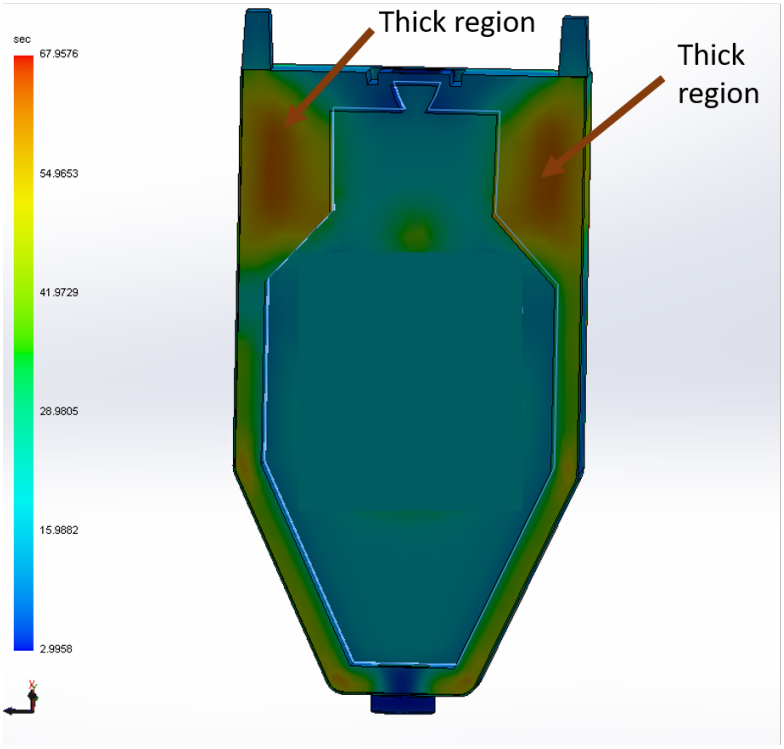

Figure 5.15: Actuator IM cooling time

The gate was then relocated to the bottom edge of the actuator and this resulted in a completely filled mold.The actuator design was further refined by having the thicker sections hollowed out by creating shelled inner surfaces. While this resulted in a slightly lower part weight, its main savings came in the form of the reduced cooling time and the reduction of sink marks. Shelling out the thick sections resulted in a cooling time that was much less than the previous design (40.44 sec, compared to 67.95 sec), and a slightly shorter fill time of 1.82 sec. The gate diameter was also adjusted to reduce its

contact area on the actuator surface; therefore, a gate diameter of 0.20” was chosen. The injection pressure needed was 2041 psi, which was less than 60% of the maximum. The final actuator design is shown in Figure 5.16. This figure shows the predicted sink mark regions are significantly reduced from the earlier design. Dark regions indicate a sink depth of about 0.0001” while the majority of the part has a sink depth of 0.0008”. These small depth values indicate that sink marks should not pose an issue in the FO manufacturing. The part cavities and entrance gate can also be seen in the figure. The figure shown includes a grayed out region to hide proprietary material.

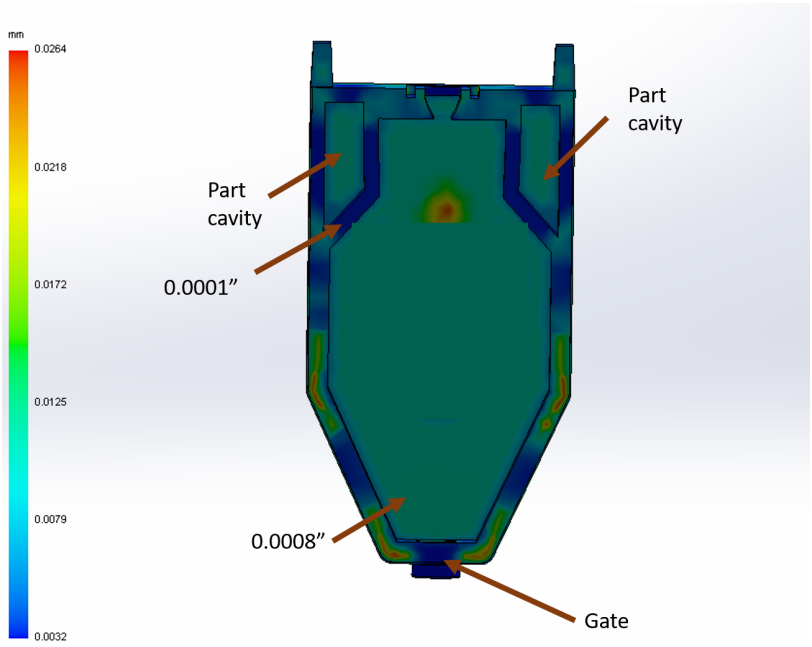

Figure 5.16: Refined Actuator IM sink marks

5.2.2 Actuator Cover

The injection molding analysis was performed on the actuator’s top cover. This was manufactured as a separate part due to the inability to manufacture a mold for the inner surfaces with a closed section on top. The simple shape of the flat cover resulted in a straight forward IM flow analysis. The part is shown in Figure 5.17 which shows the part fill time. The pink cylindrical gate is shown at the bottom.

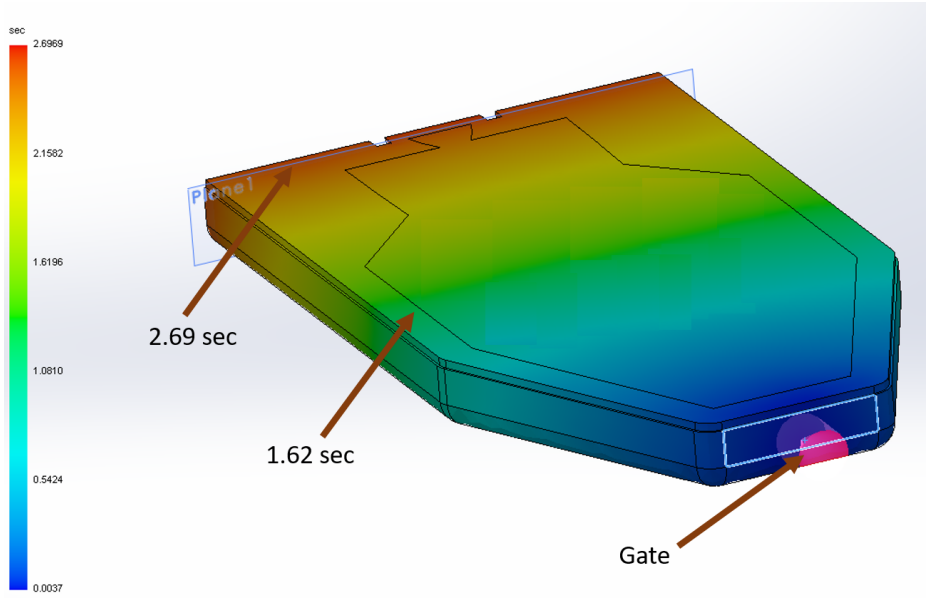

Figure 5.17: Actuator Cover IM fill time

A gate size of 0.12” located at the bottom surface near the bottom edge resulted in a 1.1 sec fill time and a 5.19 sec cooling time. The cover required an injection pressure of 5808 psi, which was less than 60% of the maximum injection pressure. Figure 5.18 shows a plot of the maximum injection inlet pressure required over time, which follows a linear relationship. The linear behavior is expected, because as the cavity is filled, there is more viscous resistance to the melted plastic, which causes the cavity pressure to increase. This in turn requires more injection pressure as the time to fill the cavity increases.

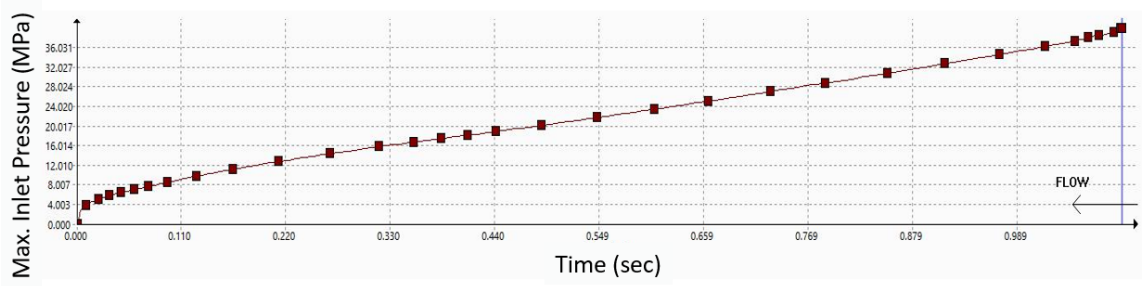

Figure 5.18: Actuator Cover IM pressure vs time

5.2.3 Sleeve

The final IM analysis was performed on the FO sleeve. This part was more difficult to IM because the sleeve was produced as one part rather than as two separate halves. It was critical for the sleeve to be one part as any parting line that overlaps the nozzle exit would disrupt air flow and result in decreased FO performance. Thus, the sleeve was designed as one part, resulting in numerous side pulls. Two gates of diameter 0.2" were initially used to help fill the mold. These were placed on either side of the exit nozzle on the top surface as shown by the red dots in Figure 5.19. This resulted in a weld line at the intersecting flow region between the two gates. This was deemed unsatisfactory as this weld line may negatively affect the air stream at the nozzle surface, and compromise the part's integrity.

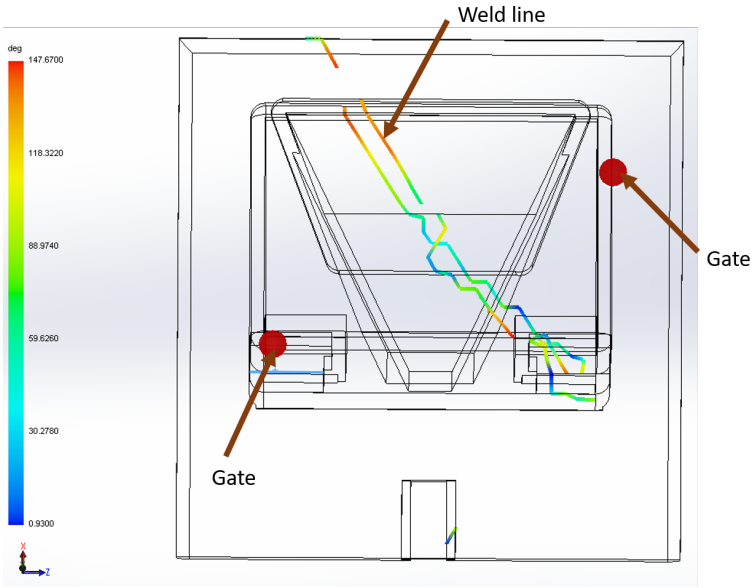

Figure 5.19: Sleeve IM weldline

Thus, a single gate was selected with a larger gate diameter of 0.31". Figure 5.20 shows the gate location at the center top surface of the sleeve. The part had a fast fill-time of 2.87 sec and a cooling time of 50.08 sec. The injection pressure required for this part was rather high at 10,193 psi . Although this pressure was high, it was still less than the 14,500 psi maximum injection pressure (Solidworks). The software analysis toolbox

showed that designs between 50%-90% of the maximum injection pressure posed no issues, and this design was at 70.27% of the maximum pressure, which satisfied the constraint. Low injection pressures may result in short shots, while pressures that are too high may result in flash and less uniform mold flow. This gate location also moved weld lines away from air flow regions as seen in Figure 5.20.

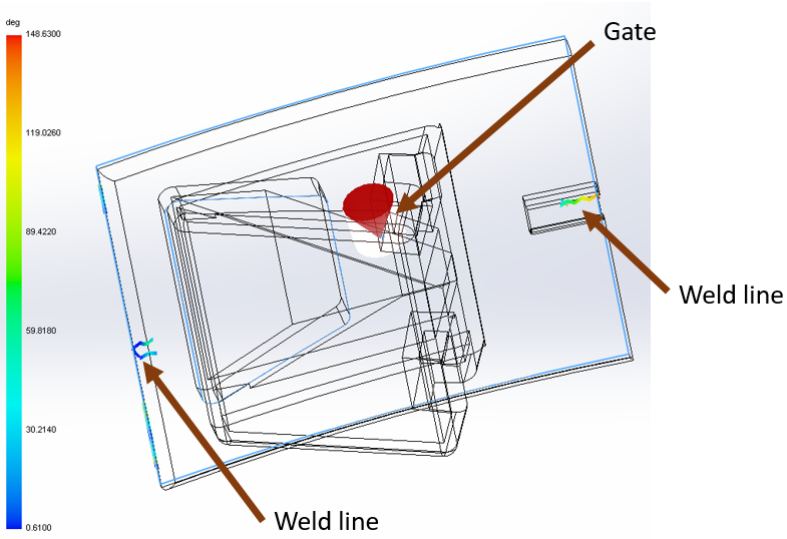

Figure 5.20: Sleeve IM weld lines

5.3 Chapter Summary

This chapter discussed the simulations performed to validate the final design. A series of FEA tests were conducted on the FO, along with molding flow simulations. For the FEA, the FO was first tested to see if it could stay attached to the flap while sustaining the flap loads. After successful validation, the actuator to the sleeve attachment was investigated, which included fatigue testing of the model. After that, mold flow simulations were conducted to identify the feasibility of injection molding each of the FO parts. These simulations resulted in design refinements, specifically with the FO actuator to make it more feasible for IM. The next chapter discusses the cost analysis for the manufacturing of each of these components dependent on the manufacturing process used.

CHAPTER 6
COST ANALYSIS

A cost analysis was performed to determine the cost of the FO with regards to large scale production. The cost was divided into manufacturing cost, material cost, and assembly cost. Calculations for the material and assembly costs were similar across different processes, but the manufacturing cost calculation differed for injection molding and SLS 3D printing. Lastly, costs were compared for parts using different processes and different combinations to produce a low-cost final product.

6.1 Manufacturing Cost

The two manufacturing processes, IM and 3D printing, resulted in two very different approaches to calculate the unit cost for each FO. While the IM analysis used empirical data to calculate the monetary cost of the mold, the 3D printing modeled the cost based on the time required at each stage of the printing process.

6.1.1 IM Cost

Following the principles of design for manufacturing and assembly (DFMA), the injection molding cost was calculated as the cost of the mold to create the parts [39]. In order to calculate the cost of the mold, the part geometry affected several factors such as the number of side pulls, number of internal lifters, and geometrical complexity. As a result, a mold cost was rated by points, where points equated to hours of mold manufacturing. The components of this point system are listed below:

1. Projected area of part (cm^2)
2. Geometric Complexity

3. Side-Pulls

4. Internal Lifters

5. Unscrewing Devices

6. Surface Finish

7. Tolerance Level

8. Texture

9. Parting Plane

The geometric complexity factor was based on the complexity ratings of the inner and outer surfaces of the part. The inner surface is the surface that contacts the main core during molding. Equation 6.1 shows this relationship between the inner and outer part complexity (X_i, X_o respectively) and the manufacturing hours required. The part complexity (X), shown in Equation 6.2, is a factor of the number of surface patches (N_{sp}) of the inner or outer surface. A surface patch is a surface that has a constant or smoothly changing curvature; two surface patches are separated by a sudden change in either slope or curvature.

$$M_x = 5.83(X_i + X_o)^{1.27} \tag{6.1}$$

$$X = 0.1N_{sp} \tag{6.2}$$

Side pulls are required when creating a mold for a design that has external depressions or holes parallel to the parting plane; these are known as undercuts. Due to these undercuts, the mold requires additional pulls mounted on slides to pull apart the mold in more than one direction. The number of side pulls was calculated for each of the FO components. The actuator required one side pull due to the inclusion of the top beam at a slight angle.

The actuator cover did not require side pulls as it was just a flat plate. The sleeve required two side pulls, one for the beam slot and another for the nozzle opening.

Internal lifters are needed whenever there are mold depressions or undercuts on the inside of a part [39]. A core pin is needed to retract the pin that retracts the device within the main core; this is usually very costly. However, none of the designs required internal lifters. Additionally, since no screws were used in the designs, the number of mold manufacturing hours for unscrewing devices was zero for all parts.

The Surface Finish was calculated as the surface finish percentage factor multiplied by the sum of the points of the projected area and geometrical complexity. The percentage increases were found using Table 6.1.

Table 6.1: Percentage Increases for Appearance Levels [39]

Appearance	Percentage Increase (%)
Not Critical	10
Opaque, standard (SPE #3) Cover	15
Transparent, standard internal flaws or waviness permissible	20
Opaque, high gloss	25
Transparent, high quality	30
Transparent, optical quality	40

The Tolerance Level was found by multiplying the tolerance percentage factor by the geometrical complexity points. The percentage factor was given by Table 6.2.

Table 6.2: Percentage Increases for Tolerance [39]

Tolerance Level	Description of Tolerances	Percentage Increase (%)
0	All greater than ± 0.5mm	0
1	Most approx. ± 0.35mm	2
2	Several approx. ± 0.25mm	5
3	Most approx. ± 0.25mm	10
4	Several approx. ± 0.05mm	20
5	Most approx. ± 0.05mm	30

Since no texture patterns such as checkers or leather grain were used on any of the parts, the number of mold manufacturing hours was zero for the Texture component.

Lastly, the Parting Plane points were calculated using Equation 6.3 which used the projected part area (A_p) and the parting plane factor (f_p) given by Table 6.3 [39].

$$M_s = f_p A_p^{0.5} \tag{6.3}$$

Table 6.3: Parting Surface Classification [39]

Parting Surface Type	Factor (f_p)
Flat parting plane	0
Canted parting surface or one containing a single step	1.25
Two to four simple steps or a simple curved surface	2
Greater than four simple steps	2.5
Complex curved surface	3
Complex curved surface with steps	4

The mold cost point system was used for each part to calculate the total mold hours required. The cost was obtained by multiplying the total time required by the mold labor

rate $40 per hour [35]. These results are summarized by Table 6.4.

Table 6.4: IM mold costs for each component

Configuration	Mold Cost ($)
Actuator	$6462
Actuator Cover	$1565
Sleeve	$9286

6.1.2 3D Printing Cost

The cost calculations for the SLS 3D printing process used a cost model developed by Ruffo that estimates manufacturing time based on model geometry [43]. The model is composed of three parts: recoating time (t_z), scanning time (t_{xy}), and pre and post processing time (t_{HC}). The three are combined to form the total build time (t_{tot}) shown by Equation 6.4.

$$t_{tot} = t_z + t_{xy} + t_{HC} \tag{6.4}$$

The recoating time (t_z) is composed of the time in seconds that the machine needs to add layers of powder to create successive layers. The gradient for the recoating time is based on the time to reposition the laser to a bed corner after scanning the build section. This gradient is a factor of the External Packing Ratio (Pr) shown in Equation 6.5.

$$Pr = \frac{V_{ext}}{V_{bed}} \tag{6.5}$$

This factor is a ratio of the volume of the geometrical box containing the entire part divided by the volume of the entire machine bed. The geometric boundary box can be viewed as the minimum dimensions for a rectangular solid to envelope the part. An example of the bounding box for the sleeve part is shown by Figure 6.1.

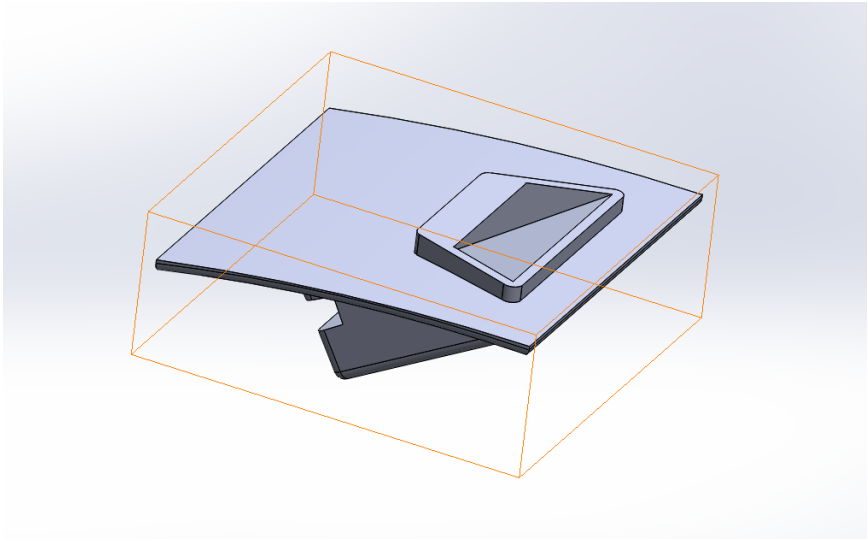

Figure 6.1: Geometric bounding box for the sleeve

Based on empirical data for the 3D Systems Vanguard SLS machine, Equation 6.6 was created as an approximating function for calculating the recoating time in seconds where z is the height of the part [43].

$$t_z = (180 - 120 * Pr) * z + 400 \tag{6.6}$$

The scanning time is highly variable as it is based on the part shape, but an approximate function was developed by Ruffo that estimated the time with a slight overestimation. This function is shown by Equation 6.7 [43].

$$t_{xy} = \gamma(0.042L^{-0.1809} * LW) * z \tag{6.7}$$

The scanning time is based on the part's bounding box along with the compact ratio (Cr) given by Equation 6.8 as the ratio of the part volume (V_b) by the part geometric bounding box volume (V_{ext}). Based on the value computed for the compact ratio, two different relationships may be obtained to connect the part volume and bounding box volume

highlighted by the variable gamma (γ) in Equation 6.9.

$$Cr = \frac{V_b}{V_{ext}} \tag{6.8}$$

$$\gamma = \begin{cases} 0.3422Cr^2 + 0.2468Cr + 0.45, & \text{for Cr<0.4} \\ 0.417e^{0.9283Cr}, & \text{for Cr>0.4} \end{cases} \tag{6.9}$$

Finally, the third element of the total build time equation is the pre and post processing time. This is based on the heating and cooling times required for the part during printing. The two processes are constant and set up by the user, and can be normally evaluated by a time of 60 min or 3600 sec.

Based on the equations given by Ruffo, the total build time was approximated for each individual part along with combination of parts together. The cost for each part was obtained by multiplying the total time required by the indirect assembly cost of an hourly wage technician obtained at $18 per hour [35]. These results are summarized by Table 6.5. The last row in the table shows the cost for creating the entire FO as one component instead of creating each part separately.

Table 6.5: SLS costs for different configurations

Configuration	Build Time (hours)	Cost ($)
Actuator	3.24	$3.24
Actuator Cover	1.43	$1.07
Sleeve	3.91	$5.87
Actuator + Cover	3.30	$3.30
FO One Part	7.32	$21.96

6.2 Material and Assembly Cost

The material and assembly costs were independent of the manufacturing process used. The material cost depended on the price of the material and the amount of material used. The assembly cost was calculated based on the handling time and insertion time for each component.

6.2.1 Material Cost

The material cost was calculated by Equation 6.10 as the product of the cost of the material (C_{mat}) and the weight of the part (m_{part}) in lbm. For 30% CF PEKK material, the cost was taken as the average material rate of $62.5 per lbm [44]. The material cost for each part is summarized in Table 6.6.

$$C_m = C_{mat} m_{part} \tag{6.10}$$

Table 6.6: Material cost for each component

Configuration	Material Cost ($)
Actuator	$6.25
Actuator Cover	$1.88
Sleeve	$12.50
Total Cost	$24.13

6.2.2 Assembly Cost

The first component of the assembly cost is the handling time. This consists of the time to grasp and manipulate a part without the aid of a grasping tool. This is highly dependent on part symmetry, which is broken up into alpha and beta symmetry. Alpha symmetry relates to the angle that the part is rotated about an axis perpendicular to the axis of insertion.

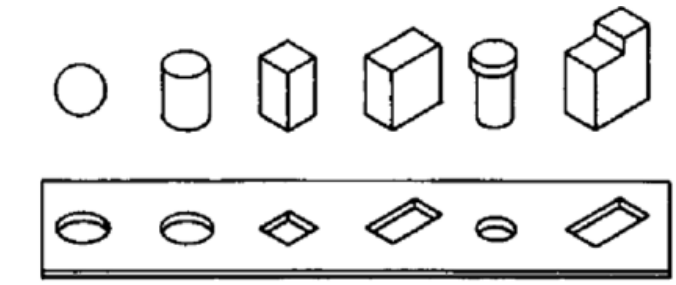

α	0	180	180	90	360	360
β	0	0	90	180	0	360

Figure 6.2: Part Angle Symmetry

Beta symmetry relates to the angle that the part is rotated about its axis of insertion. The difference between these two angles is highlighted by Figure 6.2. The handling times for different parts are shown in Table 6.7.

Table 6.7: Part Handling Times [39]

		no handling difficulties			part nests or tangles		
		thickness > 2mm		< 2mm	thickness > 2mm		< 2mm
sym (deg) = (alpha+ beta)		size > 15mm	6mm < size < 15mm	size > 6mm	size > 15mm	6mm < size < 15mm	size > 6mm
		0	1	2	3	4	5
sym < 360	0	1.13	1.43	1.69	1.84	2.17	2.45
360 <= sym < 540	1	1.5	1.8	2.06	2.25	2.57	3.0
540 <= sym < 720	2	1.8	2.1	2.36	2.57	2.9	3.18
sym = 720	3	1.95	2.25	2.51	2.73	3.06	3.34

The insertion time was also based on predetermined time standard systems for assembly times in industry [39]. The insertion time depended on factors such as the axis of insertion, visual obstructions to the insertion, part thickness, and ease of alignment. The insertion time for standard parts were calculated using Table 6.8.

Table 6.8: Part Insertion Times [39]

		secured by separate operation or part				secured on insertion by snap fit	
		no holding down required		holding down required			
		easy to align	not easy to align	easy to align	not easy to align	easy to align	not easy to align
		0	1	2	3	4	5
no access or vision difficulties	0	1.5	3.0	2.6	5.2	1.8	3.3
obstructed access or restricted vision	1	3.7	5.2	4.8	7.4	4.0	5.5
obstructed access and restricted vision	2	5.9	7.4	7.0	9.6	7.7	7.7

The handling time and insertion time were found for each component and summed for a total time. This total time was monetized using the indirect assembly cost of an hourly wage technician at $18 per hour. The results for each part are shown in Table 6.9. This table includes parts for all manufacturing configurations.

Table 6.9: Assembly Time Cost for each component

Component	Handling Time (s)	Assembly Time (s)	Total Time (s)	Cost ($)
Actuator	1.50	4.00	5.50	$0.03
Actuator Cover	1.80	2.60	4.40	$0.02
Sleeve	1.95	4.80	6.75	$0.03
Actuator + Cover	1.50	4.00	5.50	$0.03
FO One Part	1.95	4.80	6.75	$0.03

6.3 Design Configuration

After compiling the data for the cost of each part using each manufacturing process, the total FO costs were calculated for the eleven different design configurations listed in Table 6.10. The configurations include the complete scenarios for each part option.

Table 6.10: Manufacturing Design Configurations

Configuration #	Actuator	Cover	Sleeve
1	IM	IM	IM
2	SLS	IM	IM
3	SLS	SLS	IM
4	IM	SLS	SLS
5	SLS	IM	SLS
6	IM	SLS	IM
7	SLS	SLS	SLS
8	IM	IM	SLS
9	SLS One Part		SLS
10	SLS One Part		SLS
11	SLS One Part		

The total cost is a function of the number of parts produced, as well as other factors. For 3D printed components, there was also the variable manufacturing cost associated with printing each individual part. For the IM configurations, there was the fixed mold cost along with the variable assembly cost per part. Thus, for IM parts, the cost continued to decrease as the number of parts produced increased. A comparison of these design configurations is shown in Figure 6.3. Here the unit cost is compared based on the number of FO produced from 0-10,000 parts. As can be seen, the IM parts start off with a fairly large initial cost before dropping to under $40 per part after about 1000 parts. This is highest for Configuration 1 which consists of all IM parts and thus requires three separate molds to be manufactured. Configuration 7, which has all 3D printed parts, is depicted by the horizontal line. The line is horizontal because the FO unit cost is independent of the number of units produced.

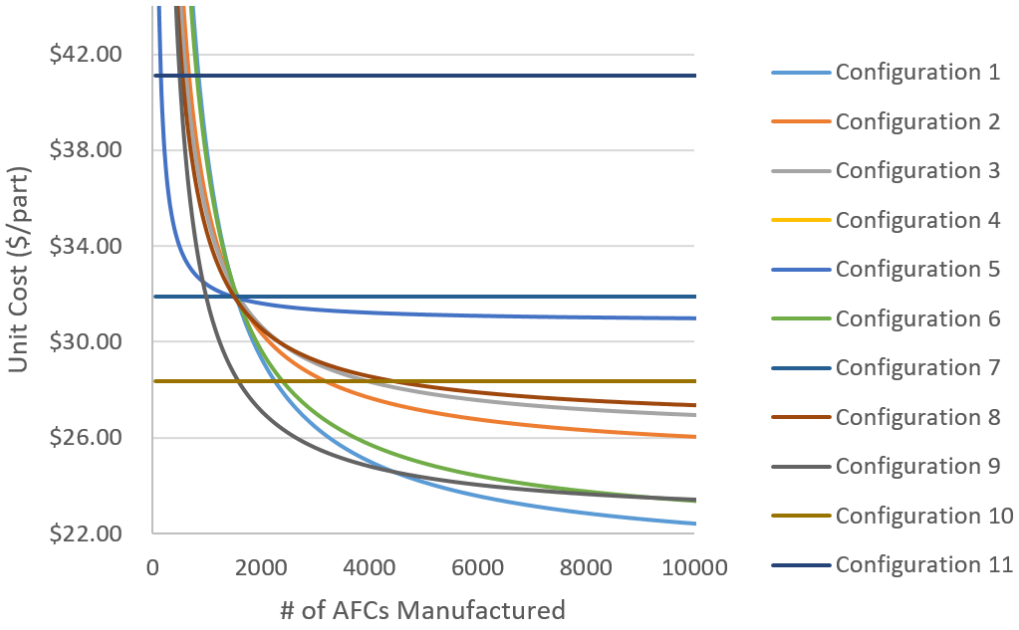

Figure 6.3: Design Configurations Unit Cost

Looking at the above figure in more detail, the disparities between each configuration are more clearly seen. Figure 6.4 depicts these disparities and clearly shows that IM parts have lower costs as more FOs are produced. Configuration 1, which starts off with the highest initial cost, ends up being the most cost efficient configuration for production of greater than 4550 parts. Configurations more reliant on SLS printing level off at higher unit costs, such as with Configurations 5, 7, 10, and 11.

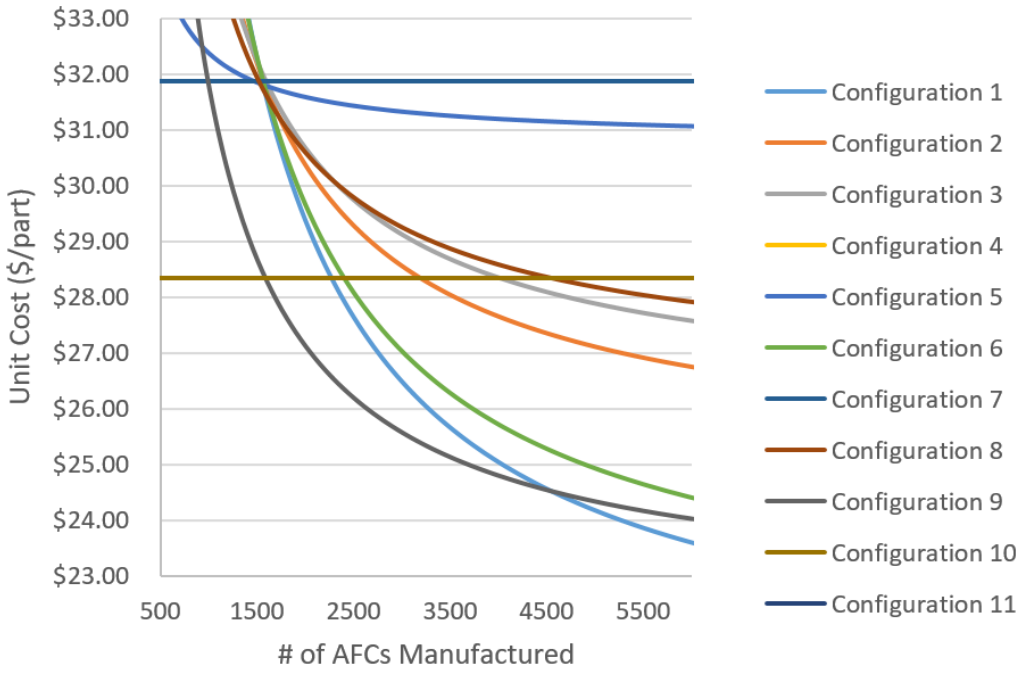

Figure 6.4: Design Configurations Unit Cost Zoomed

It should be noted that although Configuration 1 yielded the lowest cost, Configuration 6 was a close second, which had IM used for both the actuator and the sleeve, but SLS for the cover. This is understandable, as the actuator and sleeve are both more complex and larger parts that take more time to print and thus would require a large manufacturing cost. However, the cover is a small thin part without complex geometry, and so, its low 3D printing cost is similar to the IM manufacturing cost due to the large initial mold cost. It should be noted that when more than 10,000 parts are produced, the difference in cost between the IM and SLS printed Cover part becomes more apparent.

By comparing the unit costs of the different FO manufacturing configurations based on the number of parts produced, a decision can be made on which configuration to use. For any number of parts less than 1600, Configuration 10 should be used, in which the actuator and cover are one SLS part and the sleeve is produced separately. This configuration prints at a fixed cost of $28.35 per part. For part numbers greater than 1600 but less than 4550, Configuration 9 should be used, which creates the actuator and cover as one SLS part and then uses IM for the sleeve. At the lower end of 1600, parts cost $28.35 and reduce to

$24.53 for production closer to 4550 parts. For parts produced in excess of 4550, Configuration 1, which uses all IM parts, should be utilized to produce parts starting at $24.53, but reduces down to $22.43 at 10,000 parts.

6.4 Chapter Summary

This chapter provided a cost analysis for the FO production. Cost was segmented into the manufacturing, material, and assembly costs. The manufacturing costs were calculated using IM and 3D printing to produce parts. The material cost depended on the material volume used during production, while the assembly cost included the orientation angles, part symmetry, and ease of handling. Lastly, different part manufacturing configurations were created and the cost large production volumes determined. IM was found to be the most cost-efficient for quantities greater than 4550, while a combination of SLS and IM was beneficial for quantities less than that but greater than 1600. SLS 3D printing was the most cost-efficient for any production run less than 1600. In the next chapter, concluding remarks are made for the entire work.

CHAPTER 7
CONCLUSION

7.1 Summary

The primary goal of this thesis was to design an attachment mechanism for a fluidic oscillator (FO) to fit into a wing flap. Doing so could lead to potential savings of 3.2% in drag for the vehicle [33]. Previous research has shown the usefulness of such devices on airplane structures, but little work has been done on the attachment and large volume manufacturing considerations for these FOs onto aircraft structures.

Firstly, customer attributes were collected to generate the design functional requirements and design parameters. These were used to create uncoupled designs that follow the principles of Axiomatic Design. A sensitivity analysis and design of experiments were used to evaluate how the design rankings would change based on changes in the cost parameters. Four cost parameters were investigated to observe their effects on design rankings: material cost, assembly time, material density, and wing skin thickness. All four parameters were found to be significant at a 0.05 significance level and were found to have a strong correlation for design cost with an R^2 value of 0.9942. From the sensitivity analysis and DOE, it was found that although costs changed when parameters were varied, the overall ranking of the designs remained unchanged.

A final design that satisfied all functional requirements was created on the dimensions of a full-scale composite wing flap, with the wing skin assumed to be removable. Figure 7.1 shows the final FO attachment design, and Figure 7.2 shows the constituent FO parts. The prototype uses ABS plastic, while the final design is composed of carbon fiber reinforced polyetheretherketone (CF-PEKK) to sustain the loads and high temperatures required. The actuator part in Figure 7.2 contains a white region to hide a proprietary design part.

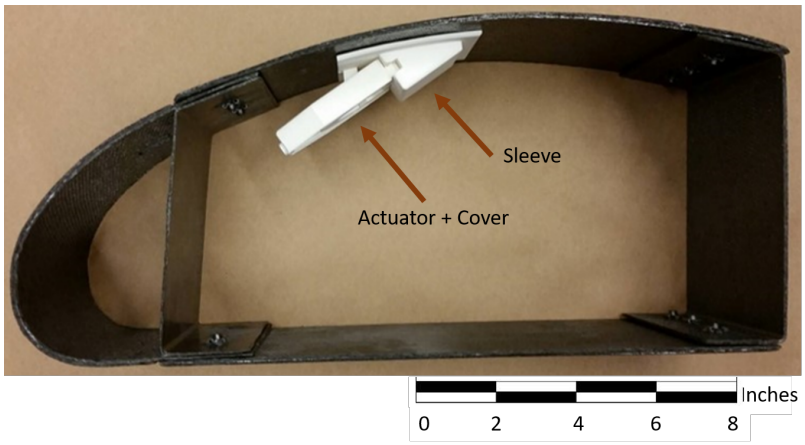

Figure 7.1: Final design visual mockup

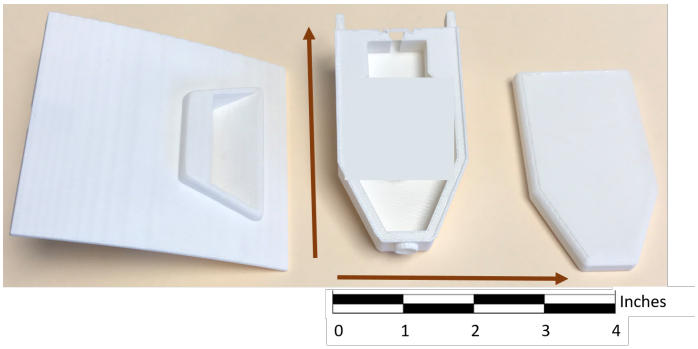

Figure 7.2: FO parts from left to right: sleeve, actuator, actuator cover

The final design accounted for the wing flap's curved geometry and added supporting structures to ensure secure attachment. The final design incorporated a support sleeve that attaches to the bottom surface of the wing through an adhesive and contains the nozzle extension profile of the actuator. The actuator then attaches to the bottom of the sleeve through the use of snapfits that require 12 lbf to attach, and 34 lbf to detach. An O-ring groove is placed at the top of the actuator to ensure sealing. The actuator was composed of two parts that are bonded together, the actuator and a top cover. Injection molding and 3D printing (SLS) were selected for manufacturing the FO due to the thermoplastic material constraint and high part quantities required.

A series of FEA and mold flow simulations were conducted on the FO to validate the final design. The FO was tested to verify attachment to the wing while sustaining loads

under 9G of acceleration. The maximum stress experienced was about 270 psi, which is far lower than the 8000 psi yield stress of the CF-PEKK material. Additional simulations for the actuator's attachment to the sleeve showed a maximum stress of 470 psi and a small deformation of only 0.00022". With regards to fatigue life, the design was found to sustain infinite life (1E6 cycles) for both the repeated loads on the FO and the repeated insertions of the actuator into the sleeve. Mold flow simulations verified the feasibility of injection molding each of the FO parts. These simulations resulted in design refinements, including hollowing out the internal cavities of the actuator to better manufacture it with injection molding (IM). With proper gate sizing and location, all of the FO parts were confirmed to be manufacturable through IM with fill times of less than 3 seconds and injection pressures that were less than 71% of the maximum injection pressures required. This was important as low injection pressures would result in short shots, while large pressures would result in flash.

Lastly, the cost analysis provided verification for the large-volume FO production. Cost was segmented into the manufacturing, material, and assembly costs. Manufacturing cost estimation for IM and 3D printing (SLS) processes yielded costs that ranged from $0.02-$0.03 per part depending on the manufacturing process used. The total material cost for the FO was $20.63 per part, while the assembly costs ranged from $0.02-$0.03 per part depending on the manufacturing process used. The assembly cost factored in the orientation angles, part symmetry, and ease of handling. Different part manufacturing configurations were created and the cost for large production volumes was determined. As shown in Figure 7.3, IM was found to be the most cost-efficient for quantities greater than 4550, while a combination of SLS and IM was beneficial for quantities less than that but greater than 1600. SLS 3D printing was the most cost-efficient for any production run less than 1600.

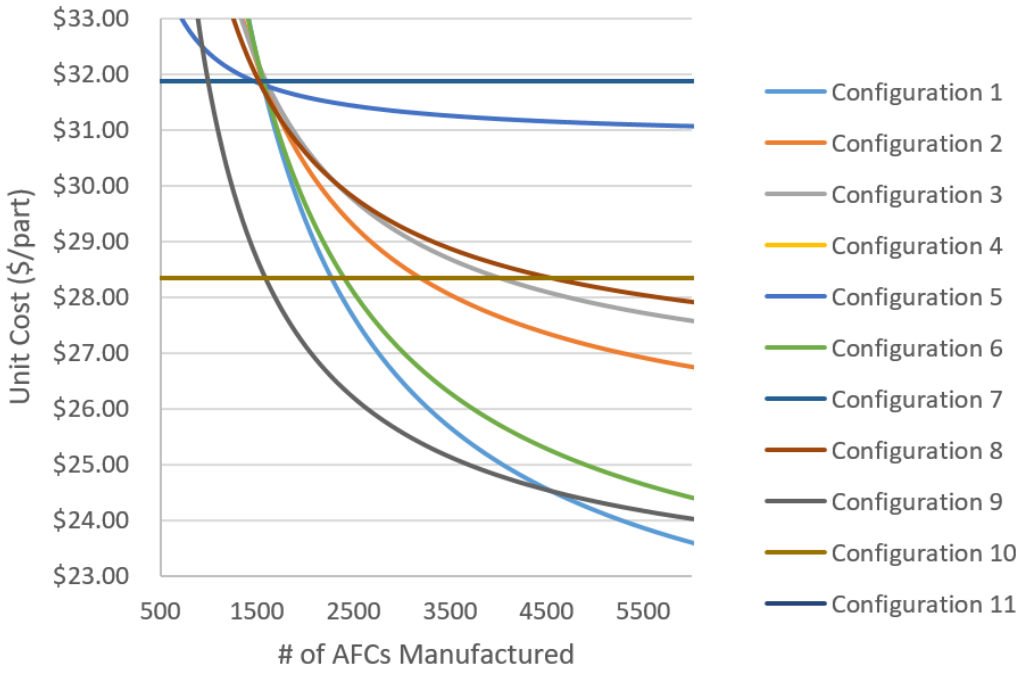

Figure 7.3: Design Configurations Unit Cost

This thesis proposes a design concept for the attachment of FOs to composite wing structures. The final design was created considering both structural and functional requirements, and was validated through simulations. This design was shown to be manufacturable for commercial applications by a cost analysis that validated the design for for large-volume production.

7.2 Future Work

Although the FO was tested using FEA to verify the attachment strength to the flap skin, more tests have to be conducted on the carbon fiber skin itself. The method of FO insertion into the flap requires a hole in the flap surface which affects the structural strength of the carbon fiber. While the sleeve proposed in the FO design provides structural support to the flap skin, more tests have to be conducted to further quantify this support. Tests should also be conducted on other techniques to reinforce the flap skin including how much support structure to have in the "doubler" around the hole. Additionally, fiber steering may also be

considered in which the carbon fiber tows are steered around the hole so that they remain continuous and enhance the structural strength of the flap skin.

Furthermore, while this project focused on the attachment of an FO to a composite wing flap, the design could be applied to several different aerospace structures such as different sections of the main wing, ailerons, rudders, and horizontal stabilizers. Applications outside of commercial aircraft include helicopter blades, drones, automobiles, trucks, and wind turbines. For all of these different applications, the proposed design should be adjusted to fit the needs of the new application.

Appendices

APPENDIX A

SUPPORTING INFORMATION

Table A.1: Design attachment listings for preliminary designs. Designs are listed: Internal (1-9), External (10-13), Internal-External (14-15)

Design #	Support-Structure Attachment	FO-Support Attachment	Nozzle-Skin Attachment	Nozzle-FO Attachment	Sealant System
1	Cocure	Snapfit	None	Fastener	O-ring
2	Cocure	Fastener	None	None	Gasket
3	Adhesive	Snapfit	Cobond	Plastic Welding	O-ring
4	Fastener	Plastic Welding	Cobond	Plastic Welding	Gasket
5	Cobond	Fastener	None	One part	O-ring
6	Snapfit	Snapfit	Cobond	Plastic Welding	O-ring
7	Snapfit	Snapfit	Cocure	Snapfit	O-ring
8	Cobond	Thermal Staking	None	One part	O-ring
9	Adhesive	Snapfit	None	One part	O-ring
10	Adhesive	Fastener	None	One part	O-ring
11	Adhesive	Thermal Staking	None	One part	O-ring
12	Cobond	Snapfit	None	One part	Gasket
13	Adhesive	Built-in bolt	None	One part	O-ring
14	Cobond	Fastener	Snapfit	One part	O-ring
15	Cobond	Fastener	Threaded	One part	O-ring

Table A.2: Snapfit assumptions

Item	Description
Equation	$C_{snap} = Volume_{snap} * Density * \frac{MaterialCost}{mass} * Quantity_{snap}$
Material cost	PEEK 30% fiber = \$62.5/lbm [44]
Material density	0.049 lbm/in^3 [44]
Quantity	2-4 dependent on part geometry
Assembly time	Assume 1.5 sec

Table A.3: Fastener assumptions

Item	Description
Equation	$C_{fastener} = Cost_{fastener} * Quantity_{fastener}$
Fastener cost	\$0.07 [45]
Quantity	2-4 dependent on part geometry + rivet strength
Assembly time	0.33 sec [46]

Table A.4: Thermal Staking assumptions

Item	Description
Equation	$C_{thermstake} = Volume_{stake} * Density * \frac{MaterialCost}{mass} * Quantity_{stake}$
PEEK cost	\$62.5/lbm [44]
PEEK density	0.049 lbm/in^3 [44]
Stake volume	CMT= 0.125, D= 0.1 [47]
Assembly time	Assume same time as fastening (0.33 sec)

Table A.5: Co-cure assumptions

Item	Description
Equation	$C_{cocure} = Volume_{resin} * Density * \frac{MaterialCost}{mass}$
Resin cost	$1170 for 10 gallons [48]
Resin density	18.77 lb/gal (2.25 g/ml) [49]
Assumption	Assume 0.1" thick resin coating
Assembly time	114 min [50]

Table A.6: Adhesive assumptions

Item	Description
Equation	$C_{adhesive} = Volume_{adhesive} * Density * \frac{MaterialCost}{mass}$
Resin cost	$207 for 0.05 gal (200ml) [51]
Resin density	18.77 lb/gal (2.25 g/ml) [52]
Assumption	Assume 0.1" thick resin coating
Assembly time	0.5 hr*Area (ft^2) [53]

Table A.7: Ultrasonic welding assumptions

Item	Description
Equation	$C_{weld} = Power_{supply} * \frac{ElectricityCost}{kWh} * Time_{weld}$
Power supply	3kW [54]
Electricity cost	$0.12/kWh [55]
Weld time	0.2-0.5 sec [54]

REFERENCES

[1] Interiot, *Stall formation*, 2006. [Online]. Available: http://www.sam.brooks.af.mil/af/files/fsguide/HTML/Graphics/fig_28-11.gif.

[2] L. F. School, *Flaps*, 2015. [Online]. Available: http://www.langleyflyingschool.com/Images/Aerodynamics%20and%20Theory%20of%20Flight/Flaps.gif.

[3] N. W. Rathay, M. J. Boucher, M. Amitay, and E. Whalen, "Performance enhancement of a vertical tail using synthetic jet actuators," in *AIAA Journal*, vol. 52, 2014, pp. 810–820.

[4] V. Ciobaca, T. Khn, and R. Rudnik, "Active flow separation control on a high-lift wing-body configuration, part 2: The pulsed blowing application," in *AIAA Applied Aerodynamics Conference*, 2011.

[5] W. Machunze, A. Gessler, T. Fabel, P. Horst, M. Rdel, K. Wolf, A. Ulbricht, S. Mnter, and W. Hufenbach, "Active flow control system integration into a cfrp flap," in *CEAS Aeronautical Journal*, vol. 7, 2016, pp. 69–81.

[6] E. D. Michael, A. W. Edward, and G. Ari, "Enhancement of high-lift system flap performance using active flow control," in *52nd Aerospace Sciences Meeting*, ser. AIAA SciTech, American Institute of Aeronautics and Astronautics, 2014.

[7] G. Gardiner, *Composites face challenges in next commercial airframes : Compositesworld*, 2015. [Online]. Available: http://www.compositesworld.com/blog/post/sampe-europe-highlights-composites-face-challenges-in-next-commercial-airframes.

[8] S. K. Mazumdar, *Composites manufacturing: materials, product, and process engineering*. Boca Raton, FLA: CRC Press, 2002.

[9] P. K. Mallick, *Fiber-reinforced composites: materials, manufacturing, and design*, 2nd. New York: Marcel Dekker, Inc., 2008.

[10] D. Wang, M. Ramulu, and D. Arola, "Orthogonal cutting mechanisms of graphite/epoxy composite. part i: Unidirectional laminate," in *International Journal of Machine Tools and Manufacture*, vol. 35, 1995, pp. 1623–1638.

[11] D. H. Wang, M. Ramulu, and D. Arola, "Orthogonal cutting mechanisms of graphite/epoxy composite. part ii: Multi-directional laminate," in *International Journal of Machine Tools and Manufacture*, vol. 35, 1995, pp. 1639–1648.

[12] J. P. Davim, *Machining Composite Materials*. London Hoboken, NJ: ISTE, 2010.

[13] J. Sloan, *A400m wing assembly: Challenge of integrating composites : Compositesworld*, 2012. [Online]. Available: http://www.compositesworld.com/articles/a400m-wing-assembly-challenge-of-integrating-composites.

[14] A. B. Strong, *Fundamentals of composites manufacturing : materials, methods, and applications*, 1st, C. A. Ploskonka, Ed. Society of Manufacturing Engineers: Publications Development Dept., 1989.

[15] M. Hashish, "Method and apparatus for forming a high velocity liquid abrasive jet," pat. US 4,648,215, 1987.

[16] OMAX, *Waterjet cutting compared*, 2015. [Online]. Available: https://www.omax.com/learn/waterjet-cutting-compared.

[17] M. Hashish, "Abrasive-waterjet machining of composites," in *WaterJet Technology Association*, 2008, p. 32.

[18] D. K. Shanmugam, T. Nguyen, and J. Wang, "A study of delamination on graphite/epoxy composites in abrasive waterjet machining," in *Composites Part A: Applied Science and Manufacturing*, vol. 39, 2008, pp. 923–929.

[19] C. Aerospace, *Cherry 1900 bulbing blind rivet*, 2009. [Online]. Available: http://www.cherryaerospace.com/docs/catalogs/CA-1035.pdf.

[20] Shur-Lok, *Advanced composites catalog*, 2015. [Online]. Available: https://studylib.net/doc/18642463/fasteners-for-advance-composites---shur-lok.

[21] E. M. Petrie, "Adhesives for the assembly of aircraft structures and components: Decades of performance improvement, with the new applications of the horizon," in *Metal Finishing*, vol. 106, 2008, pp. 26–31.

[22] B. Associates, *Adaptive control of synthetic jet actuators*, 2015. [Online]. Available: http://www.barron-associates.com/about/projects/adaptive-control-of-synthetic-jet-actuators/.

[23] M. Cattafesta L. N. Sheplak, "Actuators for active flow control," in *Annual Rev. Fluid Mech*, vol. 43, 2011.

[24] C. J. Glenn, *Fluidics*, E. F. Humphrey, Ed. Fluid Amplifier Associates, 1968.

[25] NASA, "F-16xl supersonic laminar flow," in *NASA Dryden*, NASA, 2004, p. 6.

[26] R. Petz, "Active separation control on a high-lift configuration by a periodically pulsating jet," in *International Congress of the Aeronautical Sciences*, 2004, p. 9.

[27] A. Kuchan, "The integration of active flow control devices into composite wing flaps," Master's thesis, Georgia Institute of Technology, 2012.

[28] J. Li, "Design of active flow control device integration into a composite flap structure," Master's thesis, Georgia Institute of Technology, 2016.

[29] A. Seifert, T. Shtendel, and D. Dolgopyat, "From lab to full scale active flow control drag reduction: How to bridge the gap?" In *Journal of Wind Engineering and Industrial Aerodynamics*, vol. 147, 2015, pp. 262–272.

[30] H. Becker and C. Grtner, "Polymer microfabrication technologies for microfluidic systems," in *Analytical and Bioanalytical Chemistry*, vol. 390, 2008, pp. 89–111.

[31] C.-W. Tsao and D. L. DeVoe, "Bonding of thermoplastic polymer microfluidics," in *Microfluidics and Nanofluidics*, vol. 6, 2009, pp. 1–16.

[32] N. P. Suh, *Axiomatic design : advances and applications*, ser. The MIT-Pappalardo series in mechanical engineering. New York: Oxford University Press, 2001.

[33] J. D. McLean and J. D. Crouch, *Study of the application of separation control by unsteady excitation to civil transport aircraft*, ser. NASA contractor report ; NASA CR-209338. Hampton, Va.: NASA Langley Research Center, 1999.

[34] I. Kroo, *Aircraft structural design*, 2016. [Online]. Available: http://www.aircraftspruce.com/catalog/hapages/avexblindriv.php?clickkey=116752.

[35] BLS, *National occupational employment and wage estimates*, 2015. [Online]. Available: https://www.bls.gov/oes/current/oes_nat.htm.

[36] L. Xu, *Using jmp to design experiments and analyze the results*, 2012. [Online]. Available: http://www.lisa.stat.vt.edu/sites/default/files/Using%20JMP%20to%20design%20experiments%20and%20analyze%20the%20results.pdf.

[37] Dukane, *Guide to ultrasonic plastics assembly*, 2011. [Online]. Available: https://www.dukane.com/us/Documents/DesignGuides/Guide%20To%20US%20Plastic%20Assembly.pdf.

[38] DSM, *Snap fit design*, 2005. [Online]. Available: http://fab.cba.mit.edu/classes/S62.12/people/vernelle.noel/Plastic_Snap_fit_design.pdf.

[39] G. D. Boothroyd and P. K. Winston, *Product design for manufacture and assembly*, I. Marinescu, Ed., 7. Boca Raton, FL: CRC Press Taylor and Francis Group, 2002, p. 505.

[40] Dotmar, *Co-efficient of friction — plastic properties tables*, 2015. [Online]. Available: http://www.dotmar.com.au/co-efficient-of-friction.html.

[41] R. G. Budynas, J. K. Nisbett, and J. E. Shigley, *Shigley's mechanical engineering design*, 9th, ser. McGraw-Hill series in mechanical engineering. New York: McGraw-Hill, 2011.

[42] Victrex, "Peek design guide," in *Victrex*, 2015, p. 26. [Online]. Available: http://www.hycompinc.com/PDFs/PEEK%20DESIGN%20GUIDE.pdf.

[43] M. Ruffo, C. Tuck, and R. Hague, "Empirical laser sintering time estimator for duraform pa," in *International Journal of Production Research*, vol. 44, 2006, pp. 5131–5146.

[44] G. Design, *Ces edupack*, 2016. [Online]. Available: http://www.grantadesign.com/education/edupack/.

[45] A. Spruce, *Avex non-structural blind rivets*, 2015. [Online]. Available: http://www.aircraftspruce.com/catalog/hapages/avexblindriv.php?clickkey=116752.

[46] J. Camillo, *Automating the riveting process*, 2015. [Online]. Available: http://www.assemblymag.com/articles/92592-automating-the-riveting-process.

[47] B. Ultrasonics, *Thermal staking design guidelines*, 2015. [Online]. Available: http://www.emersonindustrial.com/en-US/documentcenter/BransonUltrasonics/Plastic%20Joining/Non-Ultrasonics/Thermal%20Staking%20Design%20Guide%20pgs.pdf.

[48] U. Composites, *Epoxy : Epoxy resins and hardeners*, 2017. [Online]. Available: http://www.uscomposites.com/epoxy.html.

[49] Electrolube, *Er2074 epoxy resin technical data sheet*, 2005. [Online]. Available: http://www.electrolube.com/core/components/products/tds/044/ER2074.pdf.

[50] D. L. Dequine and C. Rush, "Continuous fiber composite part cost vs production volume by manufacturing process and material," in *Lockheed Martin*, 2014, p. 23. [Online]. Available: http://www.iceaaonline.com/ready/wp-content/uploads/2015/01/Chris-Rush-SoCal-ICEAA-Dec-2014.pdf.

[51] 3M, *3m ec-9323-2 b/a scotch-weld black two part structural adhesive*, 2016. [Online]. Available: http://site.skygeek.com/PDFs/3m-1711624itl-scotch-weld-epoxy-adhesive-9323-b-a-200-ml-tds.pdf.

[52] 3M., *Scotch weld 9323-2 two part structural adhesive*, 2010. [Online]. Available: http://site.skygeek.com/PDFs/3m-1711624itl-scotch-weld-epoxy-adhesive-9323-b-a-200-ml-tds.pdf.

[53] T. Buckley, *Structural bonding: The hidden costs of instant assembly*, 2014. [Online]. Available: http://na.henkel-adhesives.com/us/content_data/389642_Structural_Bonding_Hidden_Costs_of_Instant_Assembly_92315.pdf.

[54] A. Weber, *The economics of ultrasonics*, 2003. [Online]. Available: http://www.assemblymag.com/articles/83104-the-economics-of-ultrasonics.

[55] U. E. I. Administration, *Average price of electricity to ultimate customers by end-user*, 2016. [Online]. Available: https://www.eia.gov/electricity/monthly/epm_table_grapher.cfm?t=epmt_5_6_a.